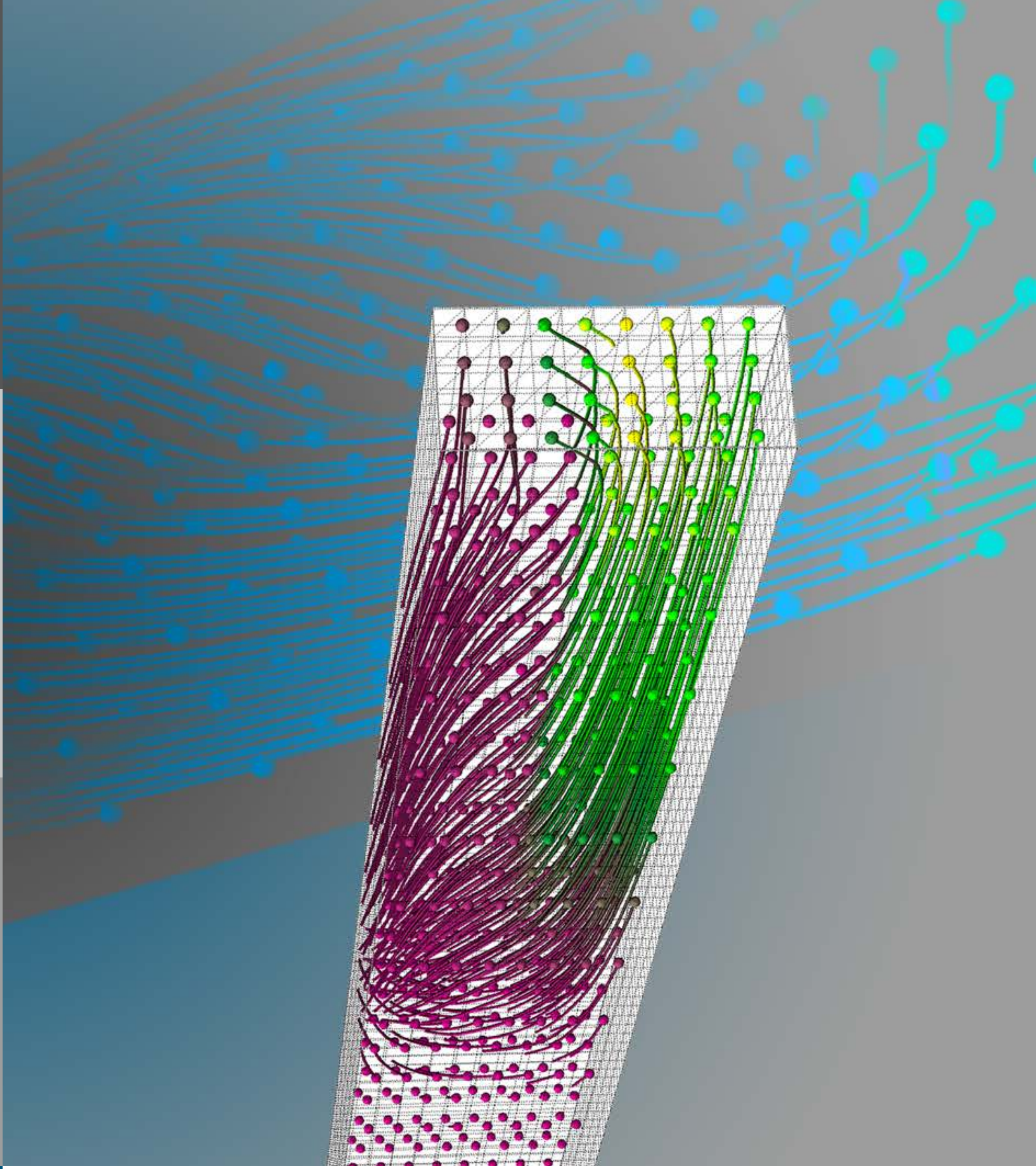

Coupled modeling of water, vapor and heat in unsaturated soils – Field applications and numerical studies

Christian Steenpaß

Member of the Helmholtz Association

JÜLICH
FORSCHUNGSZENTRUM

Schriften des Forschungszentrums Jülich
Reihe Energie & Umwelt / Energy & Environment Band / Volume 167

Forschungszentrum Jülich GmbH
Institute for Bio- and Geosciences (IBG)
Agrosphere (IBG-3)

Coupled modeling of water, vapor and heat in unsaturated soils – Field applications and numerical studies

Christian Steenpaß

Schriften des Forschungszentrums Jülich
Reihe Energie & Umwelt / Energy & Environment Band / Volume 167

ISSN 1866-1793 ISBN 978-3-89336-854-9

Bibliographic information published by the Deutsche Nationalbibliothek.
The Deutsche Nationalbibliothek lists this publication in the Deutsche
Nationalbibliografie; detailed bibliographic data are available in the
Internet at http://dnb.d-nb.de.

Publisher and Distributor:	Forschungszentrum Jülich GmbH Zentralbibliothek 52425 Jülich Phone +49 (0) 24 61 61-53 68 · Fax +49 (0) 24 61 61-61 03 e-mail: zb-publikation@fz-juelich.de Internet: http://www.fz-juelich.de/zb
Cover Design:	Grafische Medien, Forschungszentrum Jülich GmbH
Printer:	Grafische Medien, Forschungszentrum Jülich GmbH

Schriften des Forschungszentrums Jülich
Reihe Energie & Umwelt / Energy & Environment Band / Volume 167

D 82 (Diss., RWTH Aachen University, 2013)

ISSN 1866-1793
ISBN 978-3-89336-854-9

List of Contents

List of Figures

List of Tables

List of Symbols

A_n	[m^2]	part of surface area associated with boundary node n
b_1 b_2 b_3	[$W\ m^{-1}\ K^{-1}$]	empirical shape parameters of the thermal conductivity function λ_0
c	[$m\ s^{-1}$]	speed of light
C_a	[$J\ m^{-3}\ K^{-1}$]	volumetric heat capacity of air
C_n	[$J\ m^{-3}\ K^{-1}$]	volumetric heat capacities of the solid phase
C_p	[$J\ m^{-3}\ K^{-1}$]	volumetric heat capacity of porous media
C_v	[$J\ m^{-3}\ K^{-1}$]	volumetric heat capacity of water vapor
C_w	[$J\ m^{-3}\ K^{-1}$]	volumetric heat capacity of liquid water
D	[$m^2\ s^{-1}$]	vapor diffusivity in soil
D_a	[$m^2\ s^{-1}$]	water vapor diffusivity at a temperature
E	[$kg\ m^{-2}\ s^{-1}$]	evaporation rate
E_n	[$kg\ m^{-2}\ s^{-1}$]	evaporation rate at boundary note n
f_{cl}	[-]	clay mass fraction
F_i	[m^2]	total area of the i^{th} boundary segment with n as adjacent node point
g	[$m\ s^{-2}$]	gravitational acceleration
G	[$W\ m^{-2}$]	soil heat flux
G_{Wt}	[-]	gain factor for temperature induced changes in the soil water retention
h_P	[J s]	Planck's constant
h_p	[m]	pressure head
h	[m]	hydraulic head
H	[$W\ m^{-2}$]	sensible heat flux
H_r	[-]	relative humidity
$I(\lambda,T)$	[$J\ s^{-1}\ m^{-2}\ sr^{-1}\ m^{-1}$]	spectral radiance of a grey body
$I^{BB}(\lambda,T)$	[$J\ s^{-1}\ m^{-2}\ sr^{-1}\ m^{-1}$]	spectral radiance of a blackbody
k	[$J\ K^{-1}$]	Boltzmann constant
K_{lh}	[$m\ s^{-1}$]	isothermal liquid water hydraulic conductivity
K_{vh}	[$m\ s^{-1}$]	isothermal water vapor hydraulic conductivity
K_{lT}	[$m^2\ s^{-1}\ K^{-1}$]	thermal liquid water hydraulic conductivity
K_{vT}	[$m^2\ s^{-1}\ K^{-1}$]	thermal water vapor hydraulic conductivity
$\mathbf{K}^A$	[-]	dimensionless anisotropy tensor for the unsaturated hydraulic conductivity

K_{ij}^{A}	[-]	components of anisotropy tensor $\mathbf{K}^{A}$
K_s	[m s^{-1}]	saturated hydraulic conductivity
$\mathbf{Ks}^{A}$	[-]	dimensionless anisotropy tensor for the saturated hydraulic conductivity
Ks_{ij}^{A}	[-]	components of anisotropy tensor $\mathbf{Ks}^{A}$
l	[-]	van Genuchten Mualem empirical shape parameter
L_0	[J m^{-3}]	volumetric heat of vaporization of liquid water
L_w	[J kg^{-1}]	latent heat of vaporization of liquid water
M	[kg mol^{-1}]	molecular weight of water
N	[-]	number of measurements
m	[-]	van Genuchten Mualem empirical shape parameter
n	[-]	van Genuchten Mualem empirical shape parameter
N_i^{BP}	[-]	number of node points forming boundary segment *i*
q	[m s^{-1}]	Darcian fluid flux density
q_{h_i}	[J m^{-2} s^{-1}]	components of the total heat flux ($i = x, y, z$)
q_{l_i}	[m s^{-1}]	components of the liquid water flux density ($i = x, y, z$)
q_{lh_i}	[m s^{-1}]	isothermal liquid water flux components ($i = x, y, z$)
q_{lT_i}	[m s^{-}1]	thermal liquid water flux components ($i = x, y, z$)
q_i	[m s^{-1}]	components of the darcian flux ($i = x, y, z$)
q_n	[m s^{-1}]	actual flux at boundary node *n*
q_{v_i}	[m s^{-1}]	components of the vapor flux density ($i = x, y, z$)
q_{vh_i}	[m s^{-1}]	isothermal water vapor flux components ($i = x, y, z$)
q_{vT_i}	[m s^{-}1]	thermal water vapor flux components ($i = x, y, z$)
Q_n	[m^{3} s^{-1}]	Volume of water evaporated or infiltrated per time at boundary node *n*
R	[J mol^{-1} K^{-1}]	universal gas constant
r_a	[s m^{-1}]	atmospheric resistance to water vapor flow
r_H	[s m^{-1}]	aerodynamic resistance to heat flow
R_{net}	[W m^{-2}]	net radiation
S_e	[W m^{-2}]	effective saturation
T	[K]	temperature
T_a	[K]	air temperature
T_A	[K]	ambient temperature
T_{BG}	[K]	background temperature
T_D	[K]	temperature of the measurement distance
T_O	[K]	object temperature
T_s	[K]	temperature at the soil surface
t	[s]	time
x_j	[m]	spatial coordinates ($j = x, y, z$)
$\hat{\mathbf{Y}}$	[-]	vector of observed system behavior
y_i	[-]	ith observed value
$\hat{y}_i$	[-]	ith modeled value

α	$[m^{-1}]$	van Genuchten Mualem empirical shape parameter
α_M	[-]	Metropolis acceptance probability
β	[m]	thermal dispersivity
γ	$[kg\ s^{-2}]$	surface tension
γ_0	$[kg\ s^{-2}]$	surface tension of soil water at 25°C
η	[-]	enhancement factor
δ_{ij}	[-]	Kronecker delta function
ε	[-]	emissivity
ζ	[-]	measured initial conditions
Θ	[-]	model parameter vector
θ	$[m^3\ m^{-3}]$	total volumetric water content
θ_a	$[m^3\ m^{-3}]$	air filled porosity
θ_l	$[m^3\ m^{-3}]$	volumetric liquid water content
θ_n	$[m^3\ m^{-3}]$	volumetric fraction of the solid phase
θ_r	$[m^3\ m^{-3}]$	residual water content
θ_s	$[m^3\ m^{-3}]$	residual water content
θ_v	$[m^3\ m^{-3}]$	volumetric water vapor content
λ_0	$[W\ m^{-1}\ K^{-1}]$	thermal conductivity of porous medium
$\lambda_{ij}(\theta)$	$[W\ m^{-1}\ K^{-1}]$	apparent thermal conductivity tensor of soils
λ_L	[m]	longitudinal thermal dispersivity
λ_T	[m]	transverse thermal dispersivitiy
ρ_a	$[kg\ m^{-3}]$	atmospheric vapor density at a certain height
ρ_s	$[kg\ m^{-3}]$	actual vapor density at the soil surface
ρ_{sv}	$[kg\ m^{-3}]$	saturated vapor density
ρ_v	$[kg\ m^{-3}]$	actual vapor density
ρ_w	$[kg\ m^{-3}]$	density of liquid water
σ	[-]	reflectivity
σ_{SST}	[°C]	standard deviation of residuals measured and modeled surface temperatures
σ_{WCj}	$[m^3\ m^{-3}]$	standard deviation of residuals measured and modeled water contents at j = 7 cm, 15 cm
τ	[-]	transmissivity
τ_D	[-]	transmissivity of the measurement distance
τ_{MQ}	[-]	tortuosity as defined by Millington & Quirk
ϕ	[-]	measured boundary conditions
Φ_D	$[J\ s^{-1}\ m^{-2}]$	radiance emitted by the measurement distance
$\Phi_{D'}$	$[J\ s^{-1}\ m^{-2}]$	radiance leaving the measurement distance
Φ_e	$[J\ s^{-1}\ m^{-2}]$	emitted radiance
Φ_O	$[J\ s^{-1}\ m^{-2}]$	total radiance emitted by an object
Φ_r	$[J\ s^{-1}\ m^{-2}]$	reflected radiance
Φ_t	$[J\ s^{-1}\ m^{-2}]$	transmitted radiance

1 Introduction

1.1 Background and scope

The following work has been assembled while working within the Sonderforschungsbereich *Transregio Collaborative Research Center 32: Patterns in Soil – Atmosphere – Vegetation Systems* (SFB/TR32) (http://tr32.uni-koeln.de/index.php) between May 2007 and September 2010.

The SFB/TR32 is an interdisciplinary project of Universities of Aachen, Bonn, Cologne and Research Center Jülich. Its main focus is on the complex exchange processes of energy, water, and carbon between the domains of soil, vegetation, and lower atmosphere. These processes change in time and space and prediction remains a major challenge for scientists. Mechanisms in soil, vegetation and atmosphere are often studied separately from each other, with only rudimentary consideration of the other domains. However, interactions between the domains are stimulating factors in the spatiotemporal development of structural, physical and chemical patterns. SFB/TR32 tries to find a common approach to describe exchange processes, thereby deepening the understanding of patterns at different scales.

Projects within SFB/TR32 are grouped into different clusters, each cluster studying relevant processes at a different scale. Project sections include Cluster A, which studies flow and transport processes as well as structures at pore to meter scale. Cluster B combines modeling and non-invasive measurements to analyze spatiotemporal variability of matter and water fluxes. Cluster C analyzes water and solute fluxes at field scales and micro to meso-scale catchments up to a few hundred meters. Variability of land surface – atmosphere processes at regional scales is studied by Cluster D. Administration, data storage and management is supervised by Cluster Z (Figure 1.1).

The present work is placed in Cluster B, Project 4 which works at plot scales ranging from a few decimeters up to several meters. Project B4 is outlined for three research periods, whereas the first period focuses at processes and state variables and their patterns in bare soils. Apart from the present work, results of the first phase of Project B4 are documented in Vanderborght et al. (2010), Scharnagl et al. (2010), Talloen (2009) and Steenpass et al. (2010). In the second and third research period, models modified and used in the first project phase will be coupled to a crop model which adds processes needed to predict C-fluxes, and stronger emphasize will be put on scaling issues and higher dimensional statiotemporal patterns of soil-vegetation-atmosphere systems.

Main focus of Project 4 in the first phase of SFB/TR32 was put on state-of-the-art numerical modeling concepts, which can be used to simulate and predict patterns of state variables, parameters or fluxes observed at plot scale. Furthermore, remote sensing campaigns were planned as one possibility of measurement to experimentally observe patterns. As remote sensing methods always measure a signal summarized over the range of its influencing parameters, development and usage of inverse modeling and data assimilation tools were another important aspect of research. Additionally, key parameters necessary to carry effective information about patterns from one scale to another (be it via up- or downscaling) had to be identified and characterized.

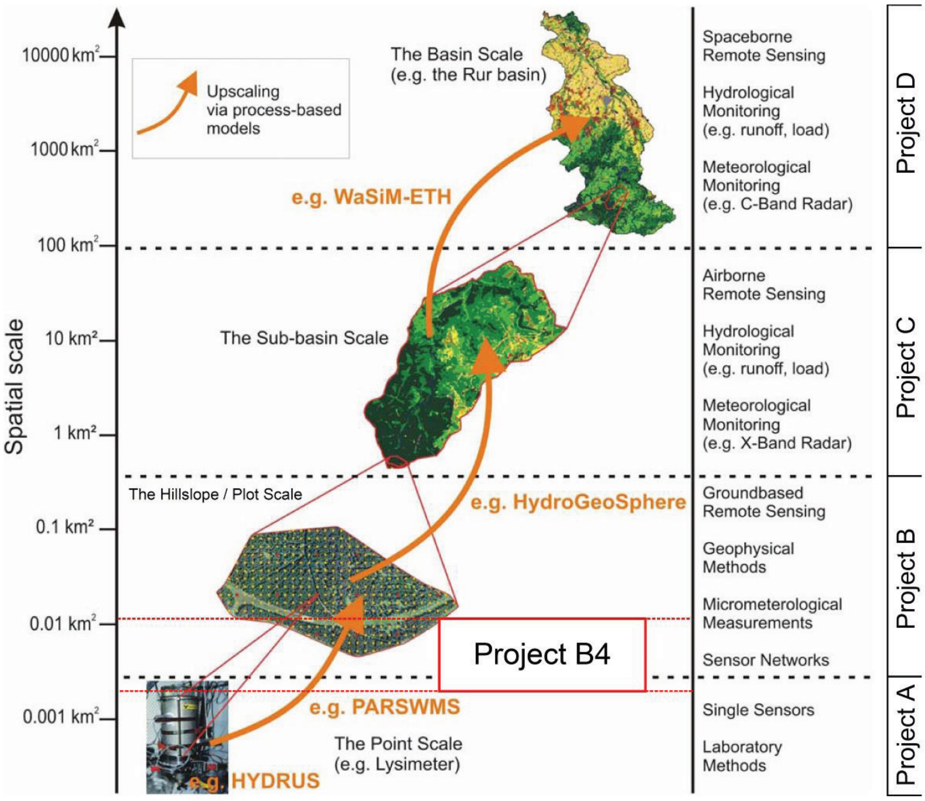

Figure 1.1: Schematic presentation of SFB/TR32 Project clusters ranging from point to regional (basin) scale. The position and associated scale ranges of Project B4 as subject of the present study within SFB/TR32 is marked by a red rectangle. Modified figure based on Bogena et al. (2006).

An important link between the different processes and scales of the neighboring domains soil and boundary layer atmosphere are water vapor fluxes. Water requires energy when changing state of aggregation from liquid to vapor and it releases energy when condensing again. Consequently, water vapor is a significant parameter in energy balances for atmospheric or soil-vegetation systems. In arid and semi-arid regions, water vapor is the dominating mechanism for evaporation from soils and water balances need to include liquid as well as water vapor fluxes. Looking from a hydrologic perspective, the importance of water and energy fluxes on important boundary layer parameters such as evaporation or surface temperature is studied in Project B4. In this context, water vapor needs to be evaluated as a coupling factor between water and energy flux in soils. On the other hand, looking from a boundary layer perspective, surface temperature or evaporation measurement patterns may be observed with remote sensing methods to assimilate those measurements and gain information about important parameters within the soil domain. Bringing together both points of view may provide opportunities to resolve scaling issues in soil – vegetation – atmosphere systems, which is one of the concluding intentions of SFB/TR32.

1.2 Objectives

Within the given framework of the Sonderforschungsbereich *Transregio Collaborative Research Center 32* and Project B4, three key aspects of research are discussed in the present work.

The role of coupled water and heat fluxes in soil:

Even though coupled heat and water fluxes have a long history of attention in the research field of soil sciences (Philip & de Vries, 1957; Rose, 1968a; Milly 1982; Noborio et al., 1996b; Saito et al., 2006; Bittelli et al.; 2008) the effects of neglecting thermal influence on the diurnal development of state variables as soil surface temperature or water content and consequently on the actual evaporation rate remains a challenge. However, these effects need to be characterized in order to provide (i) a valid lower boundary condition for atmospheric models even at high temporal resolutions and (ii) a mean to identify potential error-prone conditions when scaling up from physically based small scale processes to larger scale effective parameter based flows in soils.

The role of remote sensing methods to allow for an adequate parameterization of the soil surface as common boundary of soil – vegetation – atmosphere systems:

Soil surfaces provide important boundaries for both atmospheric and hydrologic systems. Typically, numerical models focus on either of the two systems. For example, hydrological models use meteorological data to characterize the upper boundary. However, feedback of the land surface to the atmosphere is not considered. On the other hand, meteorological models focus on processes within the atmosphere, but the soil as its lower boundary is often simplified with static process descriptions. In order to satisfyingly consider complex feedback mechanisms between both systems, appropriate methods to parameterize the soil surface even over large areas need to be available. Remote sensing methods by themselves and/or in combination with other methods such as data assimilation or inverse modeling tools provide a potentially powerful tool to do so.

The role of a mechanistic three-dimensional model in order to reproduce spatiotemporal patterns of key state variables:

The gap between an appropriate spatial resolution of regional and plot scale models complicates a direct data exchange of models used on differing scales. One reason for this is the high computing time needed to simulate small scale processes on a large area. Even though advances in computer science may put this problem into perspective, there is still the issue of the high demand of needed data to parameterize process-based models on small scales, making usage and parameterization of these models impractical on large scales. Consequently, for regional scale modeling, effective parameters averaged over specific areas have to be used to represent generally three dimensional systems with a simplified one-dimensional approach. By doing this, the influence of small scale heterogeneities and lateral fluxes is neglected. This leads to the challenging question of how vertical differences in soil state variables relevant at the centimeter scale can (or need to) be considered in one dimensional models using averaged state variables. To answer this question, the first step has to be the development of a three-dimensional model incorporating all relevant small scale processes. This model can be used to serve as a “benchmark model” to quantify biases between effective one-dimensional large scale and mechanistic three-dimensional small scale models.

1.3 Overview

The present Chapter 1 provides some remarks concerning the framework under which this work originated (Section 1.1). Section 1.2 gives a short definition of key aspects or, in other words the line of approach of this dissertation. An overview of the whole work is presented in the current Section 1.3, some general remarks and notations important in course of the following chapters are given in Section 1.4.

In Chapter 2, a brief discussion of theoretical basics important for the following chapters will be presented: First, the governing equations for coupled heat and water flow as used in this study are briefly discussed (Section 2.1). Chapter 2 also gives a short overview about the energy balance equation as an upper boundary condition (Section 2.2). In a last section (Section 2.3), basics about thermography playing an important role in Chapter 4, are given.

Chapter 3 addresses basic characteristics of “coupled” flux, “non-coupled” flux and actually controversial topics within the field of coupled heat and water modeling. In this study, coupled modeling, when compared to non-coupled modeling, includes consideration of water movement due temperature gradient and water vapor movement due to temperature and pressure head gradient. Section 3.2 focuses on differences between coupled and non-coupled modeling on important soil and boundary parameters such as temperature, water content and evaporation. The total water flux and distribution and contribution of its flux components (thermal liquid/vapor flux and isothermal liquid/vapor flux) is addressed in Section 3.3. Section 3.4 deals with the actual controversy about the water vapor enhancement factor, and gives a statement about the usage of this parameter within this work.

Chapter 4 uses a coupled water and heat model approach to inversely estimate soil hydraulic properties from infrared (IR) and time domain reflectometry (TDR) measurements. After introduction (Section 4.1), a concentrated description of relevant methods used to develop this approach follows in Section 4.2. Two kinds of experiments were performed to test the feasibility of the approach: In a synthetic experiment, the general information content of the soil surface temperature to infer Mualem – van Genuchten hydraulic parameters of the upper soil region is studied. As identifiably of the hydraulic parameters was good, a field experiment was conducted to test the estimation approach under field conditions. Both experiments and their results as well as concluding remarks are given in Section 4.3 and 4.4, respectively.

In Chapter 5, a three-dimensional coupled model is used to study the effect of horizontal heat and water fluxes in vertically heterogeneous soils with a focus on soil evaporation. To characterize the effect of these fluxes a good understanding of evaporation from homogeneous and layered soils is necessary: Therefore, Section 5.1 summarizes some actual studies concerning evaporation from bare soils and puts Chapter 5 into context of the actual research concerning soil evaporation. Methods and parameters used in this Chapter are given in Section 5.2. To quantify the influence of horizontal water and heat fluxes, modeled evaporation from a homogeneous uniform soil with a two-material soil consisting of different materials in vertical contact is compared. Differences in evaporation between both soil columns and the influence of heat and water flux are individually discussed in Section 5.3. Section 5.4 lists conclusions that can be drawn from this study.

Chapter 6 summarizes main results of the present dissertation (Section 6.1) and gives concluding remarks (Section 6.2) in order to put the results of this study into the context of the following research periods of SFB/TR32 in general and of Project B4 in particular.

1.4 General remarks

Throughout this work, the software packages HYDRUS-1D (H1D) or HYDRUS-3D (H3D) are used as basic hydrologic model. Both software packages have been developed and improved by Jirka Šimůnek (Department of Environmental Sciences, University of California Riverside), Rien van Genuchten, Miroslav Šejna and others. Modifications made to the source code of H1D and H3D were done with permission of and partly in cooperation with Jirka Šimůnek and were implemented for personal use separately from the official development branch of the HYDRUS packages. These modifications include the implementation of a surface energy balance and the consideration of water vapor (and liquid water) fluxes due to a temperature and a pressure head gradient. In this work, the term “coupled” denotes movement of water as an entirety of liquid water and water vapor not only due to a hydraulic but also to a thermal gradient within a soil. Opposing “coupled” movement, the terms “uncoupled” or “non-coupled” characterize movement of liquid water due to a hydraulic gradient in a soil, or in other words, movement of water based on the classical *Richards Equation*.

Additionally, modifications to the source code of H1D and H3D were made to make the program compatible to computers with a Linux operating system, allowing easy usage of HYDRUS on Linux computer clusters. Note that the actual version of H1D (4.15) officially supports vapor flow and coupled heat and water fluxes as well as an energy balance boundary condition. However, by the time of this work the official version of H1D did not support the mentioned mechanisms, making modifications of the source code of H1D v3.0 inevitable. In the actual official version of H3D (2.01), neither vapor flow nor an energy balance boundary condition is supported making modifications to the H3D source code necessary. To visualize result data files from H1D or H3D, the free UNIX software packages of gnuplot version 4.2, inkscape version 0.46 and VisIt version 2.1.2 were used. The software package IRBIS® (IRBIS control, IRBIS remote, IRBIS professional) by InfraTec GmbH (Dresden, Germany) was used to control and visualize infrared measurements.

Please note that some repetitions of context-important equations and/or statements are allowed in favor of a better conclusiveness of the individual chapters.

2 Theory

The HYDRUS software packages present a set of numerical models to simulate water, heat and solute transport in water variably-saturated modeling domains in the subsurface. HYDRUS packages numerically solve the *Richard's Equation* for variably-saturated water flow and convection-dispersion type equations for heat (and solute) transport. HYDRUS-1D can be used only for one-dimensional problems, whereas the software package HYDRUS-3D provides support for two- as well as three-dimensional problems and modeling domains. Heat transport in H1D and H3D considers movement by conduction as well as convection along with flowing liquid water. In the official versions of H1D v3.0 and H3D v1.0, the effect of water vapor on the water mass balance as well as movement of liquid water and water vapor due to a temperature gradient, coupling heat and water fluxes, is not taken into account. The actual H1D version 4.15 does support coupled fluxes and an energy balance boundary equation. However, no suitable version was available at the beginning of the present work. Therefore, following Saito et al. (2006), versions built from modified source codes of H1D (v. 3.0) and H3D (v 1.0) are used to correctly account for coupled heat, water, and water vapor flow. The relevant governing equations for heat, water and coupled heat-water flow can be found in Sections 2.1.1 - 2.1.3.

Another modification concerns the boundary conditions available for HYDRUS. Water flow boundary conditions in HYDRUS software packages can be defined by prescribed head or flux boundaries, free drainage, and atmospherically controlled boundaries. To solve the heat transport, first-type (Dirichlet), prescribing the temperature, and third-type (Cauchy) boundary conditions, setting the heat flux along the boundary of a modeling domain, can be used. However, for field soils which are strongly influenced by the soil-atmosphere interactions, measurements of evaporation and soil heat flux are often costly and time-consuming. Therefore, an energy balance boundary condition has been implemented in our modified versions of H1D and H3D to calculate soil surface heat and water fluxes from existing meteorological measurements, such as air temperature, wind speed, air humidity and radiation. Governing equations for the energy balance are described in Section 2.2.

Due to the vast functionalities of the HYDRUS packages, only descriptions of processes relevant for this work are given. For a full description including all features and functionalities of the HYDRUS software packages please refer to Šimůnek et al. (2005) and Šimůnek et al. (2006).

2.1 Coupled heat and water flow

2.1.1 Water flow

According to *Darcy's Law* (1856), three-dimensional water flux in water saturated anisotropic porous media follows a gradient in total water potential and water flows from high to low pressures according to

$$q_i = -K_S K s_{ij}^A \frac{\partial h}{\partial x_j} \qquad 2.1$$

where q_i [m s^{-1}] is the darcian flux in the directions $i = x, y, z$, K_s [m s^{-1}] is the saturated hydraulic conductivity, Ks^A_{ij} are components of the dimensionless anisotropy tensor of the saturated hydraulic conductivity, h [m] is the hydraulic head and x_j [m] are the spatial coordinates ($j = x, y, z$) (Šimůnek et al., 2006). In Eq. 2.1, as elsewhere in this work unless stated otherwise, *Einstein's summation convention* is used. This means that in any product of terms, a suffix (sub- or superscript) repeated twice is to be summoned over its range of values. According to this convention, Eq. 2.1 can be rewritten as:

$$\begin{aligned} q_x &= -K_S\left(Ks^A_{xx}\frac{\partial h}{\partial x} + Ks^A_{xy}\frac{\partial h}{\partial y} + Ks^A_{xz}\frac{\partial h}{\partial z}\right) \\ q_y &= -K_S\left(Ks^A_{yx}\frac{\partial h}{\partial x} + Ks^A_{yy}\frac{\partial h}{\partial y} + Ks^A_{yz}\frac{\partial h}{\partial z}\right) \\ q_z &= -K_S\left(Ks^A_{zx}\frac{\partial h}{\partial x} + Ks^A_{zy}\frac{\partial h}{\partial y} + Ks^A_{zz}\frac{\partial h}{\partial z}\right) \end{aligned} \qquad 2.2$$

where the nine components Ks_{ij}^A [-] define the hydraulic conductivity tensor $\mathbf{Ks}^A$ (Bear 1972).

Liquid water flux in unsaturated soils depends on the hydraulic conductivity, which itself is a function of the pressure head h_p:

$$q_{l\,i} = -K\left(K^A_{ij}\frac{\partial h_p}{\partial x_j} + K^A_{iz}\right) \qquad 2.3$$

where q_{l_i} [m s^{-1}] are the components of the liquid water flux, K [m s^{-1}] is the unsaturated hydraulic conductivity depending on the pressure head h_p [m] and K_{ij}^A are components of the dimensionless anisotropy tensor $\mathbf{K}^A$ of the unsaturated hydraulic conductivity (Šimůnek et al., 2006).

Water content and pressure head in the vadose zone are changing over time, as they are influenced by different boundary conditions such as evaporation or changing ground water levels. These changes over time, neglecting sink/source terms, can be described with the mass conservation equation.

$$\frac{\partial \theta_l(h_p)}{\partial t} = -\frac{\partial q_{l\,i}}{\partial x_i} \qquad 2.4$$

where $\theta_l(h_p)$ [cm^3 cm^{-3}] is the volumetric liquid water content as a function of h_p and t [s] is the time.

Combination of the Equations 2.3 and 2.4 yields the *Richards equation*, which describes variably saturated flow in porous media.

$$\frac{\partial \theta_l(h_p)}{\partial t} = \frac{\partial}{\partial x_i}\left[K\left(K_{ij}^A \frac{\partial h}{\partial x_j} + K_{iz}^A\right)\right] \qquad 2.5$$

Since the *Richards equation* is a non-linear partial differential equation, analytical solutions can be found only for a few simplified problems. Therefore, numerical models as the HYDRUS packages are used to solve problems concerning variably saturated flow in porous media.

2.1.2 Heat transport

A temperature gradient in a soil exists if the kinetic energy of molecules (*Brownian motion*) in the soil differs in horizontal and/or vertical direction. Collision of molecules in a warm, high energy region with molecules of a cold, low energy region causes kinetic energy to be transferred from the warm to the cold region. Apart from this conduction of heat, heat can also be transported by convection. In this mechanism, thermal energy is transported in fluids associated with the actual mass movement of fluids from one region to another (Bear, 1972). Both mechanisms (conduction and convection) can be described based on *Fourier's law*:

$$q_{h\,i} = \lambda_{ij}(\theta)\frac{\partial T}{\partial x_j} - C_w q_{l\,i}\frac{\partial T}{\partial x_i} \qquad 2.6$$

where q_{h_i} [J m^{-2} s^{-1}] is the total heat flux, $\lambda_{ij}(\theta)$ [J m^{-1} s^{-1} K^{-1}] is the apparent thermal conductivity of soils, T [K] is the temperature and C_w [J m^{-3} K^{-1}] is the volumetric heat capacity of water (Šimůnek et al., 2006). The first term on the right-hand side describes heat movement by conduction, the second heat movement by convection.

Equation 2.6 can be combined with the energy conservation equation (Eq. 2.7), again neglecting heat sinks and sources, to gain the governing equation for heat transport (Eq. 2.8) in soils (Sophocleous, 1979).

$$C_p\frac{\partial T}{\partial t} = -\frac{\partial q_{h\,i}}{\partial x_i} \qquad 2.7$$

where C_p [J m^{-3} K^{-1}] is the volumetric heat capacity of porous media.

$$C_p \frac{\partial T}{\partial t} = \frac{\partial}{\partial x_i}\left(\lambda_{ij}(\theta) \frac{\partial T}{\partial x_j} \right) - C_w q_{li} \frac{\partial T}{\partial x_i} \qquad 2.8$$

The volumetric heat capacity of porous media in Equation 2.7 and 2.8 consists of the volumetric heat capacities of the different components of the soil:

$$C_p T = \left(C_w \theta_l + C_n \theta_n + C_v \theta_v \right) T \qquad 2.9$$

where θ_n, θ_l, and θ_v, [cm^3 cm^{-3}] are the volumetric fractions of the solid, liquid, and gas phase, respectively, C_n and C_v [J m^{-3} K^{-1} both] are the volumetric heat capacities of the solid and gas phase, respectively.

2.1.3 Coupling of water flow and heat transport

The *Richards equation* (Eq. 2.5) describes the water flow in porous media according to gradients in the pressure head. Effects of the vapor phase on the overall water mass balance is not taken into account. Additionally, liquid and water vapor flux occurs also due to a temperature gradient, which is not considered in the original *Richards equation.* While this assumption is valid for most situations, water vapor effects cannot be neglected within dry soils, where water vapor is known to play an important role. Hence Equation 2.5 needs to be modified to correctly describe liquid and water vapor flow under pressure head and temperature gradients (e.g. Milly, 1984; Parlange et al., 1998; Saito, 2006; Sakai et al., 2009):

$$\frac{\partial \theta(h_p)}{\partial t} = \frac{\partial}{\partial x_i}\left[\left(K_{lh} + K_{vh} \right)\left(K_{ij}^{A} \frac{\partial h_p}{\partial x_j} + K_{iz}^{A} \right) + \left(K_{lT} + K_{vT} \right) K_{ij}^{A} \frac{\partial T}{\partial x_j} \right] \qquad 2.10$$

where θ [m^3 m^{-3}] is the total volumetric water content expressed as volume of water per bulk volume of soil and consists of the sum of the volumetric liquid water content θ_l [m^3 m^{-3}] and the volumetric water vapor content θ_v [m^3 m^{-3}] (expressed as volume of water per bulk volume of soil)($\theta = \theta_l + \theta_v$), K_{lh} and K_{vh} [m s^{-1} both] are the isothermal liquid and vapor hydraulic conductivities and K_{lT} and K_{vT} [m^2 s^{-1} K^{-1} both] are the thermal liquid and vapor hydraulic conductivities, respectively (García-Navarro & Playán, 2008). Conductivities and their relation to physical / thermodynamical parameters and properties of the porous media are given in Section 2.1.4.

Taking water vapor flow into account also requires expansion of the governing equation of heat transport (Eq. 2.8) as water vapor plays an important role in overall heat transport (e.g. Saito, 2006; Sakai et al., 2009).

$$C_p(\theta)\frac{\partial T}{\partial t}+L_0\frac{\partial \theta_v}{\partial t}=\frac{\partial}{\partial x_i}\left(\lambda_{ij}(\theta)\frac{\partial T}{\partial x_j}\right)-C_w q_{l\,i}\frac{\partial T}{\partial q_i}C_v\frac{\partial q_{v\,i}T}{\partial x_i}-L_0\frac{\partial q_{v\,i}}{\partial x_i} \qquad 2.11$$

where L_0 [J m^{-3}] is the volumetric heat of vaporization of liquid water and q_{v_i} [m s^{-1}] are the components of the vapor flux density. In Eq. 2.11, the governing equation of heat is expanded by the convection of sensible heat by water vapor (third term right-hand side) and the convection of latent heat by water vapor (forth term right-hand side). The volumetric heat of vaporization is given by

$$L_0 = L_w \rho_w \qquad 2.12$$

where L_w [J kg^{-1}] is the latent heat of vaporization of liquid water and ρ_w [kg m^{-3}] is the density of liquid water.

Water vapor pressure depends on temperature, as an increase in temperature results in an increase of water vapor present in air. As soils can be subject to temperature differences (e. g. with depth and/or diurnally), temperature differences may lead to water vapor flux based on temperature gradients (thermal vapor flux). Due to the interaction between liquid and vapor phases, the water vapor pressure at a constant temperature T also depends on the soil’s water pressure head prevailing in the soil profile, resulting in vapor flow based on the hydraulic gradient (isothermal vapor flux). Hence, in coupled heat and water flux modeling, water vapor flux density q_{v_i} consists of an isothermal and a thermal vapor flux component (Philip & de Vries, 1957). Note that it is assumed that there is no bulk air flow in soils, so that vapor flow due to convection is neglected.

$$q_{v\,i}=q_{vh\,i}+q_{vT\,i}=-K_{vh}K_{ij}^{A}\frac{\partial h_p}{\partial x_j}-K_{vT}K_{ij}^{A}\frac{\partial T}{\partial x_j} \qquad 2.13$$

where q_{vh_i} [m s^{-1}] is the isothermal vapor flux component following an hydraulic gradient and q_{vT_i} [m s^{-1}] is the thermal water vapor flux following a thermal gradient.

Similar to water vapor flux, liquid water flux needs to be redefined when considering hydraulic together with thermal gradients.

$$q_{l\,i} = q_{lh\,i} + q_{lT\,i} = -K_{lh}\left(K_{ij}^{A}\frac{\partial h_p}{\partial x_j} + K_{iz}^{A}\right) - K_{lT}\left(K_{ij}^{A}\frac{\partial T}{\partial x_j}\right) \qquad 2.14$$

where q_{lh_i} [m s^{-1}] is the isothermal liquid water flux component, and q_{lT_i} [m s^{-1}] is the thermal liquid water flux following a thermal gradient.

2.1.4 Soil thermal and hydraulic properties

The thermal water vapor hydraulic conductivity K_{vT} is defined as follows (Nassar & Horton, 1989):

$$K_{vT} = \frac{D}{\rho_w}\eta H_r \frac{d\rho_{sv}}{dT} \qquad 2.15$$

where D is the vapor diffusivity in soil [m^2 s^{-1}], η [-] is an enhancement factor accounting for increased thermal vapor fluxes due to increased temperature gradients in the air phase, H_r [-] is the relative humidity, and ρ_{sv} [kg m^{-3}] is the saturated vapor density.

Water vapor diffusivity in soils is given by (Saito et al., 2006)

$$D = \tau_{MQ}\theta_a D_a \qquad 2.16$$

where θ_a [m^3 m^{-3}] is the air filled porosity, D_a [m^2 s^{-1}] is the water vapor diffusivity at a temperature T [K]

$$D_a = 2.12\times10^{-5}\left(\frac{T}{273.15}\right)^2 \qquad 2.17$$

and τ_{MQ} [-] is the tortuosity as defined by Millington & Quirk (1961)

$$\tau_{MQ} = \frac{\theta_a^{7/3}}{\theta_s^{\,2}} \qquad 2.18$$

where θ_s [m^3 m^{-3}] is the saturated water content.

The enhancement factor (see Section 3.4) (Cass et al., 1984) can be written as

$$\eta = 9.5 + \frac{3\theta}{\theta_s} - 8.5\exp\left\{-\left[\left(1+\frac{2.6}{\sqrt{f_{cl}}}\right)\frac{\theta}{\theta_s}\right]^4\right\} \qquad 2.19$$

where f_{cl} [-] is the clay mass fraction.

The relative humidity H_r [%] is calculated from the thermodynamic relationship between liquid water and water vapor in soil pores is first introduced by Edlefsen and Anderson (1943) and depends on the pressure head (Eq. 2.20), whereas the saturated vapor density ρ_{sv} depending on a temperature T can be calculated from Equation 2.21.

$$H_r = \exp\left(\frac{h_p Mg}{RT}\right) \qquad 2.20$$

$$\rho_{sv} = 10^{-3}\,\frac{\exp\left(31.3716 - \frac{6014.79}{T} - 7.92495\times10^{-3}T\right)}{T} \qquad 2.21$$

In Eq. 2.20, M is the molecular weight of water [kg mol^{-1}], g is the gravitational acceleration [m s^{-2}], R is the universal gas constant [J mol^{-1} K^{-1}], and the pressure head h_p is expressed in meters.

The isothermal vapor hydraulic conductivity K_{vh} [m s^{-1}] is defined as follows:

$$K_{vh} = \frac{D}{\rho_w}\rho_{sv}H_r\frac{Mg}{RT} \qquad 2.22$$

Following Noborio et al. (1996b), thermal hydraulic conductivity K_{lT} [m^2 K^{-1} s^{-1}] for liquid water flux can be expressed as

$$K_{lT} = K_{lh}\left(hG_{wT}\frac{1}{\gamma_0}\frac{d\gamma}{dT}\right) \qquad 2.23$$

where K_{lh} [m s^{-1}] is the isothermal liquid hydraulic conductivity, γ [kg s^{-2}] is the surface tension, γ_0 [kg s^{-2}] is the surface tension of soil water at 25°C, G_{wT} [-] is a gain factor (Nimmo & Miller, 1986), which depends on the soil water content and the type of soil and accounts for temperature induced changes in the soil water retention. The surface tension as a function of temperature T [°C] is defined as follows:

$$\gamma = 75.6 - 0.1425T - 2.38\times10^{-4}T^2 \qquad 2.24$$

The isothermal hydraulic conductivity K_{lh} [m s^{-1}] itself is derived using the pore-size distribution model of Mualem (1976) from the analytical retention function of van Genuchten (1980):

$$K_{lh}(h) = K_s S_e^l \left[1-\left(1-S_e^{1/m}\right)^m\right]^2 \qquad 2.25$$

where K_s [m s^{-1}] is the saturated hydraulic conductivity, S_e [-] is the effective saturation, and l and m [-] are empirical parameters.

$$\theta_l(h) = \begin{cases} \theta_r + \dfrac{\theta_s-\theta_r}{\left[1+\left|\alpha h_p\right|^n\right]^m} & h_p < 0 \\ \\ \theta_s & h_p \geq 0 \end{cases} \qquad 2.26$$

where θ_r [m^3 m^{-3}] is the residual water content, α [m^{-1}], n [-] and m ($m=1-1/n$) [-] are empirical parameters.

According to Šimůnek & Suarez (1993), the apparent soil thermal conductivity incorporates the thermal conductivity of the porous medium (solid + water) and the macrodispersivity as a linear function of the flux (de Marsily, 1986).

$$\lambda_{ij}(\theta) = \lambda_T C_w |q| \delta_{ij} + (\lambda_L - \lambda_T) C_w \frac{q_j q_i}{|q|} + \lambda_0(\theta)\delta_{ij} \qquad 2.27$$

where q [m s^{-1}] is the absolute of the Darcian fluid flux density, δ_{ij} is the *Kronecker delta* function and λ_L and λ_T [m] are the longitudinal and transverse thermal dispersivities. The Kronecker delta is defined as

$$\delta_{ij} = \begin{cases} 1 & if \quad i = j \\ 0 & if \quad i \neq j \end{cases} \qquad 2.28$$

Using the *Kronecker delta* function and *Einstein's summation convention*, in three dimensions the nine components of the apparent thermal conductivity tensor can also be written as:

$$\begin{aligned}
\lambda_{xx} &= \lambda_L C_w \frac{x_x^2}{|q|} + \lambda_T C_w \frac{x_y^2}{|q|} + \lambda_T C_w \frac{x_z^2}{|q|} + \lambda_0 \\
\lambda_{yy} &= \lambda_L C_w \frac{x_y^2}{|q|} + \lambda_T C_w \frac{x_x^2}{|q|} + \lambda_T C_w \frac{x_z^2}{|q|} + \lambda_0 \\
\lambda_{zz} &= \lambda_L C_w \frac{x_z^2}{|q|} + \lambda_T C_w \frac{x_x^2}{|q|} + \lambda_T C_w \frac{x_y^2}{|q|} + \lambda_0 \\
\lambda_{xy} &= (\lambda_L - \lambda_T) C_w \frac{q_x q_y}{|q|} \\
\lambda_{xz} &= (\lambda_L - \lambda_T) C_w \frac{q_x q_z}{|q|} \\
\lambda_{yz} &= (\lambda_L - \lambda_T) C_w \frac{q_y q_z}{|q|}
\end{aligned} \qquad 2.29$$

where λ_0 [J s^{-1} m^{-1} K^{-1}] is the thermal conductivity depending on water content θ, which accounts for the tortuosity of the porous media. Following Chung & Horton (1987), the thermal conductivity is expressed as

$$\lambda_0(\theta) = b_1 + b_2\theta_l + b_3\theta_l^{1/2} \qquad 2.30$$

where b_1, b_2 and b_3 [W m^{-1} K^{-1}] are empirical shape parameters.

2.2 Energy balance boundary condition

The solution of the partial differential equations describing water and heat flux requires knowledge of initial and boundary conditions. For the boundary condition at the soil/air interface, surface heat and water fluxes are computed using a surface energy balance from measured meteorological data (i.e., rainfall, air temperature, wind speed, air humidity and radiation) and state variables T, h_p, and θ_v at the soil surface. Since the calculated mass and energy fluxes, which are used as boundary conditions for the solution of the water and heat flow equations, depend on the soil surface state variables and thus the solution of the water and heat flow equations themselves, the surface fluxes and state variables had to be derived iteratively. Two iteration loops were found to be a good tradeoff between the accuracy and computational effort (Saito et al., 2006).

The surface energy balance is given as:

$$G = R_{net} - H - L_w \cdot E \qquad 2.31$$

where G [W m^{-2}] is the heat flux into the soil, R_{net} is the net radiation [W m^{-2}], H is the sensible heat flux [W m^{-2}], L_w is the latent heat of vaporization [J kg^{-1}], and E is the evaporation rate [kg m^{-2} s^{-1}]. G and R_{net} are defined to be positive downward (into the soil profile) and L_wE and H are defined to be positive upward (out of the soil profile).

The net radiation R_{net} is the sum of the net shortwave and net longwave radiation (sum of incoming and outgoing shortwave and longwave radiation). Following van Bavel & Hillel (1976), the latent heat flux L_wE and the sensible heat flux H from a bare soil can be defined as:

$$L_w \cdot E = L_w \cdot \left(\frac{\rho_s - \rho_a}{r_a} \right) \qquad 2.32$$

$$H = C_a \frac{T_s - T_a}{r_H} \qquad 2.33$$

where ρ_s [kg m^{-3}] and T_s [K] are the water vapor density and temperature at the soil surface, ρ_a [kg m^{-3}] is the water vapor density measured in the air at a certain height above the soil surface, r_a [s m^{-1}] is the atmospheric resistance to water vapor flow, and C_a [J m^{-3} K^{-1}] the volumetric heat capacity of air. In Equation 2.33, r_H [s m^{-1}] is the aerodynamic resistance to heat flow and T_a [K] is the air temperature. Since vapor flow in the soil is modeled as a function of vapor density gradients and vapor diffusivity in soils, the reduction of the vapor flux due to a resistance to vapor flow within the soil is explicitly accounted for and not parameterized as a soil resistance in a model that predicts the vapor transfer from the soil surface to the atmosphere (van de Griend and Owe, 1994).

The energy balance equation is used to provide surface fluxes for heat as well as for water (Camillo et al., 1983). Solving the energy balance for each time step during the numerical simulation yields the heat flux density G. Soil heat flux G and the evaporation rate E are used as heat and water flux boundary conditions for the top of the soil profile, respectively. In case of precipitation, the sum of precipitation and evaporation rate is used as a flux boundary condition for water flow.

The calculated evaporation flux, E, defines the water and vapor flux at the soil surface:

$$\frac{E}{\rho_w} = q_v + q_l \Big|_{z=0} \qquad 2.34$$

and the calculated heat flux, G, defines the heat flux into the soil:

$$G = -q_h \big|_{z=0} \qquad 2.35$$

The negative sign follows from definitions of G and q_h, fluxes are negative downward and positive upward.

The evaporation rate E includes both the liquid water flux towards the soil surface, which is evaporated at the soil surface, and the water vapor flux at the soil surface. The total heat flux into the soil G comprises the conductive and convective heat fluxes and the latent heat flux due to vapor flux $L_0 q_v$ in the soil profile. If G is written as:

$$G = -L_0 q_v - q_{h,nonlatent} \qquad 2.36$$

where $q_{h,nonlatent}$ is the heat flux in the soil that is not caused by latent heat flow. Thus $q_{h,nonlatent}$ increases (in absolute terms) with q_v to provide energy for evaporation within the soil profile. In a dry soil where most of the water is evaporated within the soil profile and the evaporation rate approximates to $E \approx \rho_w \, q_v|_{z=0}$, it follows from the surface energy balance that $-q_{h,nonlatent} = R_{net} - H$.

For a wet soil profile, $q_v|_{z=0} \approx 0$, $E \approx \rho_w \, q_l|_{z=0}$ and $-q_{h,nonlatent} = R_{net} - H - L_0 \, q_l|_{z=0.}$ In a wet soil, the latent heat is consumed at the soil surface. Thus, including vapor flow in soil water flow model leads to the prediction of lower soil surface temperatures when vapor flow in the soil contributes significantly to the evaporation rate.

2.3 Infrared thermography

In Section 4, the assessment of soil surface temperatures using infra-red (IR) measurement techniques (IR thermography) plays an important role. Therefore, the theoretical approach of measuring IR temperatures using an IR camera is given.

The basic principle of infrared thermography is the observation that every object with a temperature above 0° K emits electromagnetic radiation based on its physical temperature. If measured, the intensity of this radiation can be used to determine its temperature without contact. Temperature is a measure of the internal energy within an object and depends on the macroscopic average of kinetic energy of the atoms or molecules of which the object is composed. Consequently a distribution of wavelengths and intensities is radiated by an object of a single physical temperature. The emissive power of radiation as a function of wavelength and temperature, assuming a black body, is known as *Planck's Law* (Figure 2.1)

$$I^{BB}(\lambda,T)=\frac{2h_Pc^2}{\lambda^5}\left(e^{h_Pc/\lambda kT}-1\right)^{-1} \qquad 2.37$$

where $I^{BB}(\lambda,T)$ [J s^{-1} m^{-2} sr^{-1} m^{-1}] is the spectral radiance as a function of wavelength λ [m] and temperature T [K] of a blackbody, h_P [J s] is the Planck constant, c [m s^{-1}] is the speed of light and k [J K^{-1}] is the Boltzmann constant (Gaussorgues & Chomet, 1994).

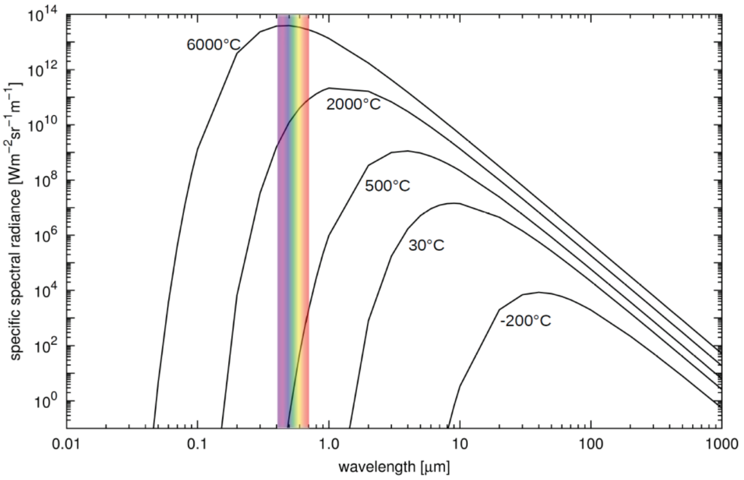

Figure 2.1: Spectral radiance of a blackbody as a function of temperature and wavelength described by Planck's Law. Between approximately 0.4 and 0.8 µm (400 – 800 nm) the spectral range of visible light can be seen. (Figure based on data provided by Gaussorgues & Chomet, 1994)

Planck's Law is only valid for a blackbody, which is defined to absorb all incoming electromagnetic radiation, independent of wavelength or temperature. Thus, radiation emitted from a blackbody does not contain radiation reflected from other radiating sources. As no blackbodies exist in nature, the ability of a real object to absorb or emit is described by its emissivity ε [-]. A real object which is assumed to have the same emissivity over a certain spectral range (e.g. within the IR band) is called a grey body. The emissivity is defined as the radiation emitted by a grey body relative to the radiation of a blackbody at the same temperature.

$$\varepsilon = \frac{I(T)}{I^{BB}(T)} \qquad 2.38$$

where $I(T)$ [J s^{-1} m^{-2} sr^{-1} m^{-1}] is the spectral radiance at a temperature T [K] of a grey body. From Eq. 2.38 can be seen that the emissivity is $\varepsilon = 1$ for a blackbody and $\varepsilon < 1$ for a real object.

It can be seen from Figure 2.1 that the peak wavelength (λ_{Peak}) is also a function of the temperature, expressed by *Wiens Displacement Law*

$$\lambda_{Peak} = \frac{b_{Wien}}{T} \qquad 2.39$$

where b_{Wien} [μm K] is Wien's displacement constant (2897.8 μm K). Using Equation 2.39 shows that the sun with a temperature of ~5800 K emits radiation with peak wavelengths within the visible spectral range (Figure 2.1). In contrast, objects with a temperature around room temperature (300 K) emit radiation within the IR spectral range (Figure 2.2) (Gaussorgues & Chomet, 1994). Hence, in IR imaging thermography, unlike in other visible imaging techniques, most objects are a source of radiation, not only the reflector of a source. This allows not only visible imaging, but also inferring of the temperature of an observed object and thus making IR thermography useful for a wide range of applications.

The distance between object and camera and physical properties of the measured object itself influence the radiation registered by the IR camera. Thus, the measured radiation needs to be modified to consider potential error sources:

Infrared thermography is a non-invasive measurement and radiance emitted from an object may be influenced by infrared optical properties of the measurement distance from object to camera. Depending on the wavelength, air (i.e. carbon dioxide and water vapor) can absorb infrared radiation. Between 2 – 5 μm and 8 – 14 μm the transparency of air to IR radiation is constant and close to 100% (no IR radiance is absorbed) (Gaussorgues & Chomet, 1994). Therefore, most thermographic IR-imagers have a spectral sensitivity in one of the mentioned wavelength ranges.

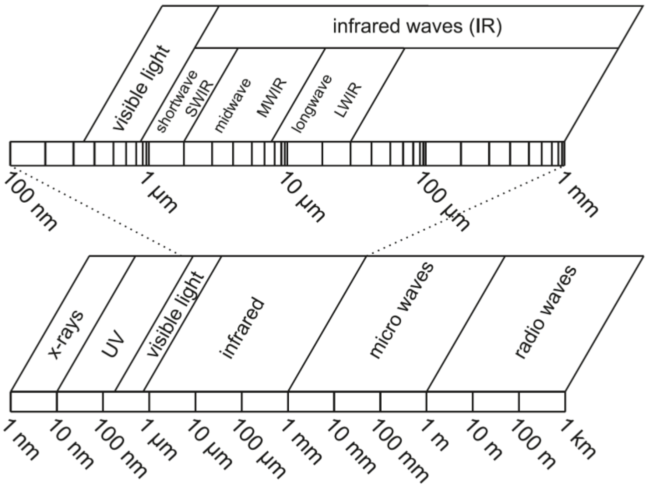

Figure 2.2: Wavelengths and their classifications between 1nm and 1km. The IR spectral band ranges from ~ 0.8 µm to 1 mm and is divided into shortwave (SWIR, 0.8 – 2 µm), midwave (MWIR, 2 – 6 µm) and longwave (6 – 20 µm) infrared spectrum. (Figure based on data provided by Gaussorgues & Chomet, 1994)

An object with an emissivity of ε and a temperature of TO emits radiance Φ_e [J s-1 m-2], which can be calculated as

$$\Phi_e = \varepsilon \cdot \Phi(T_O) \quad 2.40$$

where $\Phi(T_O)$ [J s^{-1} m^{-2}] is the radiance emitted from a blackbody at the same temperature. A grey body has an emissivity lower then 1, therefore a part of the radiance coming from the grey body is reflected (Eq. 2.41). In case of a transparent object, radiance may also be transmitted by the measured medium (Figure 2.3) (Eq. 2.42).

$$\Phi_r = \sigma \cdot \Phi(T_A) \quad 2.41$$

$$\Phi_t = \tau \cdot \Phi(T_{BG}) \quad 2.42$$

where Φ_r [J s^{-1} m^{-2}] and Φ_t [J s^{-1} m^{-2}] are the reflected and transmitted radiances, respectively, $\Phi(T_A)$ [J s^{-1} m^{-2}] is the radiance of the surrounding area which depends on the ambient temperature T_A, $\Phi(T_{BG})$ [J s^{-1} m^{-2}] is the radiance of objects behind the measured objects which is a function of the temperature of the objects in the background T_{BG}, σ [-] is the reflectivity and τ [-] is the transmittance. The total radiance of a measured grey body Φ_O [J s^{-1} m^{-2}] can be described as:

$$\Phi_O = \Phi_e + \Phi_r + \Phi_t \tag{2.43}$$

It can be seen that the sum of the total fractions of radiance emitted, reflected and transmitted equals the total radiance coming from an object. It follows that

$$\varepsilon + \sigma + \tau = 1 \tag{2.44}$$

for a semi-transparent medium. In case of a non-transparent ($\tau = 0$) object, Equation 2.44 reduces to

$$\varepsilon + \sigma = 1 \tag{2.45}$$

and the total emitted radiance Φ_O [J s^{-1} m^{-2}] from a measured medium can be written as:

$$\Phi_O = \varepsilon \cdot \Phi(T_O) + \sigma \cdot \Phi(T_A) \tag{2.46}$$

Depending on wavelength and distance between measured medium and IR camera, Φ_O may be reduced according to the transmittance of the measurement distance (i.e. air) (Gaussorgues & Chomet, 1994).

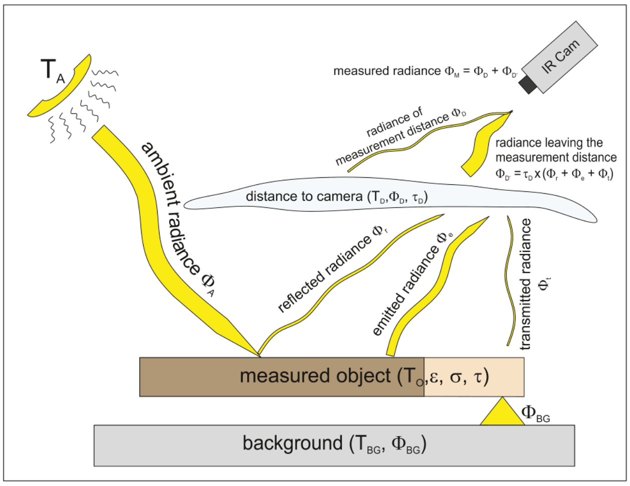

Figure 2.3: Schematic illustration of an IR measurement arrangement. Different components of the total radiance measured by the IR camera are discussed in the text.

$$\Phi_{D'} = \tau_D \cdot \Phi_O \qquad 2.47$$

where τ_D [-] is the transmittance of the measurement distance and $\Phi_{D'}$ [J s^{-1} m^{-2}] is the radiance leaving the measurement distance, which can emit radiance depending on its temperature and transmittance according to

$$\Phi_D = (1 - \tau_D) \cdot \Phi(T_D) \qquad 2.48$$

where Φ_D [J s^{-1} m^{-2}] is the radiance emitted by the measurement distance and T_D [K] is the temperature of the measurement distance.

Hence, the total radiance registered by the camera Φ_M [J s^{-1} m^{-2}] is

$$\Phi_M = \Phi_D + \Phi_{D'} = (1 - \tau_D) \cdot \Phi(T_D) + \tau_D \cdot \Phi_O \qquad 2.49$$

Using Equations 2.45 and 2.46 in Equation 2.49 yields the basic model of radiation physics used in most thermographic and pyrometric systems:

$$\Phi_M = (1 - \tau_D) \cdot \Phi(T_D) + \tau_D \cdot (\varepsilon \cdot \Phi(T_O) + (1 - \varepsilon) \cdot \Phi(T_A)) \qquad 2.50$$

In chapter 4, an IR-camera is used to determine soil surface temperatures. Details about camera and used thermography parameters can be found in Section 4.2.2.

3 Coupled water and heat modeling in soils

3.1 Introduction

Numerical models considering coupled heat and water flow are used for various applications in different research fields: In civil engineering coupled heat and water fluxes play a role in environmental effects such as urban heat islands (e.g. Arnfield, 2003). Asaeda and Ca (1993) used the coupled heat and water flux theory to study transport of water and heat under covered surfaces such as asphalt and concrete leading to urban heat islands and concluded that underground transfer of heat cannot be predicted properly without considering coupled heat and vapor fluxes. In another engineering application coupled heat and water is known to play an important role in modeling of geothermal fields (Faust & Mercer, 1979; Battistelli, 1997). Diao et al. (2004) studied the impact of groundwater flow on performance of geothermal heat exchangers using a coupled heat and water model and postulate that groundwater advection alters conductive heat distribution and therefore influences the effectiveness of ground-coupled heat pumps. In military applications, the accurate prediction of moisture and temperatures near the soil surface is required to allow detection of landmines (Šimůnek et al., 2001). Also showing the broad usage of numerical models considering simultaneous flow of water and heat is a publication by Farnworth (1986), who studied combined heat and water vapor transport in multi-layered clothing and states that, apart from heat loss by conduction and thermal radiation, heat may also be lost by evaporation of water (sweat) and subsequent diffusion of water vapor through the individual clothing layers.

Since Philip & de Vries' (1957) theoretical description of coupled heat and water movement in soils, several models considering vapor flow and/or water-heat interactions were presented (e.g. Rose, 1968a; Milly 1982; Noborio et al., 1996b; Friedel, 2005; Saito et al., 2006; Seetharam et al., 2007; Bittelli et al.; 2008). To study coupled heat and water transport in porous media and its effect in different applications, a modification the well-tested model HYDRUS-1D, considering vapor flow and thermally induced water (vapor) movement, is used. Governing equations describing the difference between coupled and non-coupled modeling can be found in Section 2.1.

3.2 Comparing coupled and non-coupled modeling

In soil sciences, movement of water is mostly represented by the classical *Richards equation* (Eq. 2.5), which describes water movement due to a hydraulic gradient. However, liquid water may move due to a temperature gradient or evaporate at one place in the soil and condensate at another, thereby following hydraulic and thermal gradients within the soil. This movement of water was found to be important especially for dry soils (Scanlon & Milly, 1994; Grifoll et al., 2005; Akinyemi and Mendes, 2007; Goss & Madlinger; 2007) and can only be modeled accurately by considering processes such as water vapor movement and movement of water (liquid or vapor) due to a hydraulic and a thermal gradient.

Milly (1984) found that the effect of coupled modeling on cumulative evaporation was small. However, the effect of coupled heat and water flow could be more important when diurnal variations of evaporation rates and of soil surface states (soil moisture and soil temperature) are of interest. Using IR thermography (or other non-invasive methods such as active and passive radar or eddy covariance measurements), these soil surface state variables and fluxes can be measured with high temporal resolution. A proper interpretation of these measurements therefore requires models that account for or consider all relevant physical processes that influence or determine these state variables and fluxes.

To understand the effects of coupled heat-water fluxes on simulated soil evaporation, soil surface temperature and soil moisture content, numerical experiments comparing coupled and non-coupled modeling for wet and dry soil are performed.

3.2.1 Reference model setup

For modeling, a 100 cm deep soil profile with van Genuchten – Mualem hydraulic parameters representing a loamy soil was used and evaporation, temperature and water content over a time period of five days was modeled. The thermal conductivity function of Chung & Horton (1987) (Eq. 2.30) provided in HYDRUS-1D were used and thermal parameters were chosen to represent a loamy soil. Resulting hydraulic and thermal parameters can be found in Table 3.1.

Table 3.1 Hydraulic (van Genuchten - Mualem) and thermal (Chung & Horton) parameters used for modeling.

hydraulic properties (van Genuchten – Mualem 1980)	θ_s	θ_r	α	n	K_s	l
unit	[cm^3 cm^{-3}]		[cm^{-1}]	[-]	[cm d^{-1}]	[-]
	0.45	0.02	0.03	1.38	34.2	0.5
thermal parameters (Chung & Horton 1987)	b_1		b_2		b_3	
unit			[W m^{-2} K^{-1}]			
	24.3		39.3		153.4	

During evaporation, the top soil dries out and consequently develops steep gradients in pressure head. Hence dynamics in temperature and water content are expected to be strongest close to the soil – atmosphere boundary (Bitelli et al. 2008). Therefore model domain discretization was chosen to be small closest to the surface (0.33 cm), increasing with depth. This results in a model domain with 101 nodes and 100 elements.

Two different model scenarios representing a wet soil and a dry soil were used to quantify the differences between coupled and non-coupled modeling. Initial water content for the wet and the dry scenario was set to be homogenous (dry: 0.14 cm^3 cm^{-3}, wet: 0.43 cm^3 cm^{-3}) for the whole soil profile. Initial conditions for the temperature in both scenarios were variable with depth: Temperature at the top of the profile was set to 17°C and temperatures from -50 cm to -100 cm depth (bottom of the profile) were set to 10°C. Temperatures between 0 cm and -50 cm depth were interpolated linearly.

Solution of the energy balance equation requires meteorological data such as net radiation, air temperature, relative humidity, wind speed, and precipitation. These data were taken from a weather station at Research Center Jülich measured between 18th of September 2006 and 22nd of September 2006 (Figure 3.1). Meteorological data shows a period of less than one day of rain followed by more than 4 days of high potential evaporation rates (0.5 – 0.8 cm d^{-1}).

An energy balance boundary condition (BC) was used to provide heat and water fluxes at the top of the soil profile. Section 2.2 gives an overview of the implementation of this energy balance equation in HYDRUS. As lower boundary condition for water flow a free drainage BC was used. A third type (Cauchy) BC was chosen as lower BC for heat transport.

Both scenarios (dry and wet initial conditions) were simulated with a coupled and a non-coupled version of H1D.

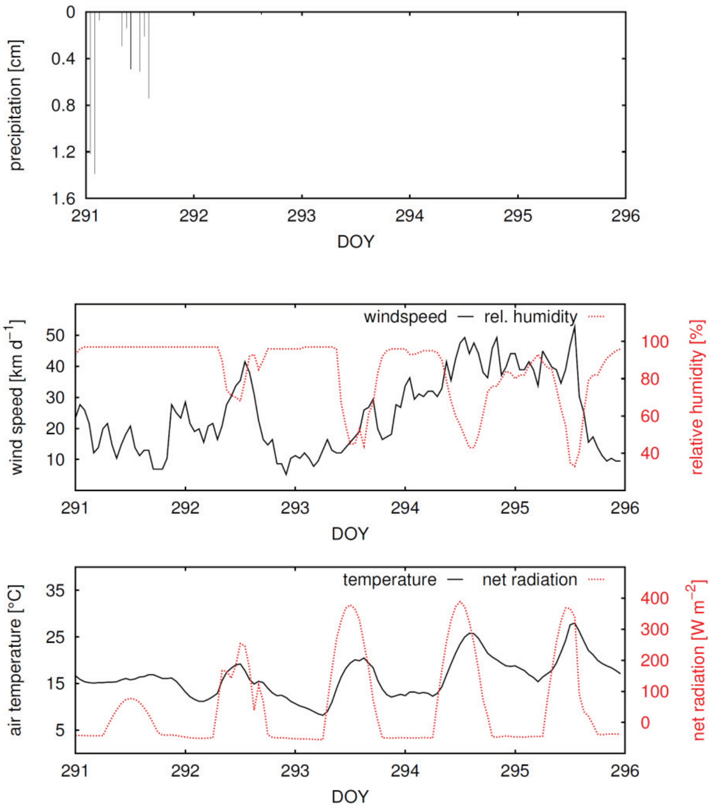

Figure 3.1: Meteorological parameters measured at Research Center Jülich from September 18th to 22nd of 2006.

3.2.2 Results and discussion

Under wet initial conditions, coupling of heat and water does not have a noticeable effect on the modeling results (Figure 3.2). Soil surface temperature (SST) / moisture (SSM) and actual evaporation (EP) show the same development over the modeling period. This means that neither liquid water flux due to a temperature gradient nor thermal or isothermal water vapor flux does have an effect on the overall water or heat balance.

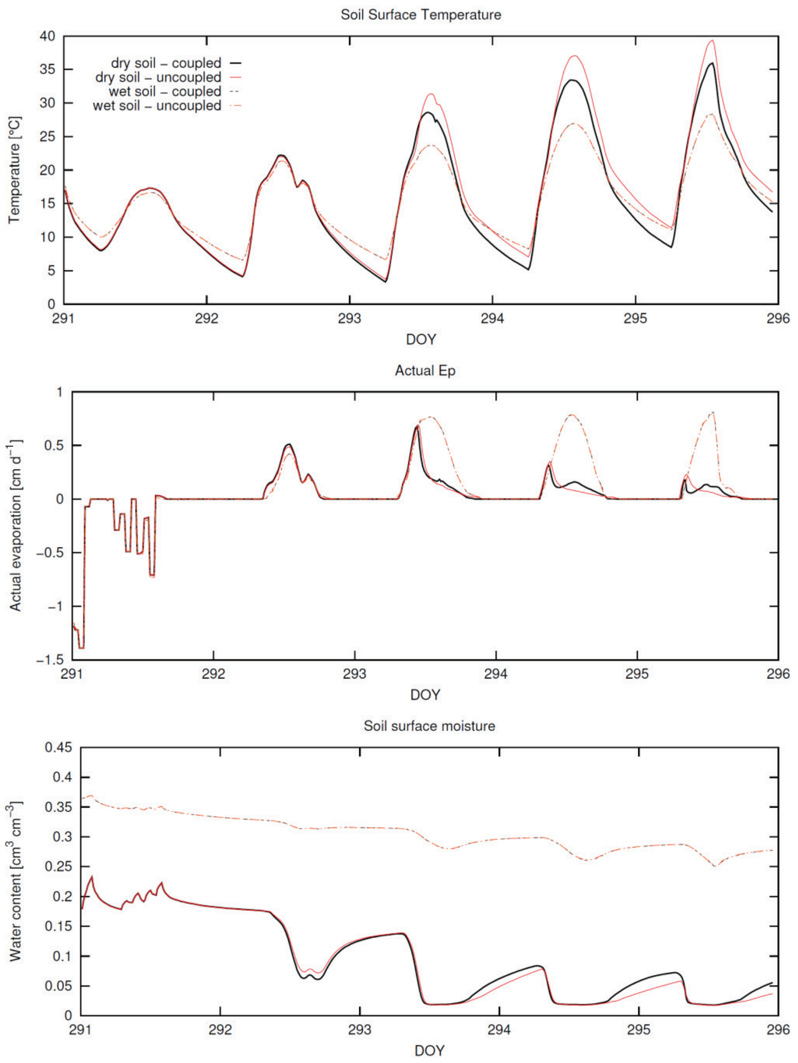

Figure 3.2: Comparing coupled (black) and non-coupled (red) water and heat modeling using wet (dashed) and dry (solid) initial conditions. Boundary conditions, thermal and hydraulic parameters, and meteorological input in coupled and non-coupled approach are identical.

Using dry initial conditions shows differences between coupled and non-coupled modeling. These differences are relatively small at the beginning (DOY 291 – 293.5), but are increasing with ongoing drying of the soil (DOY 293.5 – 296). Peak soil surface temperatures in the coupled modeling approach are significantly lower during day and night compared to the non-coupled approach. For both approaches, highest temperatures are calculated around noon, lowest temperatures early in the morning. The soil surface moisture shows differences during night, where higher water contents and a faster wetting are calculated with the coupled model. Until DOY 294, differences in evaporation rate calculated from coupled and non-coupled approach are relatively small. These differences become more striking, when the soils evaporation rate decreases from potential to actual evaporation.

Because of the distinct differences between coupled and non-coupled modeling on DOY 294, discussion of the described trends will focus on this day. In the uncoupled approach, the SST of DOY 294 around 01:30 pm shows a peak temperature of approximately 37°C, whereas the coupled model calculates a peak temperature of ~33°C (Figure 3.3). Water content and evaporation rate development also differs between coupled and uncoupled modeling.

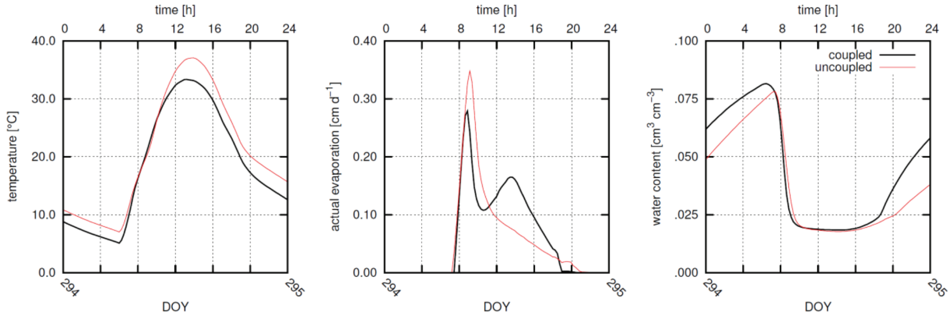

Figure 3.3: Development of soil surface temperature, actual evaporation and soil surface moisture between DOY 294 and DOY 295. Red lines and black lines show the results for uncoupled and coupled modeling approach, respectively.

During soil-atmosphere interactions, soil surface temperature and moisture are coupled by evaporation from the soil, which consumes heat by changing the aggregate state of water from liquid water to water vapor. Water vapor leaves the soil, thereby reducing the total water content and removing latent heat from the soil. As can be seen from Figure 3.2, water accumulates at the soil surface during night. With sunset around 08:00 am, water at the soil surface evaporates fast, again reducing the SSM to a residual water content of ~0.02 cm^3 cm^{-3}. Following the sunset, evaporation between 08:00 am and 16:00 pm behaves differently in non-coupled and coupled approach. EP in the uncoupled approach decreases over the day, whereas the EP in the coupled model increases again around 10:00 am and reaches a maximum around 13:00 pm. Considering water vapor flow in the coupled model causes the evaporation rates to be calculated differently: With increasing incoming radiation and air temperatures (Figure 3.1) during the day, the soil is heating up. As the soil surface is reduced to its residual water content, evaporation takes place in deeper regions of the soil and the resulting water vapor leaves the soil. The evaporation rate increases as long as the incoming radiation heating up the soil increases. Heating up of the soil also leads to an increase in the saturated vapor pressure so that hotter air contains more moisture and the evaporation rate follows the evolution of temperature. Consequently, in the coupled model, there should be a loss of latent heat, which induces a cooling effect to the soil. Figure 3.2 also shows a larger increase in soil moisture during night. This is due to thermal vapor fluxes directed upward in the coupled approach and will be discussed in more detail in Section 3.3.

As mentioned before, the wet soil shows no differences between coupled and non-coupled modeling. In contrast to this result, Milly (1984) reports slight differences in evaporation even for wet soils. Note that Milly (1984) performed numerical experiments using a sandy soil, which is drying faster than the loamy soil used in this simulation. Usage of a sandy soil results in a fast reduction of the SSM making the water vapor flow more and more important and finally causing different EP rates.

Generally, shown results and Milly’s (1984) numerical experiment indicate that even a relatively short-termed modeling period can, depending on the soil’s texture, dry the soil to an extent that erroneous results are produced if coupling of heat and water is not taken into account. These errors may be especially important when modeling soil surface temperatures (see Section 4), because small deviations in evaporation rate can cause relatively large errors in modeled soil surface temperature.

3.3 Water flux components in coupled heat and water modeling

The modified *Richards equation* (Eq. 2.10) defines that liquid water and water vapor flux components, both following a thermal and a hydraulic gradient, define the net water content development over time. Thermal liquid water and thermal water vapor flow are following temperature differences within the soil, whereas isothermal liquid water and isothermal water vapor fluxes are following the hydraulic gradient. On the other hand, the original *Richards equation* (Eq. 2.5) only considers isothermal liquid water flux. Hence, the additional three flux components (thermal liquid and vapor flux; isothermal vapor flux) considered in the modified *Richards equation* affect the net water flux in a way that coupled modeling under dry conditions yields different results compared to uncoupled modeling (using the original *Richards equation)*. Section 3.2 shows that coupling of water and heat affects soil state variables as soil temperature and soil moisture.

To quantify the importance of the different flux components under evaporative conditions in dry soils, the reference coupled model setup described in Section 3.2.1 is used. with coupled modeling approach and assuming dry initial conditions .

As the importance of the different flux components are different depending on the soil water content, DOY 292 is discussed as an example for a relatively wet soil and DOY 294 as an example for a relatively dry soil.

For wet initial conditions, Figure 3.2 shows that differences between coupled and uncoupled approach are small on DOY 292. Therefore, the additional three flux components considered in the modified *Richards equation* are expected to have a negligible effect on the net water flux. Figure 3.4 shows that the isothermal liquid flux is dominant on DOY 292.

Due to evaporation at the soil surface, a hydraulic gradient develops close to the soil surface. Liquid water flux occurs due to this hydraulic gradient and is directed to the soil surface where it evaporates and leaves the soil.

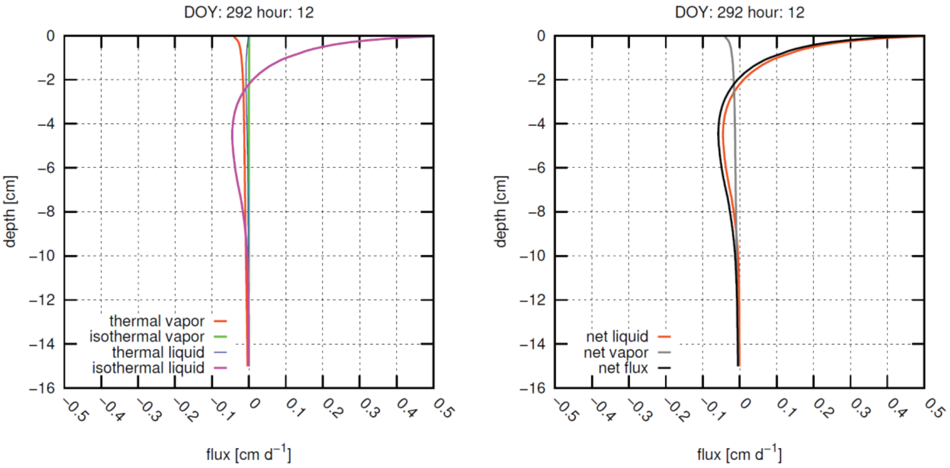

Figure 3.4: (left) Flux components calculated with the coupled heat and water modeling approach using the modified *Richards equation* and (right) overall net water flux consisting of the net liquid and net vapor flux. Both figures show the flux densities over the first 15 cm of the soil profile on DOY 292, 12 pm. Positive values indicate upward fluxes (out of the profile).

Thermal liquid flux is small in all simulations. According to Milly (1984) liquid water flux may be of importance in saturated or waterlogged systems in existence or shortly after a sufficiently heavy rainfall and is otherwise negligible. This corroborates with Jackson et al. (1973 a, b), who studied water flux components at 5 mm depth in a field experiment.

Isothermal vapor flux depends on a gradient in the actual vapor pressure (depending on the pressure head) prevailing in the soil profile. Hence, the isothermal vapor flux can be written as

$$q_{vh} = -\frac{D}{\rho_w}\frac{d\rho_v}{dh}\frac{\partial h}{\partial z} \qquad 3.1$$

where ρ_v [kg m^{-3}] is the vapor density. Assuming equilibrium between the liquid and vapor phases of water in soil, the vapor densities can be expressed as the product of saturated vapor density (Eq. 2.21) and relative humidity (Eq. 2.20).

$$\rho_v = \rho_{sv} \cdot H_r \qquad 3.2$$

Using Equation 3.2 and assuming that ρ_{sv} does not depend on the pressure head, Equation 3.1 can be rewritten as

$$q_{vh} = -\frac{D}{\rho_w} \rho_{sv} \frac{dH_r}{dh} \frac{\partial h}{\partial z} \tag{3.3}$$

Inserting Equation 2.20 in Equation 3.3 and differentiating that part with respect to yields

$$q_{vh} = -\frac{D}{\rho_w} \rho_{sv} \frac{Mg}{RT} H_r \frac{\partial h}{\partial z} = -K_{vh} \frac{\partial h}{\partial z} \tag{3.4}$$

which describes the isothermal vapor flux based on the relative humidity and is used in the HYDRUS software packages.

On DOY 292, the water content at the soil surface is ~0.1 cm^3 cm^{-3} (Figure 3.5), which corresponds to a pressure head of approximately -2500 cm for the loamy soil used in our experiment. According to Eq. 2.20 and assuming a temperature of 21 °C (Figure 3.5), the relative humidity of air in the soil at the surface is close to 100%.

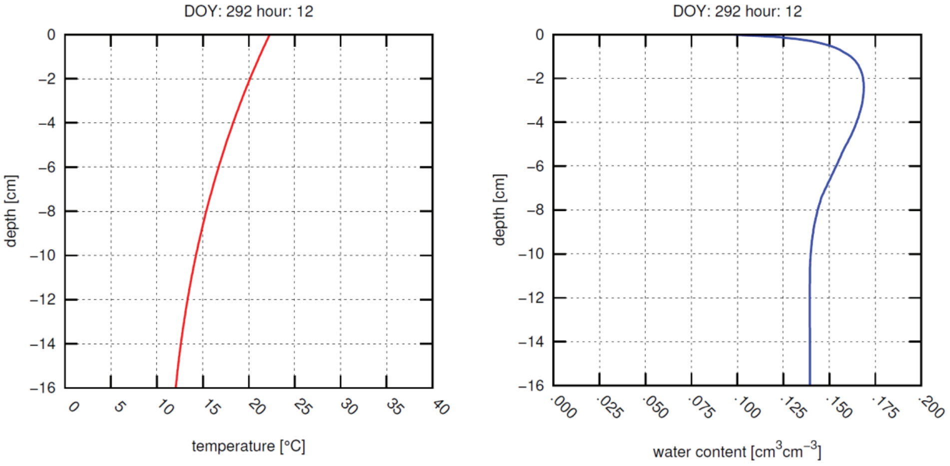

Figure 3.5: (left) Soil temperature and (right) soil water content profiles from 0 cm to 16 cm depth on DOY 292, 12 pm.

Looking at Eq. 3.4 shows that the isothermal vapor hydraulic conductivity strongly depends on the soil vapor diffusivity D [m^2 s^{-1}]. The soil vapor diffusivity itself depends on the volumetric air filled porosity (Eq. 2.16). In wet soils, the air filled porosity is close to zero and consequently, the isothermal vapor hydraulic conductivity becomes small.

Physically, this means that vapor flow is hardly possible, because there is no air filled porosity within a wet soil.

Thermal vapor flux follows the temperature gradient in the soil profile and opposes the isothermal liquid flow (Figure 3.4). It is defined by the actual vapor pressure following the gradient in soil temperature, enhanced by an increase of the thermal vapor flux as a result of condensation on and evaporation from liquid islands in the air phase described by the enhancement factor η.

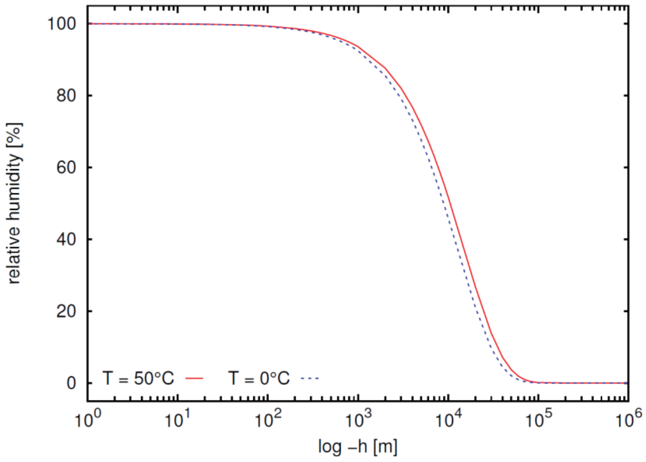

Figure 3.6: Dependence of the relative humidity of soil air on the pressure head as described by Equation 2.20 at temperatures of 323 K. (50°C, solid red) and 273 K (0°C, dashed blue).

Recently, the enhancement factor has been subject to discussion and its necessity has been doubted (e.g. Shokri et al., 2009). For a more detailed discussion on the enhancement factor, refer to Section 3.4. The thermal vapor flux can be expressed as:

$$q_{vT} = -\frac{D}{\rho_w}\eta\frac{d\rho_v}{dT}\frac{\partial T}{\partial z} \qquad 3.5$$

According to Figure 3.6, the dependence of the relative humidity of soil air on the temperature is assumed to be negligibly small. Therefore, using Equation 3.2, Equation 3.7 can be rewritten as

$$q_{vT} = -\frac{D}{\rho_w}\eta H_r \frac{d\rho_{sv}}{dT}\frac{\partial T}{\partial z} = -K_{vT}\frac{\partial T}{\partial z} \quad 3.6$$

where the thermal vapor flux is described depending on the saturated vapor pressure, which is a function of the temperature (Eq. 2.21). During day, the soil surface heats up and an upward temperature gradient (temperatures decrease with increasing depth) develops. As the saturated water vapor pressure increases with temperature, vapor moves from top of the soil profile, where vapor pressure is higher, to deeper parts of the soil profile, where vapor pressure is lower. Hence, on DOY 292, 12 pm thermal vapor flux is directed into the soil.

Further discussion will focus on DOY 294 in the dry soil, when the coupling of heat and water affects evaporation rate, surface temperature, and surface moisture (Figure 3.2). Additionally, the distribution of the different flux components over depth shows a typical development on DOY 294. As the direction and the velocities of the different flux components vary over the day, the development of the fluxes and their effects on soil state variables such as evaporation and surface temperature is discussed on a diurnal basis. Soil temperature and water content profiles for all times discussed in the following section can be seen in Figure 3.7.

At 8 am for reasons stated above, isothermal vapor and thermal liquid flux are negligible. In general, fluxes in the soil are relatively small in the morning (Figure 3.8). Thermal vapor flux directed downwards due to the temperature gradient and isothermal liquid flux directed upwards due to the hydraulic gradient are dominant. This leads to a net liquid water flux out of the profile close to the soil surface. On the other hand, net water vapor flux is directed downwards.

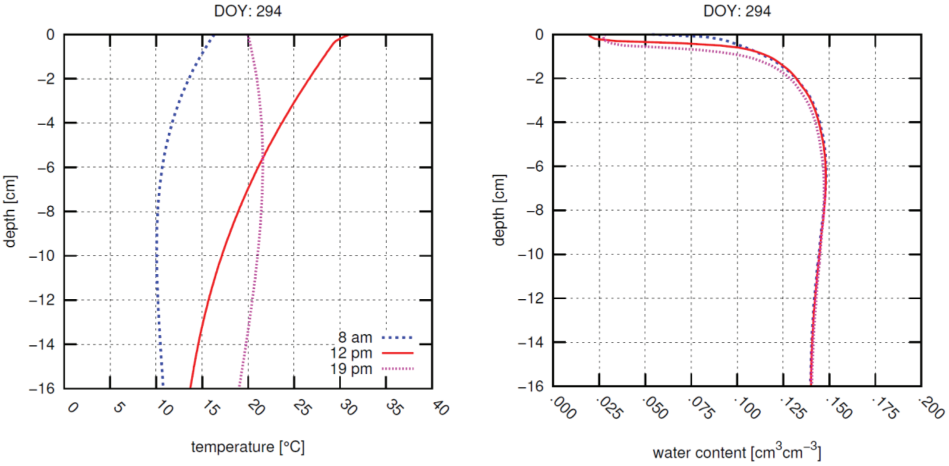

Figure 3.7: Soil profiles for (left) temperature and (right) water content fort the top 16 cm of the soil profile. The dashed blue line shows the profiles at 8 am, solid red at12 pm and dotted magenta at 19 pm.

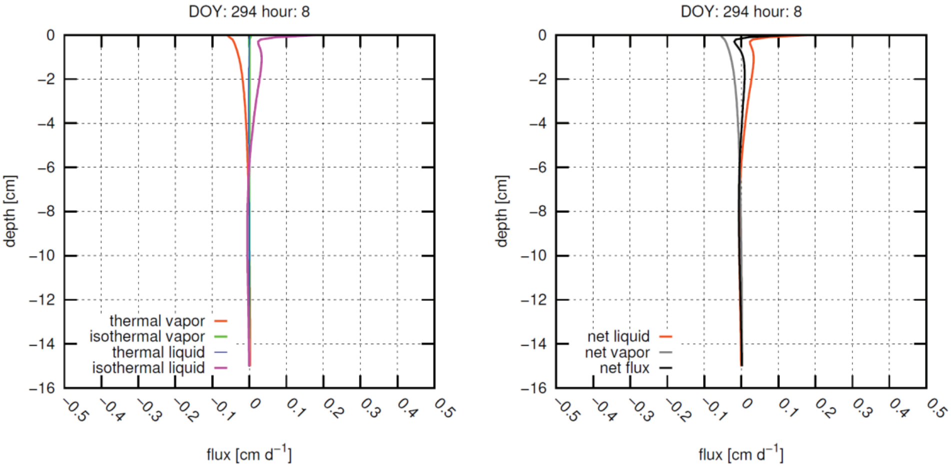

Figure 3.8: (left) Distribution of the four different water flux components on DOY 294, 8 am and (right) overall net water flux consisting of the net liquid and net vapor flux for the top 15 cm of the soil profile. Fluxes are positive out of the profile.

This leads to a distinct net water flux (liquid + vapor), which is directed out of the soil profile on top (dominated by the net liquid flux) and directed downward directly beneath the top of the profile (dominated by the net vapor flux). In terms of evaporation, this means that EP rates on DOY 294, 8 am are lower using a coupled modeling approach in comparison to an uncoupled approach (Figure 3.3), because water potentially available for evaporation is directed into the soil profile by thermal water vapor flux.

At 12 pm, liquid water flux at the top of the profile (~ 0.5 cm) is reduced strongly down to zero flux, while isothermal vapor flux increases at the same depth. This implies that water changes its phase from liquid water to water vapor, making isothermal water vapor the dominant flux component at the top of the profile. Thus, evaporation does not take place at the surface, but at a certain depth within the profile, which will be refer to as “evaporation depth” for the remainder of this section.

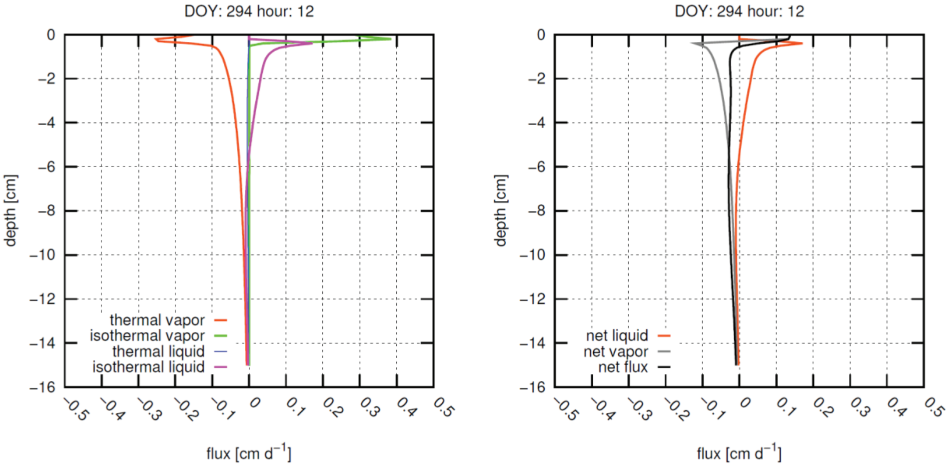

Figure 3.9: (left) Distribution of the four different water flux components on DOY 294, 12 pm and (right) overall net water flux consisting of the net liquid and net vapor flux for the top 15 cm of the soil profile. Fluxes are positive out of the profile.

Flux component distributions above and below the evaporation depth are different: Below the evaporation depth, a large downward thermal vapor flux is reduced by an upward isothermal liquid water flux, leading to an overall net water flux into the profile. Above the evaporation depth, thermal and isothermal water vapor are the important flux components, isothermal flux being dominant. As a result, net vapor and overall net water flux (Figure 3.9) are directed out of the profile. Between 10 am and 14 pm, the absolute difference between isothermal and thermal vapor flux close to the soil surface increases (absolute isothermal > absolute thermal) and the isothermal liquid water flux remains negligible. Hence, the overall net water flux out of the profile increases between 10 am and 14 pm, which explains the increased evaporation rate from the coupled approach compared to the evaporation rate from the uncoupled approach seen in Figure 3.3.

At 19 pm fluxes are small again (Figure 3.10). The evaporation depth has retreated deeper into the profile.

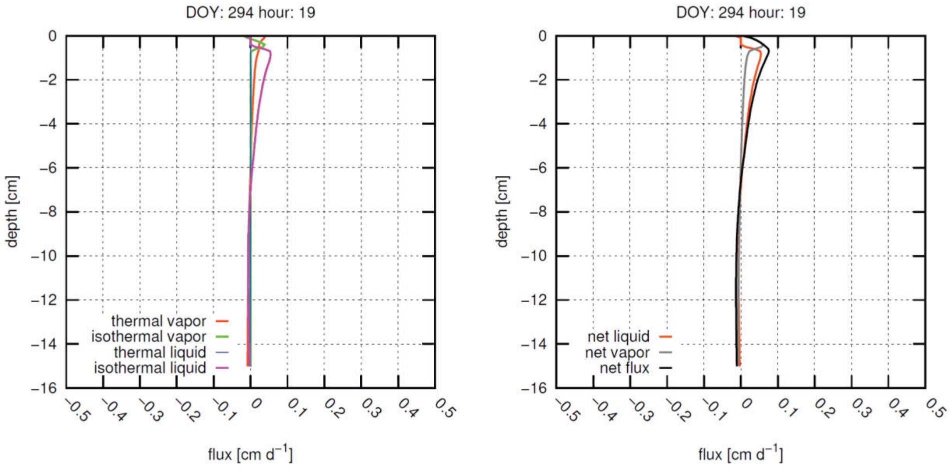

Figure 3.10: (left) Distribution of the four different water flux components on DOY 294, 19 pm and (right) overall net water flux consisting of the net liquid and net vapor flux for the top 15 cm of the soil profile. Fluxes are positive out of the profile.

Fluxes below the evaporation depth are dominated by an upward isothermal liquid water flux. In contrast to the thermal vapor flux direction at 8 am and 12 pm (downward), the thermal vapor flux is directed upward, as a result of the soil profile temperatures, which are increasing with height up to a depth of approximately 7 cm. Above the evaporative depth, isothermal and thermal vapor fluxes are dominant. Both fluxes are directed upward, resulting in an upward overall water flux above the evaporation depth. The upward net vapor flux decreases with height close to the surface. This indicates that condensation takes place within the soil profile.

Generally during evening and night, the net water flux from a depth of ~ 8cm is directed upward in both, coupled and non-coupled modeling approach. Because evaporation during night is almost zero, the upward flow leads to an accumulation of water close to the soil surface, which can be seen in Figure 3.2. However, accumulation of water is faster using the coupled approach compared to the non-coupled approach (Figure 3.2). This is due to the net water vapor flux, which is directed upward and adds to the total water content at the soil surface.

3.4 Enhanced water vapor movement in soils

The HYDRUS software packages use water vapor diffusion enhancement factors as defined by Cass et al. (1984) to explain reported differences between experimental measurement and theoretical prediction of water vapor diffusion in soils.

Recent studies (e.g. Shokri et al., 2009; Ho & Webb, 1998) critically evaluated the usage of water vapor diffusion enhancement factors. In their study Shokri et al. (2009) used laboratory evaporation experiments and neutron transmission techniques to analyze the continuity of capillary induced liquid flow and conclude that the diffusion of the total vapor flux in soils can be attributed to a combination of *Fick’s law of diffusion* and capillary flow. Shokri et al. (2009) describe two different evaporation stages for their experiment. A constant drying rate is characteristic for the first stage of evaporation. The receding drying front (primary drying front) remains connected to the soil surface over film and capillary flow and water evaporates at the soil surface. When the liquid connection between drying front and soil surface collapses, stage two of the evaporation process takes place (Lehmann et al., 2008). During this stage water is not evaporating at the surface any longer but at a vaporization plane (secondary drying front), which recedes into the soil with ongoing drying. Shokri et al. (2009) used blue dyed water to visually mark secondary and primary drying front. The drying rate during the second stage of evaporation decreases with respect to vapor diffusion length. Vapor diffusion length itself corresponds with the distance between secondary drying front and soil surface. Shokri et al. (2009) adjusted *Fick’s law* of diffusion with the vapor diffusion length and calculated drying rates for stage two evaporation. Comparison of calculated and measured drying rates shows that *Fick’s law* of diffusion without an enhancement of the diffusion coefficient suffices to correctly describe the drying rate. Therefore, the authors conclude that “with proper account of capillary flow, continuity and pathways, no enhancement factors are needed”.

Additionally, the same research group (Lehmann et al., 2008) postulated the distance between primary and secondary drying front as the evaporative characteristic length, which depends mainly on the pore size distribution of the soil. According to Shokri et al. (2009) the calculated characteristic evaporative lengths for some soil samples used to infer the enhancement factor showed that most soil samples were too short to ignore liquid capillary flow. Therefore Shokri et al. (2009) point out that the inferred enhancement factor could be ascribed also to liquid capillary flow as well as to vapor flux enhancement. However, none of both theories can be ruled out without further experiments.

As Shokri et al. (2009) point out, the original study by Philip & de Vries (1957) offers a thesis to explain differences between measured observations and theoretical calculations of water vapor flux. According to Philip & de Vries (1957), enhanced water vapor diffusion is observed due to two pore-scale processes: First, water vapor condensing at one side of liquid islands and evaporating at the other side. Second, local thermal gradients differing between different phases (air, water and solid) due to non-equilibrium effects at the pore scale. These processes however are based on pore-scale processes and according to Ho & Webb (1998) no direct evidence for enhanced vapor flow processes has been presented. In their study, Philip & de Vries (1957) develop “equations describing moisture and heat transfer in porous materials under combined moisture and temperature gradients”. In this context, they separate the total vapor flux into two components, the isothermal vapor flux due to moisture gradient and the thermal vapor flux due to temperature gradient. Shokri et al.’s (2009) discussion of previous literature concerning enhanced water vapor flow shows that Philip and De Vries theory (1957) is widely used in hydrologic sciences (e.g. Milly, 1984; Cahill & Parlange, 1998; Parlange et al., 1998; Saito et al., 2006; Sakai et al., 2009), on the other hand several studies state that capillary film flow is the dominant transport mechanism, even at low water contents (e.g. Yiotis et al., 2005; Lehmann et al., 2008). Additionally, several experimental studies (e.g. Jury & Letey, 1979; Cary, 1979; Cass et al., 1984; Bach, 1992) concerning parameterization or validation of the enhancement factor were published.

This section cannot address the question whether capillary film flow or enhanced vapor diffusion explains the difference between the theoretical and observed water vapor fluxes. However, it is emphasized that, even though the authors' argumentation is entirely comprehensible and plausible, the laboratory experiment needs to be altered to demonstrate whether or not an enhancement factor for water vapor diffusion in variably saturated soils is needed to describe coupled heat and water flow in porous media. Shokri et al. (2009) performed their experiment under constant air temperatures in the lab using Hele-Shaw cells with no radiation or external heat and do not mention any temperature differences within their soil column. In another evaporation experiment, Hanks et al. (1967) studied evaporation as influenced by drying with wind or radiation and used soil columns with 10 cm in diameter and 45 cm in height. Hanks et al. (1967) performed their laboratory experiment under air temperature controlled conditions (25 ± 2°C), which was also the temperature at the bottom of the soils cores in the beginning of the experiment. Additionally, the soil cores were placed in a box containing 8 cm Styrofoam surrounding the cylinders to prevent lateral heat flow. Temperature at the bottom of the coil cores was not controlled during the experiment. Hanks et al. (1967) report a temperature difference of about 15°C between the temperature at top and bottom of the column at the end of the evaporation experiment (day 40) within the soil column exposed to radiation. In the soil column exposed to wind evaporation, the temperature profile was nearly uniform (< 2°C difference from top to bottom of the column) after 5 days until the end of the experiment. Referring to Hanks et al. (1967), the thermal gradient within the 11 mm thick, non-insulated Hele-Shaw soil column cells used by Shokri et al. (2009) is assumed to be, if any, very small. Therefore the bulk of existing experimental studies concerning enhanced water vapor diffusion analyze systems liable to a temperature gradient. Consequently, I think that laboratory experiments discussing the necessity of the enhancement factor should include experiments subject to a gradient in temperature, where a noticeable effect of thermally driven vapor diffusion is to be expected.

Using the well-tested software package HYDRUS-1D (Šimůnek et al., 2008) different scenarios to analyze the effect of the enhancement factor on soil moisture and temperature profiles as well as evaporation were modeled. HYDRUS features Philip & de Vries (1957) theory to calculate the water vapor transport under isothermal/thermal conditions and solves coupled heat and water flux in variably saturated porous media. Below, relevant equations implemented in HYDRUS-1D calculating water vapor transport in soils are given briefly. HYDRUS defines the total water vapor flux as:

$$q_v = q_{vh} + q_{vT} = -K_{vh}\frac{\partial h}{\partial z} - K_{vT}\frac{\partial T}{\partial z} \qquad 3.7$$

Where q_v [m s^{-1}] is the total water vapor flux, q_{lh} and q_{lT} are the isothermal and thermal liquid water fluxes [m s^{-1}], respectively, K_{vh} is the isothermal hydraulic conductivity for water vapor fluxes [m s$^{-1,}$] K_{vT} is the thermal hydraulic conductivity for water vapor fluxes [m^2 s^{-1} K^{-1}], h_p is the pressure head [m], and T is the temperature [K].

The thermal (K_{vT}) water vapor hydraulic conductivity is defined as follows (Šimůnek et al, 2008):

$$K_{vT} = \frac{D}{\rho_w}\eta H_r \frac{d\rho_{sv}}{dT} \qquad 3.8$$

where D is the vapor diffusivity in soil [m^2 s^{-1}], ρ_w is the density of water [kg m^{-3}], η is the enhancement factor [-] (Cass et al., 1984), H_r is the relative humidity [-], and ρ_{sv} is the saturated vapor density [kg m^{-3}].

The relation between vapor diffusivity in soils and free air and the volumetric soil air content is described by:

$$D = \tau_{MQ}\theta_a D_a \qquad 3.9$$

where θ_a [m^3 m^{-3}] is the air filled porosity, D_a [m^2 s^{-1}] is the water vapor diffusivity at a temperature T [K] and τ_{MQ} [-] is the tortuosity as defined by Millington & Quirk (1961).

Definition of the enhancement factor and its dependence on soil water content is strongly linked to the definition of the tortuosity factor: According to Jury & Horton (2004), the tortuosity factor for vapor flow is different from the tortuosity of an inert gas because islands of water blocking diffusion through pores do not function as blockage for vapor since vapor can condense on one side of the water cluster and evaporate from the other. Usage of the Millington & Quirk (1961) model to describe the effective diffusion coefficient includes parameterization of evaporation and condensation processes on liquid islands in the enhancement factor.

Water diffusivity in soils is given as:

$$D_a = 2.12 \times 10^{-5} \left(\frac{T}{273.15} \right)^2 \qquad 3.10$$

The isothermal vapor hydraulic conductivity (K_{vh}) [m s^{-1}] is defined as:

$$K_{vh} = \frac{D}{\rho_w} \rho_{sv} H_r \frac{Mg}{RT} \qquad 3.11$$

where M is the molecular weight of water [kg mol^{-1}], g is the gravitational acceleration [m s^{-2}], and R is the universal gas constant [J mol^{-1} K^{-1}].

HYDRUS uses the enhancement factor parameterized by Cass et al. (1984), who determined thermally driven vapor diffusion enhancement η by using transient state thermal conductivity measurements. Cass et al. (1984) studied the thermal conductivity as a function of temperature, water content, and pressure. They describe the enhancement factor as follows:

$$\eta = 9.5 + \frac{3\theta}{\theta_s} - 8.5 \exp\left\{ - \left[\left(1 + \frac{2.6}{\sqrt{f_{cl}}} \right) \frac{\theta}{\theta_s} \right]^4 \right\} \qquad 3.12$$

where θ [m^3 m^{-3}] is the volumetric water content, θ_s [m^3 m^{-3}] is the saturated water content, and f_{cl} [-] is the clay mass fraction in the soil.

Three model scenarios were designed to demonstrate the effect of the enhancement factor on soil moisture/temperature and evaporation in systems liable to temperature gradients induced by external heat sources and in a system where the temperature gradient is caused by evaporation from the top of a soil column. In the first scenario, the temperature gradient in the soil decreases from bottom to top of the profile and is caused by cold air cooling the top of the soil column with simultaneous heating of the bottom of the soil column. In a second scenario, the temperature in the soil profile was inverted by cooling the bottom of the soil and simultaneously heating the top of the soil column with warm air. In a third scenario no temperature gradient exists between the bottom of the soil and the air flowing over the soil column.

Table 3.2 Van Genuchten – Mualem hydraulic parameters and meteorologic data used to for modeling. Meteorologic parameters were chosen to represent laboratory conditions. The grey shaded area shows the parameters changed in the three scenarios.

hydraulic properties	**θ_s**	**θ_r**	**α**	**n**	**K_s**	**l**
unit	[cm^3 cm^{-3}]		[cm^{-1}]	[-]	[cm d^{-1}]	[-]
	0.41	0.03	0.09	1.3	50	0.5
meteorologic parameters‡		**R_{in}**	**v_{wind}**	**H_r**	**T_{air}**	**T_{bot}**
unit		[MJ m^{-2} d^{-1}]	[km d^{-1}]	[%]	[°C]	
scenario A (heat bottom)		0.1	40	90	5	30
scenario B (heat top)		0.1	40	25	30	5
scenario C (no external heat)		0.1	40	40	20	20

‡ *R_{in}: incoming radiation; v_{wind}: wind speed; H_r: relative humidity; T_{air}: air temperature; T_{bot}: bottom temperature*

However, evaporation from the top of the soil and small radiation lead to a small gradient in temperature of the soil. By using model scenarios with temperature increasing and decreasing towards the top of the profile, the effect of thermal water vapor flux on total vapor flux and, consequently, on evaporation is illustrated. Simulation time was 50 days and all scenarios started with a fully saturated silty soil column and a homogeneous temperature profile (20°C). Constant temperature and no water flux were chosen as lower boundary conditions. As upper boundary condition an energy balance equation was solved (Section 2.2) to calculate water and heat boundary fluxes. Standard meteorological data are needed to solve the energy balance equation.

These data were chosen to represent laboratory conditions and are given in Table 3.2.. Each simulation was performed including and excluding ($\eta = 1$) the enhancement factor. I am aware that the used model setup is not in agreement with Shokri et al.'s (2009) experimental setup in every detail. Nonetheless I think that the model simulations can be used to illustrate the potential effect of the enhancement factor as defined by Philip & de Vries (1957) and questioned by Shokri et al. (2009).

In model scenario A, a temperature gradient in the soil profile is generated, where the temperature decreases towards top of the profile (Figure 3.11). Including the enhancement factor in the model simulation results in a higher cumulative evaporation and consequently a drier soil profile compared to the model simulation with excluded enhancement factor (η = 1). The distribution of vapor fluxes seen in Figure 3.11 shows that both fluxes are directed upwards (positive). This is the case for enhanced and non-enhanced approach. However, because of the thermal gradient within the soil column, upward thermal water vapor flux is higher for the enhanced approach during the simulation. This leads to a higher evaporation rate, if enhanced vapor diffusion is taken into account.

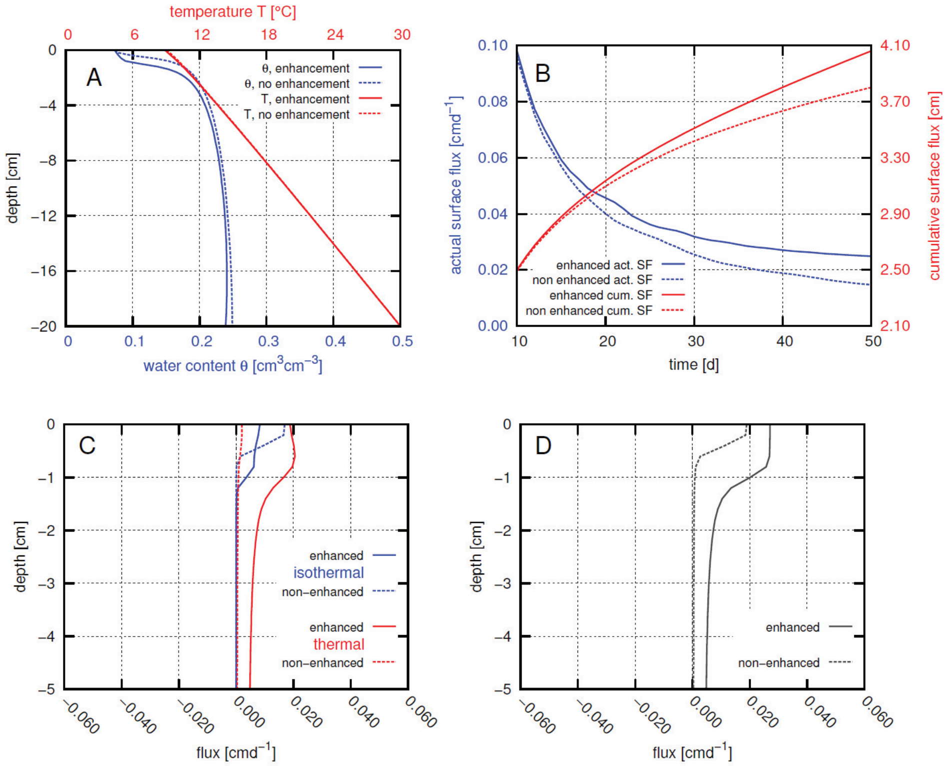

Figure 3.11: Scenario A (T_{air} = 5°C; T_{bot} = 30°C). (A) Soil water and temperature profile after 40 days of modeled evaporation with and without enhanced water vapor diffusion. (B) Calculated actual (act. SF) and cumulative surface fluxes (cum. SF) from day 10 to day 40 of the model simulation. (C) Distribution of isothermal and thermal water vapor fluxes and (D) total vapor flux at day 40 in the top 5 cm of the soil profile. Negative fluxes are directed into the soil. In all plots, solid and dashed lines show modeling approaches with and without enhancement of vapor diffusion, respectively.

In model scenario B (Figure 3.12) the temperature within the soil column increases towards the soil surface. Contrary to evaporation and soil moisture shown in Figure 3.11, including the enhancement factor results in a lower evaporation and higher water contents in the soil profile.

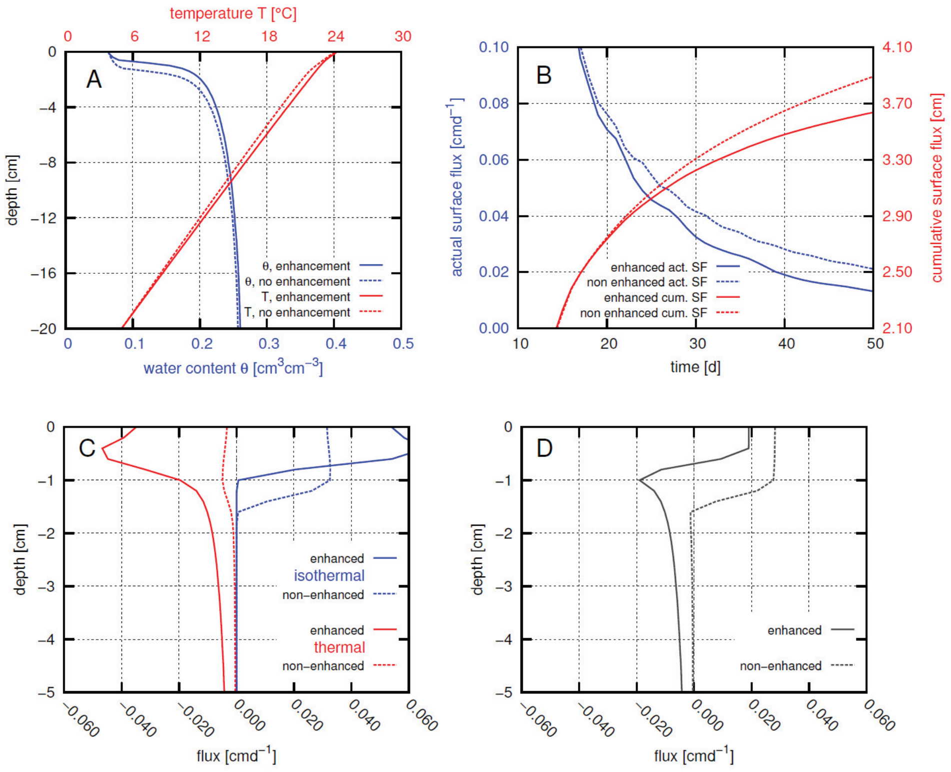

Figure 3.12: Scenario B (T_{air} = 30°C; T_{bot} = 5°C). (A) Soil water and temperature profile after 40 days of modeled evaporation with and without enhanced water vapor diffusion. (B) Calculated actual (act. SF) and cumulative surface fluxes (cum. SF) from day 10 to day 40 of the model simulation. (C) Distribution of isothermal and thermal water vapor fluxes and (D) total vapor flux at day 40 in the top 5 cm of the soil profile. Negative fluxes are directed into the soil. In all plots, solid and dashed lines show modeling approaches with and without enhancement of vapor diffusion, respectively.

Water vapor flux distribution shows that the thermal vapor flux is directed downwards into the profile, following the temperature gradient and the isothermal water vapor flux is directed upwards. The enhancement factor increases the downward thermal vapor flux and consequently, evaporation rates are lower in the enhanced approach.

In model scenario C, no temperature gradient was applied to the soil profile and the temperature gradient in the soil column is a result of the small incoming radiation and energy consumption by evaporation.

As can be seen in Figure 3.13, the enhancement factor does not have a considerable effect on the model simulations. Both, enhanced and non-enhanced approach, show similar results for soil moisture and evaporation.

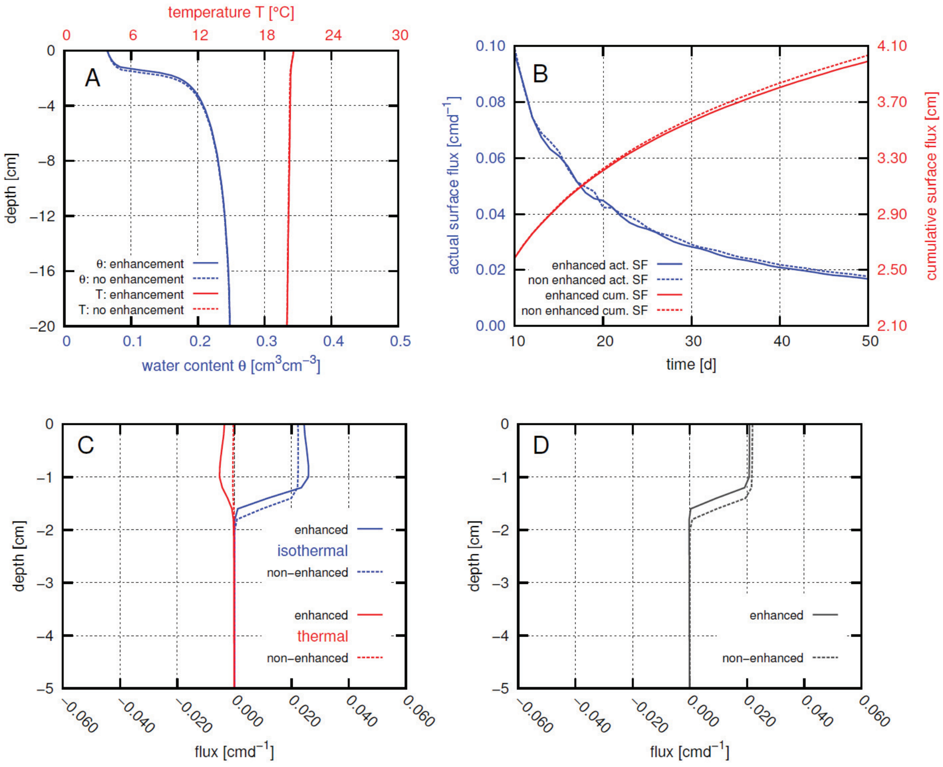

Figure 3.13: Scenario C (T_{air} = 20°C; T_{bot} = 20°C). (A) Soil water and temperature profile after 40 days of modeled evaporation with and without enhanced water vapor diffusion. (B) Calculated actual (act. SF) and cumulative surface fluxes (cum. SF) from day 10 to day 40 of the model simulation. (C) Distribution of isothermal and thermal water vapor fluxes and (D) total vapor flux at day 40 in the top 5 cm of the soil profile. Negative fluxes are directed into the soil. In all plots, solid and dashed lines show modeling approaches with and without enhancement of vapor diffusion, respectively.

Even though an effect of the enhancement factor on thermal water vapor flux can be seen, it remains a minor flux component, because the thermal gradient within the system is very small. This results in similar total water vapor fluxes in enhanced and non-enhanced approach.

Therefore, experiments without strong temperature gradients are dominated by isothermal flow (in liquid and vapor phase). However, the enhancement factor itself has been defined to predict water vapor movement under temperature gradients. Temperature gradients caused by evaporation from soil columns in which no external energy source such as radiation or an externally applied temperature gradient are applied, do not lead to sufficiently large temperature gradients which induce an important thermal water flux that is affected by the enhancement factor.

Even though these numerical results are not supported by experimental data, I think that the simulations illustrate the influence of the enhancement factor as defined by Philip & de Vries (1957) under different boundary conditions. Our study supports the conclusions of Shokri et al. (2009) that an enhancement factor was not needed to explain the evaporation rates observed in their laboratory experiment. Additionally, our simulation results demonstrate that an enhancement of thermal water vapor diffusion is not important for evaporation from soil columns in a laboratory setup without an additionally enforced temperature gradient, for instance generated by radiation. The presented results do not (and cannot) resolve the question whether the theory of capillary flow or enhanced water vapor diffusion is more plausible. I merely think that the experiments performed by Shokri et al. (2009) should include setups subject to a temperature gradient to clarify whether or not an enhancement factor is needed to explain differences in theory and measurements of water vapor fluxes.

4 Estimation of hydraulic parameters using IR and TDR measurements

[Please note that Chapter 4 is based on research written up in form of the peer-reviewed paper: **Steenpass C., J. Vanderborght, M. Herbst, J. Šimůnek and H. Vereecken (2010). Estimating Soil Hydraulic Properties from Infrared Measurements of Soil Surface Temperatures and TDR Data. Vadose Zone J. 9: 910 – 924.**]

4.1 Introduction

The dynamics of soil water content at the soil surface provides important insights into physical processes governing the soils' interactions with the atmosphere. These interactions are important in a variety of models that predict soil water and energy balances and plant growth (Vereecken et al., 2008). Soil hydraulic properties are important controlling factors for water and energy exchange between the soil and the atmosphere and are required to properly simulate these processes.

Classical methods usually identify soil hydraulic properties representative for small soil volumes (Dane & Topp, 2002). However, such measurements are costly and time-consuming and need to be repeated for a large number of soil cores and locations since soil hydraulic properties vary considerably in space. This variation is caused not only by spatial heterogeneities within the soil structure, but also by soil compaction or soil tillage (Mapa et al., 1986; Murphy et al., 1993; Osunbitan et al. 2005). On the other hand, remote sensing techniques provide an opportunity to observe the state of the soil surface for relatively large areas and may thus be used to derive effective soil hydraulic properties at a much larger scale (Burke et al., 1997; Chanzy et al., 1995; Demarty et al., 2005; Das & Mohanty, 2006), Camillo et al (1986) and Burke et al. (1998) used ground-based passive microwave data to inversely estimate soil hydraulic properties. They concluded that hydraulic properties may be inferred from ground-based remotely sensed data if the dataset covers a broad range of water contents, from dry to wet. Additionally, Camillo et al. (1986) and Burke et al. (1997, 1998) concluded that a short period of intensive measurements (Camillo et al., (1986) used 3 days, Burke et al., (1998) used 15 days) was sufficient to derive hydraulic properties.

Several methods allow the inversion of field measured or remotely sensed data. Optimization algorithms, such as the Shuffled-Complex-Evolution developed at the University of Arizona (SCE-UA, Duan et al., 1992), are designed to find the global minimum of the objective function in a space of optimized parameters reliably. However, since measurements are generally error-prone, the “best” parameter set corresponding to the global minimum is uncertain, which may lead to a considerable uncertainty in the model outputs (Vrugt et al., 2003).

In previous studies, either observed soil surface temperatures were used to infer evapotranspiration rates (Ben-Asher et al., 1983; Olioso et al., 1996; Olioso et al., 1999) or measured evaporation fluxes were used to estimate soil hydraulic properties (Jhorar et al., 2002). Additionally, soil surface temperatures strongly depend on the water content in the top few centimeters of the soil. This means that soil surface temperatures may be used to directly infer soil hydraulic properties (Demarty et al., 2005).

In order to estimate soil hydraulic properties from measured surface temperatures, it is important that water and energy fluxes, as well as their mutual interactions, are adequately modeled. Philip & de Vries (1957) pointed out that the movement of water vapor in the soil depends on both thermal and hydraulic gradients. The influence of water vapor in the soil on soil water dynamics has been studied in numerous publications (e.g., Rose, 1968a; Rose, 1968b; Jackson et al., 1973a; Jackson et al., 1973b; Cahill & Parlange, 1998; Scanlon et al., 2003; Goss & Madlinger, 2007; Shokri et al., 2008). The general agreement in these studies is that water vapor fluxes become more important for the total soil water dynamics as the soil dries out. Milly (1982), Kondo et al. (1990), Scanlon & Milly (1994), Saito et al. (2006), and Bitelli et al. (2008), among others, therefore included water vapor flow in their models to obtain improved predictions of temperatures, water dynamics and evaporation rates.

This section presents a modeling approach for the inverse estimation of van Genuchten - Mualem parameters of soil hydraulic properties (van Genuchten, 1980) from relatively short periods (following Camillo et al.; 1986, Burke et al., 1998) of ground-based remotely sensed infra-red based measurements of soil surface temperatures. For that purpose, the optimization algorithm was linked to a hydrologic model that considers coupled movement of water and energy (Saito et al., 2006). The use of a recently developed optimization algorithm (Vrugt et al., 2008a) allows to determine the information content of soil surface temperatures for estimation of soil hydraulic parameters. In addition, it was tested whether combining local water content measurements with soil surface temperatures will improve estimates of soil hydraulic properties. As subsurface hydraulic properties, and the corresponding soil water dynamics, are important for the water availability and the heat transport close to the soil surface, time domain reflectometry (TDR) measurements in 7-cm and 15-cm depths were made. The general applicability of the approach was first tested using numerically generated data. The same approach was then also applied to a real dataset. This study was conducted (i) to analyze the information content of soil surface temperatures for estimation of soil hydraulic properties with short measurement periods, (ii) to characterize uncertainties in SHP estimated from SST and soil water content data, and (iii) to determine the effect of soil tillage on near-surface soil hydraulic properties.

4.2 Materials and methods

For forward modeling the version 3.0 of the well-tested hydrological model HYDRUS-1D (Šimůnek et al., 2005; Šimůnek et al., 2008) was used. HYDRUS-1D numerically solves the Richards equation for variably-saturated water flow and convection-dispersion type equations for heat transport. The governing equations for water flow and heat transport are solved numerically using Galerkin-type linear finite element schemes.

For inverse estimation of soil hydraulic properties, soil surface temperatures have to be modeled as accurately as possible. Various studies (e.g., de Vries, 1975; Milly, 1984; Cahill & Parlange, 1998; Saito et al., 2006) pointed out that soil temperature calculations can be erroneous, if thermal and isothermal water vapor fluxes are neglected. Especially in the upper part of the soil profile, which dries out very fast, water vapor plays an important role in the total water movement (Cahill & Parlange, 1998). Following the approach of Saito et al. (2006), a modified HYDRUS-1D v 3.0 is used, which accounts for water vapor flow and the effects of temperature gradients (Section 2.1) on water flow and uses an energy balance equation as upper boundary condition for the coupled heat and water flow equations (Section 2.2). Similar approaches were developed by Camillo et al. (1983), Camillo & Gurney (1986), Nassar & Horton (1989, 1992), and Milly (1982, 1984).

4.2.1 Model description

Only equations considered important for a better conclusiveness of Chapter 4 will be given in this section. A more detailed description of the used model can be found in Chapter 2.

One-dimensional liquid water and water vapor movement

Following Saito et al. (2006) one-dimensional liquid water q_l [m s^{-1}] and water vapor q_v [m s^{-1}] fluxes (expressed in terms of equivalent volumes of liquid water) in soils can be described as

$$q_l = q_{lh} + q_{lT} = -K_{lh}\left(\frac{\partial h}{\partial z} + 1\right) - K_{lT}\frac{\partial T}{\partial z} \qquad 4.1$$

and

$$q_v = q_{vh} + q_{vT} = -K_{vh}\frac{\partial h}{\partial z} - K_{vT}\frac{\partial T}{\partial z} \qquad 4.2$$

where K_{lh} and K_{vh} are the isothermal hydraulic conductivities for liquid water and water vapor fluxes [m s^{-1}], respectively, K_{lT} and K_{vT} are the thermal hydraulic conductivities for liquid water and water vapor fluxes [m^2 s^{-1} K^{-1}], respectively, q_{lh} and q_{lT} are the isothermal and thermal liquid water fluxes [m s^{-1}], respectively, q_{vh} and q_{vT} are the isothermal and thermal water vapor fluxes [m s^{-1}], respectively, h is the pressure head [m] and z [m] is the vertical coordinate, and T [K] is the temperature.

Inserting the liquid water and water vapor fluxes into a mass conservation equation yields the governing equation for one-dimensional water flow in variably saturated porous media, which describes the change in the total water content over time (Saito et al., 2006).

$$\frac{\partial \theta}{\partial t} = \frac{\partial}{\partial z}\left[K_{lh}\frac{\partial h}{\partial z} + K_{lh}(h) + K_{lT}\frac{\partial T}{\partial z} + K_{vh}\frac{\partial h}{\partial z} + K_{vT}\frac{\partial T}{\partial z}\right] \qquad 4.3$$

where θ is the total volumetric water content, consisting of the sum of the volumetric liquid water content θ_l and the water vapor content θ_v ($\theta = \theta_l + \theta_v$) (both expressed as a volume of liquid water per volume of bulk soil [m^3 m^{-3}]) and t [s] is time.

Heat transport

Based on the mathematical model of Philip & de Vries (1957) and Philip (1957), the soil heat flux is described using the following equation:

$$q_h = -\lambda(\theta_l)\frac{\partial T}{\partial z} + C_w T q_l + C_v T q_v + L_0 q_v \qquad 4.4$$

where q_h [J m^{-2} s^{-1}] is the total heat flux, $\lambda(\theta_l)$ [J m^{-1} s^{-1} K^{-1}] is the apparent thermal conductivity, which is a function of the volumetric water content θ_l, T is the temperature [K], C_w and C_v [J m^{-3} K^{-1}] are the volumetric heat capacities for water and vapor, respectively, q_l [m s^{-1}] is the liquid water flux, q_v [m s^{-1}] is the water vapor flux, which is expressed as an equivalent volume flux of liquid water [m s^{-1}], and L_0 [J m^{-3}] is the volumetric latent heat of vaporization of liquid water (Saito et al., 2006)

Combining the heat flux and the energy conservation equation yields the governing equation for heat flow, describing the change in heat storage over time.

$$\frac{\partial C_p T}{\partial t} + L_0 \frac{\partial \theta_v}{\partial t} = \frac{\partial}{\partial z}\left[\lambda(\theta_l)\frac{\partial T}{\partial z}\right] - C_w \frac{\partial q_l T}{\partial z} - L_0 \frac{\partial q_v}{\partial z} - C_v \frac{\partial q_v T}{\partial z} \qquad 4.5$$

where C_p [J m^{-3} K^{-1}] is the heat capacity of the soil consisting of the volumetric heat capacities of the liquid water, water vapor, and the solid phase (Saito et al., 2006).

4.2.2 Field measurements

Field data was collected from 15th to 26th of September 2008 on a bare soil at the Selhausen field test site, near the Research Center Jülich, Germany. The soil at the experimental test site was kept bare since September 2006 and was regularly treated with herbicides to prevent accumulation of weeds.

According to the USDA the soil was classified as a silt loam (sand 13%, silt 70%, clay 17%, Herbst et al., 2009). Bauer et al. (2008) measured an organic matter content of 2.2 – 2.5 volume percent for the upper 20 cm of the soil. From the site, small undisturbed soil cores (100 cm³) were sampled. Water retention curves of the samples were determined in the laboratory, using sand suction tables and pressure cells. Saturated hydraulic conductivity was derived using a constant head permeameter. The soil hydraulic parameters, i.e. the Mualem van Genuchten parameters and the saturated conductivity that were derived from the lab measurements are given in Table 4.1.

72 TDR probes (two-rod TDR probes, 25 cm rod length, 2.3 cm spacing between the rods, 11.5 m coaxial cable length) were installed at 36 locations in a field plot of 36 m^2 (6 m x 6 m), which was harrowed before the installation of the TDR probes. Bulk density (BD) for the harrowed upper part of the soil (0 – 10 cm) was 1.35 g cm^{-3} and 1.69 g cm^{-3} for the lower (10 – 90 cm), non-tilled part of the soil. Note that the bulk density of the harrowed top layer was considerably smaller than the bulk density of the soil samples that were taken from the top soil layer of a non-disturbed field plot and from which soil hydraulic parameters were derived in the lab (Table 4.1).

To install the TDR probes 3 trenches with 6 small pits at each side of the three trenches were excavated. One week before the start of the experiment, two TDR probes were installed horizontally at the depths of 7 cm and 15 cm in each of the 36 pits (Figure 4.1). As the coaxial TDR cables might disturb the IR surface temperature measurements, the trenches were used in order to bury the cables (at 10 cm depths) to the TDR instruments outside the test plot. Before installation, all TDR probes were calibrated with water-air measurements. Installed TDR probes were connected to a TDR 100 cable tester and the recorded waveforms were stored on a CR1000 data logger (both Campbell Scientific, Logan, UT, USA). The PCTDR software (Campbell Scientific, Logan, UT, USA) was used to analyze the waveforms for the dielectrical permittivity and the empirical relationship of Topp et al. (1980) to convert the dielectrical permittivity to water content. The soil water content was monitored on a half-hourly basis.

Figure 4.1: TDR probe installation for the field experiment from 15th to 26th of September 2008.

Additionally, at each location soil temperatures at 3-cm and 6-cm depths were measured manually every 6 hours with a TypeE thermocouple (Li 8100-201, LI-COR Biosciences, Lincoln, NE, USA).

Table 4.1 Soil hydraulic parameters for the upper (0-10 cm) and lower part (10-90 cm) of the soil profile as determined in the laboratory using the sand suction table and the pressure cell method. 100-cm^3 soil samples were taken before the harrowing of the plot in an undisturbed part of the soil profile. The saturated hydraulic conductivity was determined using the constant head method.

Measurement Data	θ_r [cm^3 cm^{-3}]	θ_s [cm^3 cm^{-3}]	α [cm^{-1}]	n [-]	K_s [cm d^{-1}]	BD† [g cm^{-3}]
0 – 10 cm	0.0000	0.3530	0.0042	1.3242	91.6800	1.6140
10 – 90 cm	0.0000	0.3719	0.0690	1.2525	50.8800	1.6920

† BD = Bulk Density

An infra-red (IR) camera (VarioCAM, InfraTec, Germany) was installed to measure the soil surface temperature every 5 minutes. The IR camera measures the brightness temperature in the spectral range from 8 to 14 µm. It has a resolution of 320 x 240 pixels and an absolute measurement accuracy of ±1.5 K in the temperature range from -10 – 50 °C. The IR camera was installed on an auto hoist 11-m above ground to cover the 6 m x 6 m measurement plot (Figure 4.2). Within the spectral range from 8 to 14 µm and a measurement distance of ~11 m, the transmittance of air can be neglected (Gaussorgues & Chomet, 1994)($\tau_D = 1$ in Eq. 2.50).

For soils, an emissivity from 0.8 to 0.98 [-] is given by Allen et al. (1998). Within HYDRUS-1D moisture dependency of emissivity ε is defined by

$$\varepsilon = \min(0.9 + 0.18 \cdot \theta, \quad 1) \qquad 4.6$$

During the field experiment, the sky was partially covered with clouds, which can be seen in the net radiation data shown in Figure 4.3. Air temperature, relative humidity (combined temperature/air humidity sensor CS215, Campbell, Logan, NE, USA), wind speed (CSAT3, Campbell, Logan, NE, USA) and net radiation (1 x SP Lite, Kipp & Zonen, Delft, The Netherlands) were monitored by an automatic weather station installed close to the test site. All meteorologic data was measured 2 m above the ground. Figure

4.3 shows the meteorological standard data for the duration of the experiment. Half-hourly values of the meteorological data were used as input data for the model.

Figure 4.2: IR camera installed on an auto hoist 11 m above ground. The camera was used to measure the soil surface temperature of the experimental plot every 5 minutes during field experiment.

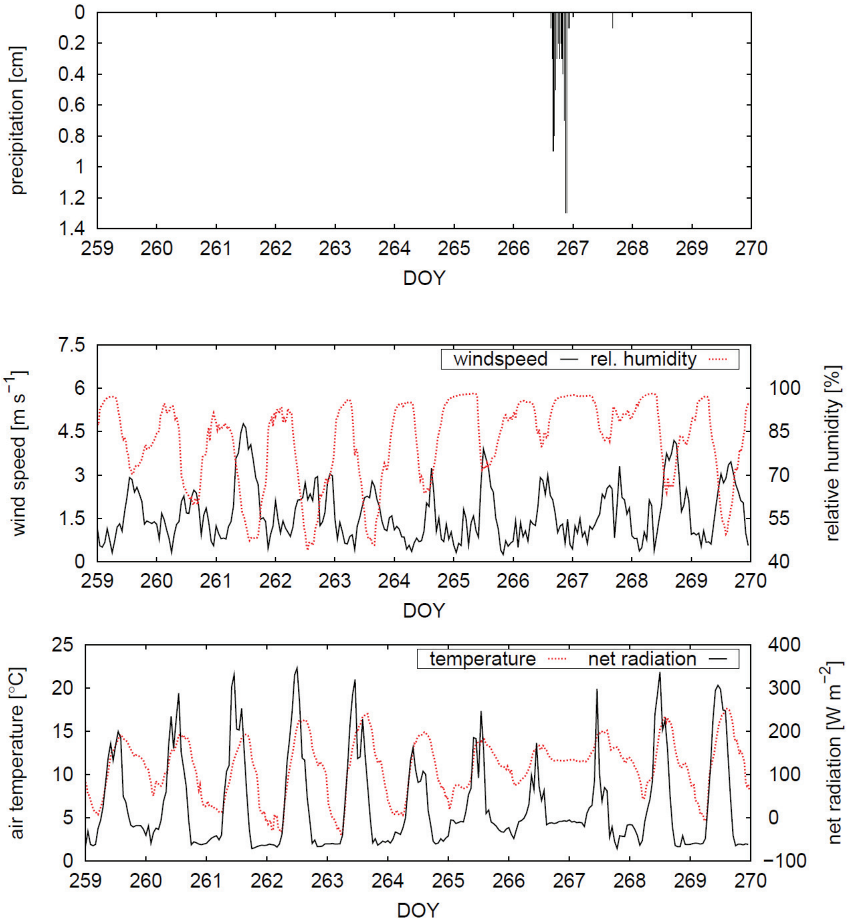

Figure 4.3: Meteorological data measured at the Selhausen test site during the field experiment in September 2008 (15th to 26th). The upper plot shows the irrigation events, the middle plot the wind speed (solid black line) and the relative humidity (dotted red line), and the lower plot the air temperature (dotted red line) and the net radiation (solid black line).

4.2.3 Parameterization and inverse optimization

A 90-cm soil profile was discretized for numerical simulations into 100 finite elements and 101 nodes. Zero pressure head and temperature gradients (i.e., free drainage) were used as bottom boundary conditions for water flow and heat transport, respectively. The energy balance and the soil surface boundary condition were described in a previous paragraph. Since pressure head and temperature gradients increases towards the top of the soil profile, the spatial discretization was gradually refined towards the soil surface where the grid size was 0.3 cm. Chung & Horton (1987) parameters of a loamy soil (b_1 = 0.243, b_2 = 0.393, b_3 = 1.534, all [W m^{-1} K^{-1}]) implemented in HYDRUS-1D were used to describe the thermal properties of the soil at the test site. The thermal dispersivity β has not been measured often for unsaturated soils, since it only becomes important when water flux is high (Hopmans et al., 2002). A value of $\beta=5$ [cm] was taken, which is the default value used in HYDRUS-1D. Initial conditions for numerical simulations were derived from TDR water content measurements at 7, 15, 45, 60, and 90 cm depths and temperature measurements at 3, 6, 15, 45, 60, and 90 depths at the beginning of the experiment. Water contents at 45, 60, and 90 cm depths and temperatures at 15, 45, 60, and 90 cm depths were measured few meters apart from the experimental plot with horizontally installed TDR and temperature probes. These measurements were only used to define the initial conditions as good as possible but were not further used in the optimization process. Water content measurements in 7 and 15 cm depth were used for inversion.

The DREAM (Differential Evolution Adaptive Metropolis) algorithm (Vrugt et al., 2008a, b) was used to estimate the van Genuchten-Mualem soil hydraulic parameters from measured soil surface temperatures and water contents and to determine their posterior probability distribution given the observed dataset. The algorithm starts with an initial population of points within the possible parameter space (the a priori parameter distribution) which is sampled by the Latin hypercube method to effectively represent the parameter space with a low number of sampling points. The a-priori distribution was assumed to be a uniform distribution with ranges of the hydraulic soil parameters that cover most soil types (see Table 4.2).

The DREAM algorithm runs multiple Markov chains in parallel for different starting points and every chain (a parent) generates new candidate points (proposals) for every single model evaluation. Whether or not new candidate parameter sets are accepted is based on the log-likelihood of the parameter set given the measured data. By updating the parameter sets in the chains based on their log-likelihood, the distribution of the parameter sets converges to the posterior distribution given the measured dataset.

Table 4.2 The reference set of the van Genuchten-Mualem soil hydraulic parameters used to generate measurements for the synthetic experiment and the optimized values obtained using single-objective (SO) and multi-objective (MO) approaches. Numbers in parenthesis are the lower and upper bands of the 95% confidence interval. The parameter range gives the upper and lower limits allowed for each parameter during the optimization.

Measurement Data	**θ_r [cm^3 cm^{-3}]**	**θ_s [cm^3 cm^{-3}]**	**α [cm^{-1}]**	**n [-]**	**K_s [cm d^{-1}]**
Reference Parameter	0.0900	0.4000	0.0900	1.9000	10.0000
Soil Surface Temperature (SO)	0.0910 (0.0371 – 0.1051)	0.3838 (0.2905 – 0.4438)	0.1015 (0.0500 – 0.1908)	1.7069 (1.3283 – 1.9771)	8.688 (1.3489 – 42.4521)
Soil Surface Temperature + Water Content (MO)	0.0860 (0.0582 – 0.0976)	0.4014 (0.3258 – 0.4466)	0.1063 (0.0689 – 0.1764)	1.8375 (1.5345 - 1.9882)	11.6054 (2.4394 – 28.7872)
Parameter Range	0.000 – 0.150	0.250 – 0.450	0.003 – 0.200	1.100 – 2.000	1.00 – 500.00

The posterior distributions of soil hydraulic parameters are derived for two different datasets. The first dataset contains only soil surface temperature (SST) measurements, which were spatially averaged in the field plot. For this single objective (SO) approach, the log-likelihood function l_{SST} is defined as:

$$l_{SST}\left(\Theta \middle| \hat{Y}_{SST},\zeta,\phi\right) = -\frac{N}{2} * \left(\ln\left(2\pi\right)+\ln\left(\sigma_{SST}\right)\right) - 0.5 * \sum_{i=1}^{N} \frac{\left(y_{i,SST}\left(\Theta|\zeta,\phi\right)-\hat{y}_{i,SST}\right)^2}{\sigma_{SST}{}^2} \qquad 4.7$$

where Θ is a vector of model parameters (van Genuchten-Mualem parameters in this case), ζ and ϕ are measured initial and boundary conditions, respectively, $\hat{\boldsymbol{Y}}_{SST}$ is a vector of the observed system behavior (in this case the SST measurements), N denotes the number of SST measurements, $y_{i,SST}$ and $\hat{y}_{i,SST}$ are the i^{th} SST measurement value and the SST model prediction, respectively, and σ_{SST} is the standard deviation of residuals between the measured and simulated soil surface temperatures for the optimal parameter set, i.e., for the parameter set with the highest likelihood. The optimal parameter set or the parameter set with the highest log-likelihood do not depend on σ_{SST}. However, σ_{SST} determines the spreading of the posterior parameter distribution. Therefore, a two-step approach was used to determine the posterior parameter distribution. In the first step, the optimal parameter set was determined using a dummy value of σ_{SST}. For the optimal parameter set, σ_{SST} was calculated from the residuals between the modeled and measured surface temperatures (σ_{SST} = 1.95 °C). This value was subsequently used to derive the posterior parameter distribution. It must be noted that σ_{SST} comprises both measurement and model errors.

The second dataset contained soil surface temperature and water content measurements at 7 and 15 cm depths, expressed as the mean of the 7-cm and 15-cm depth TDR measurements. A multi-objective optimization (MO) was used in this case with one objective function defined using surface temperatures and the other two using water contents at different depths. The log-likelihood was calculated for water contents measured at different depths *j = 7, 15* cm as follows:

$$l_{WC_j}\left(\Theta \middle| \hat{Y}_{WC_j},\zeta,\phi\right) = -\frac{N}{2} * \left(\ln\left(2\pi\right) + \ln\left(\sigma_{WC_j}\right)\right) - 0.5 * \sum_{i=1}^{N} \frac{\left(y_{i,WC_j}\left(\Theta \middle| \zeta,\phi\right) - \hat{y}_{i,WC_j}\right)^2}{\sigma_{WC_j}{}^2} \qquad 4.8$$

where σ_{WCj} are the standard deviations of residuals between the measured and simulated water contents at a depth of *j* = 7 and *j* = 15 cm, which have been calculated with the same approach as described for σ_{SST}. Again, values of σ_{WCj} (0.005 cm^3 cm^{-3} at a depth of 7 cm) and σ_{WCj} (0.006 cm^3 cm^{-3} at a depth of 15 cm) comprise both measurement and model errors.

The total log likelihood was obtained as:

$$l_{total} = l_{SST} + l_{WC7} + l_{WC15} \qquad 4.9$$

Based on the calculated likelihood of every parameter set, the Markov chain either moves to a new location when the likelihood is higher, or remains at the old position when the likelihood is lower. Additionally, a random change in the chain's position can occur:

$$\alpha_M = \min\left[e^{(l_{new} - l_{old})}, 1\right] \qquad 4.10$$

where α_M is the Metropolis acceptance probability, and l_{new} and l_{old} represent the likelihoods of the proposal and the parent position of the Markov chain, respectively. Equation 4.10 shows that a higher likelihood in the proposal position (l_{new}) compared to the parent position (l_{old}) results in α = 1, forcing the Markov chain to move to the proposal position. For $\alpha < 1$, a random number r is drawn from a uniform distribution between 0 and 1 and the chain moves to the proposal position, if $r < \alpha$. This Random Walk Metropolis method makes the DREAM optimization algorithm an efficient and robust sampler of the parameter space. For inverse modeling, a total of 50,000 model evaluations distributed on 5 CPUs was used. This set-up resulted in approximately two days computation time for an optimization run.

In order to test the ability of the DREAM algorithm to infer the van Genuchten-Mualem soil hydraulic parameters from soil surface temperature data, a synthetic experiment was performed first: A HYDRUS-1D forward simulation with known van Genuchten-Mualem parameters (Table 4.2), subsequently referred to as the reference parameters, was first carried out to generate synthetic soil surface temperatures and water contents in two different depths. The synthetic dataset was generated using the same initial and boundary conditions, the same meteorological conditions and the same flow domain as for the real Selhausen dataset. A random error with known standard deviation (σ_{SST} =0.75°C, σ_{WC7} = 0.005 cm^3 cm^{-3}, σ_{WC15} = 0.005 cm^3 cm^{-3}) was added to simulated data, which were then used as a synthetic measurement dataset for the inverse optimization of the van Genuchten-Mualem parameters of soil hydraulic properties.

4.3 Results and discussion

4.3.1 Synthetic data experiment

In Figure 4.4 posterior probability density functions (pdfs) of the parameters obtained using the SO and the MO approaches are shown. The horizontal axes of the plots correspond with the initial parameter distribution. The width of the posterior pdf compared with the width of the a priori parameter distribution is a measure for how strong the posterior parameter distribution is constraint by the measurements.

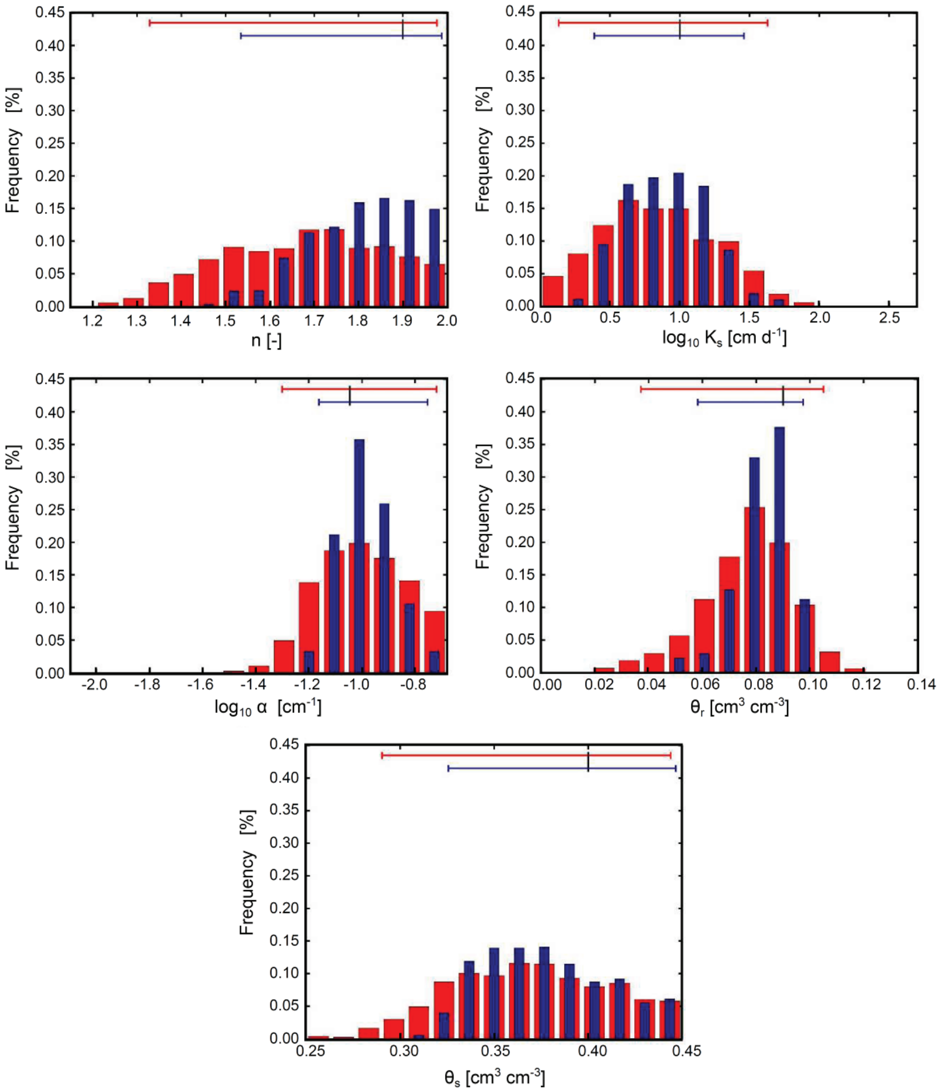

Figure 4.4: Probability density functions (pdfs) of the optimized van Genuchten-Mualem parameters for the synthetic experiment. Red (wide bars) histograms show the pdfs resulting from single objective (SO) optimization (soil surface temperature data only), blue (narrow bars) histograms show the pdfs for a multi-objective (MO) optimization (soil surface temperature and water content data). In the upper part of every plot, the 95% confidence intervals are given for the SO (upper line) and MO (lower line) approaches. Vertical black lines indicate the true parameter values.

The true and optimized parameter sets are given in Table 4.2 together with the

95th confidence intervals (CI95). The width of the posterior distributions or the CI95 compared with the width of the prior distributions (Figure 4.4, Table 4.2), show a relatively good identifiability for parameters θ_r and K_s. In relation to the initial a priori parameter ranges, confidence intervals for parameters n, θ_s, and α are larger.

Table 4.2 shows that both optimizations based on measurements of only soil surface temperatures (SO) or on measurements of soil surface temperatures and subsurface water contents (MO) produced parameter sets close to the reference parameters. The univariate posterior distributions of the optimized parameters do not contain information about correlations between parameters or clustering of parameter combinations in the parameter space. Instead of investigating the parameter uncertainty, the uncertainty intervals can also be plotted directly around the hydraulic functions. In Figure 4.5, the optimized water retention curves (obtained for the optimized parameters) are shown together with the 95% confidence range of water contents for given pressure heads.

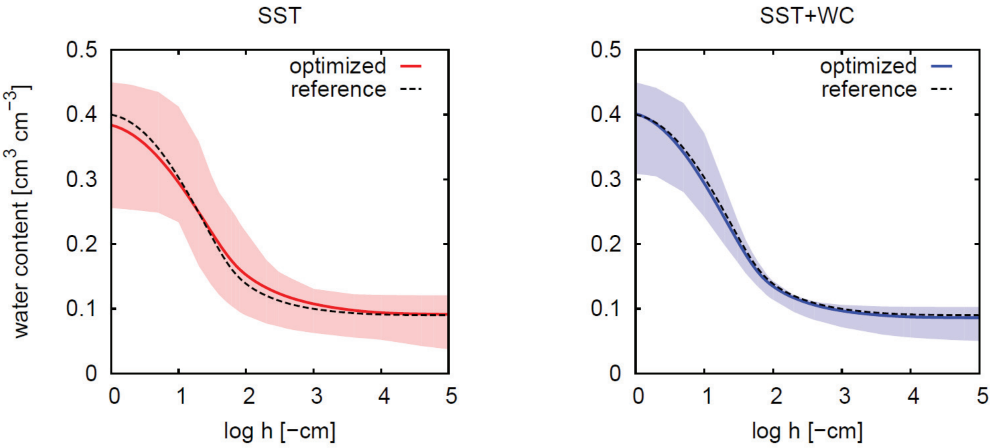

Figure 4.5: Soil water retention curves for the synthetic experiment. The dashed black line represents the reference soil water retention curve. The red line (left plot) is the optimized water retention curve based on only soil surface temperature measurements (SST) and the blue line (right plot) is the optimized water retention curve based on soil surface temperature and water content measurements (SST+WC). The shaded areas represent the 95% confidence intervals of the water contents.

A visual comparison of optimized soil water retention curves obtained with SO and MO approaches (Figure 4.5) illustrates that the use of additional water content measurements yielded slightly better results. The main difference between the two approaches is the uncertainty in the optimized retention curves, which is clearly larger for the SO than for the MO approach, especially for lower pressure heads. E.g., at h= -1000 cm, the 95% uncertainty interval of the water content θ ranges from 0.063 [cm^3 cm^{-3}] to 0.131 [cm^3 cm^{-3}] for the SO approach, and is somewhat narrower, i.e. from 0.072 [cm^3 cm^{-3}] to 0.106 [cm^3 cm^{-3}] for the MO approach.

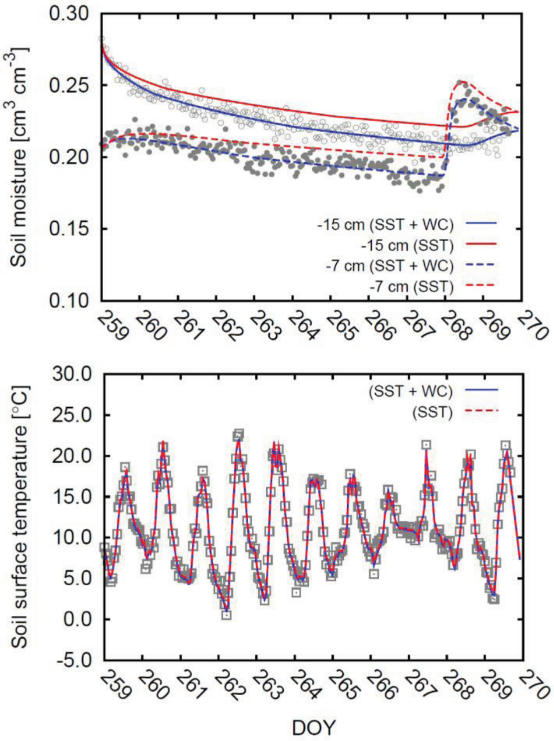

Figure 4.6: Soil water contents (left plot) and soil surface temperatures (right plot) calculated using the van Genuchten-Mualem parameters estimated using the SO approach (SST data, red lines) and the MO approach (SST+WC data, blue lines). Solid and open circles show synthetic water contents at 7-cm and 15-cm depths (left figure), respectively, and squares denote synthetic soil surface temperatures (right figure).

The optimization results of the van Genuchten-Mualem parameters were then used in the HYDRUS-1D forward simulation to compare modeled soil water contents and soil surface temperatures with those generated using the reference parameter set. Figure 4.6 shows a comparison between generated (using the reference parameter set) and modeled (using optimized parameters) soil surface temperatures and water contents.

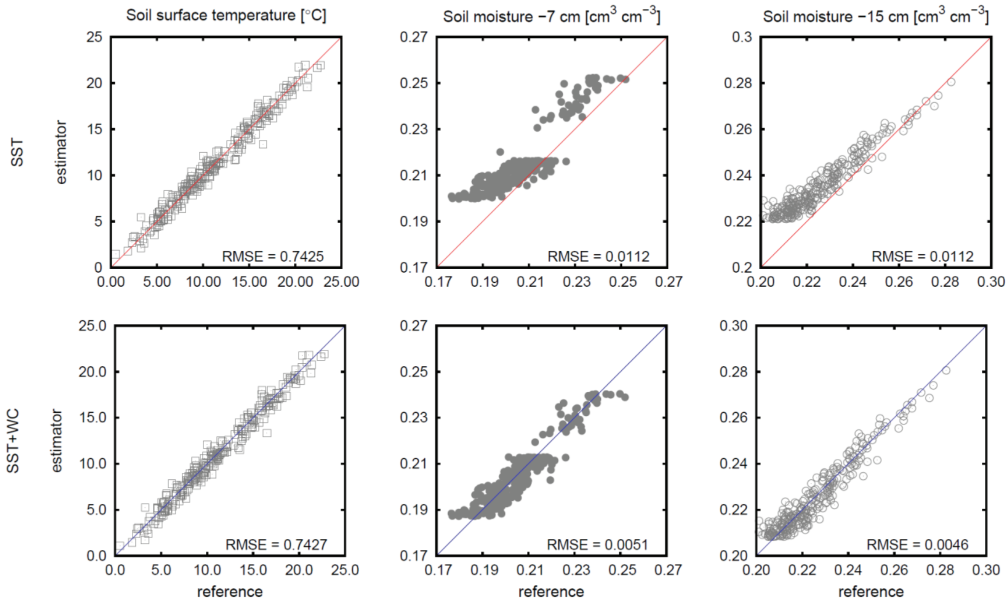

Figure 4.7: Modeled temperatures and water contents (y-axis) plotted against the synthetic measurements (x-axis). The results for parameters estimated inversely using the SO approach (from soil surface temperatures, SST) are shown in the top row. The results for parameters estimated inversely using the MO approach (from soil surface temperatures combined with subsurface soil water contents, SST+WC) are shown in the bottom row.

Both MO and SO approaches provide a similar fit of soil surface temperatures with only marginal differences. The obtained root mean squared error (RMSE), 0.7425 °C for SO and 0.7427 °C for MO are close to the random error that was added to the forward simulated temperatures. Differences in the soil water dynamics are much more significant. Figure 4.7 shows that the MO approach using measurements of both soil surface temperatures and water contents yields a better fit of measured values in both depths (RMSE 7-cm: 0.0051 cm^3 cm^{-3}, RMSE 15-cm: 0.0046 cm^3 cm^{-3}, which is close to the random error that was added to the forward simulations).

Parameters estimated from only soil surface temperature data resulted in an overestimation of soil water contents in both depths. This bias led to a larger RMSE (RMSE ~ 0.01 cm^3 cm^{-3}) for SO approach (Figure 4.7) than the random error (0.005 cm^3 cm^{-3}). However, the prediction of the soil water dynamics with the optimized parameters from soil surface temperature measurements is still reasonable (Figure 4.6).

The synthetic experiment was designed to illustrate the usefulness of soil surface temperatures to derive parameters of soil hydraulic properties. The results show that soil surface temperatures contain information that can be used to derive parameters of soil hydraulic properties. Even though uncertainties in optimized parameters become smaller when water content data are used in addition to soil surface temperatures, the reference parameter set used to generate the synthetic measurement data was reproduced reasonably well using both the SO and the MO approach.

4.3.2 Field data experiment

The measured field data were used to parameterize a model accounting for a soil profile with vertically uniform hydraulic properties. This assumption implies that an effective parameter set can be found representing a vertically heterogeneous soil profile and predicting soil surface temperatures and soil water contents at different depths adequately. The soil hydraulic parameters were optimized using the DREAM algorithm and, analogous to the synthetic experiment, both SO and MO approaches. A priori parameter ranges during the optimization process are given in Table 4.4 and final optimized values are shown in Table 4.3.

Figure 4.8 reveals that the two estimated parameter sets (using either SO or MO approaches) cannot describe soil water content dynamics properly. This is similar to findings of Yang et al. (2005), who showed that effective soil hydraulic properties cannot represent well layered soils. Yang et al. (2005) pointed out that soil hydraulic parameters cannot be adjusted in a way that a layered, heterogeneous soil profile can be approximated assuming a homogeneous soil profile. As the estimation of effective van Genuchten-Mualem hydraulic properties for a homogeneous soil profile does not yield sensible results, parameter uncertainties have not been analyzed.

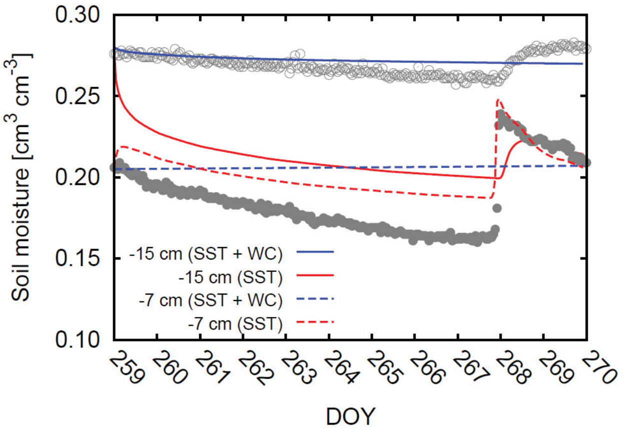

Figure 4.8: Soil water content measurements in 15 (circles) and 7 cm depth (filled dots) and predictions (lines) assuming homogeneous soil profile that was parameterized using only soil surface temperature measurements (SST) and using a combination of soil surface temperatures and soil water content measurements (SST+WC).

Table 4.3 Van Genuchten-Mualem parameter sets of an assumed homogeneous soil profile that are estimated from measured data using a single-objective (SO) and multi-objective (MO) approach.

Measurement Data	**θ_r [cm^3 cm^{-3}]**	**θ_s [cm^3 cm^{-3}]**	**α [cm^{-1}]**	**n [-]**	**K_s [cm d^{-1}]**
Soil Surface Temperature (SO)	0.0904	0.3059	0.1310	1.3061	54.9872
Soil Surface Temperature + *Water Content (MO)*	0.1381	0.3313	0.1965	1.1962	2.8787

Before the installation of the TDR probes, the plot was harrowed. As a consequence, the bulk density of the top soil layer (1.35 g cm^{-3}) was considerably lower than that of the subsoil (1.69 g cm^{-3}), indicating that different soil hydraulic properties would have to be assigned to the two layers. Therefore the soil profile was sub-divided into a layer representing the harrowed upper part of the soil (0 – 10 cm) and a layer representing the non-harrowed subsoil (10 – 90 cm depth).

A sequential iterative approach was used to determine the parameters of the two soil layers. In the first step a homogeneous soil profile was assumed. Its hydraulic properties were estimated using soil surface temperatures and water contents at a depth of 7 cm. During the second step, the soil profile was divided into two horizons, with the parameters estimated in the first step assigned to the surface soil layer (0-10 cm) and the parameters of the subsurface layer (10-90 cm) derived from water content measurements in 15-cm depth. Since soil surface temperatures and water contents are influenced by the hydraulic properties of both layers, the hydraulic properties of the individual soil layers were successively updated in subsequent steps, while keeping the parameters of the other layer fixed, until the estimated hydraulic properties of both layers stopped changing between subsequent steps. The iterative process converged after three iterations.

This approach represents an MO inversion, since both water contents and soil surface temperatures are used during this parameter optimization process. For each step, the prior distribution of the parameters of the soil layer of which the parameters were estimated was set to the initial prior distributions. For the last step, the posterior distributions of the van Genuchten-Mualem soil hydraulic parameters for the upper part of the soil were estimated using only soil surface temperatures (the SO approach) and soil surface temperature and water content measurements in 7-cm depth (the MO approach), while keeping the soil hydraulic parameters for the deeper part of the soil profile constant. Except for the last step of the iteration process, the DREAM algorithm was used only until convergence, which greatly sped up computational time. Therefore no confidence intervals for the best estimate of the hydraulic properties for the lower soil layer (0 – 90 cm) were obtained (Table 4.4). The focus was mainly on the upper part of the soil profile, since our additional modeling showed that soil surface temperatures did not contain sufficient information to infer soil water dynamics of the second, deeper layer of the soil profile.

Table 4.4 Van Genuchten-Mualem parameter sets and their 95% confidence intervals of a layered soil profile (0 – 10 cm and 10-90 cm) that are estimated from measured data using a single-objective (SO) and multi-objective (MO) approach. The soil hydraulic properties of the deeper soil layer (10 – 90 cm) were estimated iteratively using the TDR measurements at 15 cm depth. Numbers in parenthesis are the lower and upper bands of the 95% confidence interval. The parameter range gives the upper and lower limits allowed for each parameter during the optimization.

	Measurement Data	**θ_r [cm^3 cm^{-3}]**	**θ_s [cm^3 cm^{-3}]**	**α [cm-1]**	**n [-]**	**K_s [cm d^{-1}]**
0-10 cm	*Soil Surface Temperature (SO)*	0.1083 (0.0322 – 0.1500)	0.2811 (0.2102 – 0.4427)	0.1232 (0.0128 – 0.1916)	1.4669 (1.1971 – 1.9671)	16.2378 (1.0454 – 108.8930)
	Soil Surface Temperature + Water Content (7cm) (MO)	0.1132 (0.0732 – 0.1181)	0.3097 (0.2720 – 0.3413)	0.1862 (0.1413 – 0.1998)	1.8664 (1.6146 – 2.0000)	5.4761 (4.3361 – 35.7108)
10-90 cm	*Water Content (15 cm)*	0.0538	0.3902	0.0339	1.5701	23.6872
	Parameter Range	0.000 – 0.150	0.250 – 0.450	0.003 – 0.200	1.100 – 2.000	1.00 – 500.00

Soil hydraulic parameters estimated from field measured surface temperatures and from both temperatures and water contents (Table 4.4) differ more than those estimated from synthetic data. The best estimate of van Genuchten-Mualem parameter n, shows the largest difference between the two approaches (SO: n = 1.42; MO: n = 1.89). However, the posterior parameter distribution of n remains nearly uniform, indicating that n cannot be identified with the SO approach. The uncertainty of all optimized parameters is considerably larger when only surface temperatures compared to combined use of surface temperatures and soil water content measurements (e.g. CI95 for K_s with SO: 1.05 – 108.89 cm d^{-1}, CI95 for K_s with MO: 4.34 – 35.71 cm d^{-1}, Figure 4.9). For the SO approach, the parameter uncertainty is also considerably larger than that in the synthetic experiment.

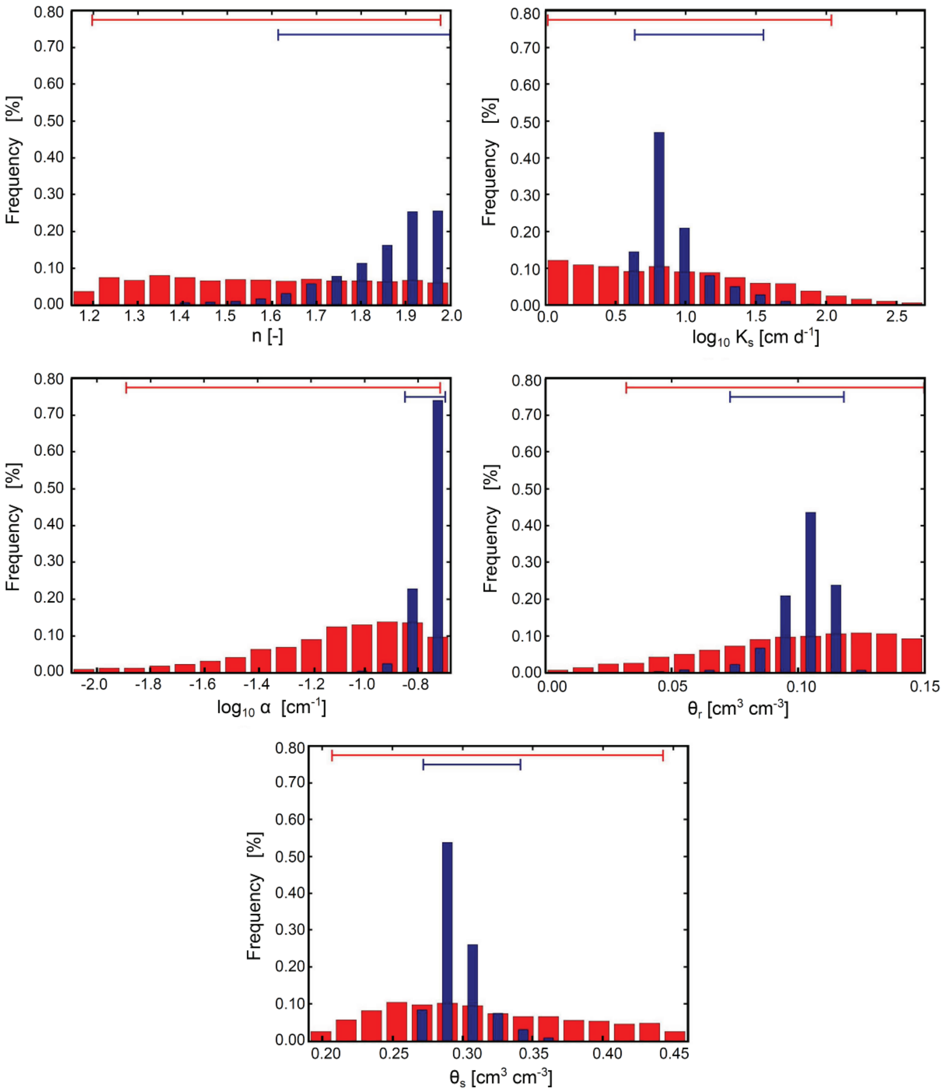

Figure 4.9: Probability density functions (pdfs) of the optimized van Genuchten-Mualem parameters for the 0-10 cm layer for the field experiment. Red (wide bars) histograms show the pdfs resulting from single objective (SO) optimization (soil surface temperature data only), blue (narrow bars) histograms show the pdfs for a multi-objective (MO) optimization (soil surface temperature and water content data). In the upper part of every plot, the 95% confidence intervals are given for the SO (upper red line) and MO (lower blue line) approaches.

The CI95 in the synthetic experiment calculated from the SO approach for θ_r ranges from 0.037 – 0.105 cm^3 cm^{-3}, whereas it ranges from 0.03 – 0.15 cm^3 cm^{-3} in the field experiment.

For α and n parameters, the additional use of water content data led to a concentration of the probability mass at the upper boundary of the parameter ranges. The value ranges for these parameters could not be extended, due to numerical instabilities and unrealistic behavior in the model.

Water retention curves resulting from the best van Genuchten – Mualem parameter sets and their 95th confidence intervals are shown in Figure 4.10 for the SO and the MO approach. As expected, examinating the posterior parameter distributions (Figure 4.9), the uncertainty in the optimized retention curve is considerably reduced when soil water content data are considered together with soil surface temperature measurements in the optimization process.

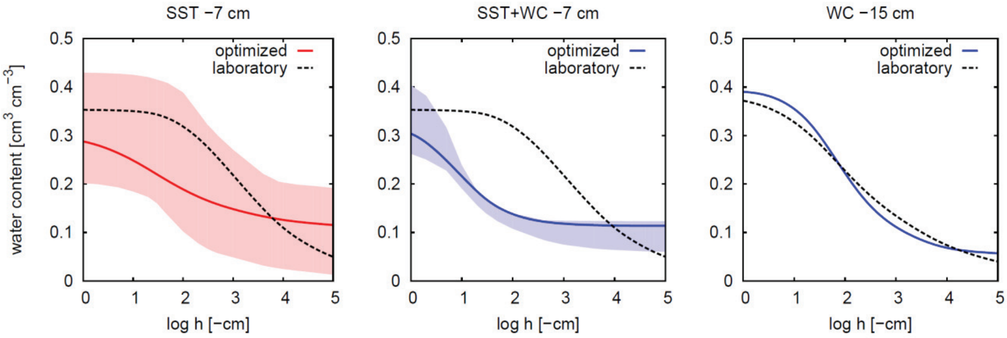

Figure 4.10: Soil water retention curves for the optimized van Genuchten-Mualem parameter sets for the upper (0 – 10 cm; left and middle plot) and lower parts (10 – 90; right plot) of the soil profile. The red line (left plot) represents the water retention curve optimized using only soil surface temperature measurements (SST). The blue line (middle plot) represents the water retention curve optimized using both soil surface temperature and water content measurements (SST+WC). Shaded areas represent the 95% confidence intervals in terms of water contents. The right plot shows the soil water retention curves determined using the sand bed and the pressure plate method (dashed line) and optimized using TDR measurements (solid line) in the 15-cm depth.

Figure 4.10 also compares the estimated water retention curves against those determined in the laboratory (Table 4.1). Both the SO- and MO-derived water retention curves for the surface soil layer deviate considerably from the retention curve determined in the laboratory. Both estimated retention curves are characteristic of a soil with a coarser texture (i.e., larger α parameter). The optimized retention curve for the top soil layer also deviates considerably from the retention curve derived for the deeper soil layer, which shows more resemblance to that determined in the laboratory. This indicates larger pore sizes in the top soil layer than what would normally be observed for a soil with this texture. The bulk density of the top soil has been decreased by harrowing at the beginning of the experiment, which may explain the effect on α. Despite the larger uncertainty of the SO-estimated hydraulic parameters, it is still possible to infer that hydraulic properties of the disturbed top soil layer are considerably different from hydraulic properties determined on undisturbed soil samples.

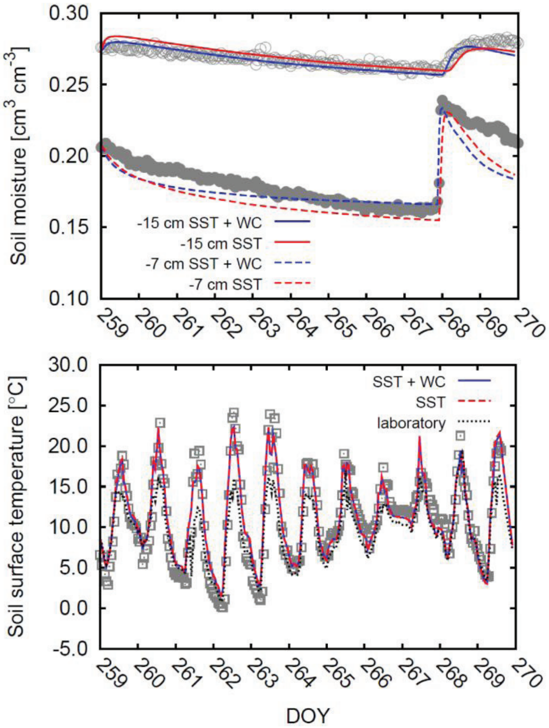

Figure 4.11: Soil water contents (upper plot) and soil surface temperatures (lower plot) calculated using the van Genuchten-Mualem parameters estimated from SST (red lines) and SST+WC (blue lines) data. The right plot also shows soil surface temperatures (dotted line) calculated using the soil hydraulic properties determined in the laboratory on undisturbed soil samples. Solid and open circles represent measured water contents at depths of 7 and 15 cm, respectively (left plot), and squares denote measured soil temperatures. Measured surface temperatures and water contents are expressed as an average of all plots.

Due to the lower bulk density of the harrowed upper soil layer than the non-tilled deeper layer, the saturated hydraulic conductivity and the saturated water content are expected to be larger for the upper soil layer. However, fitted K_s and θ_s in the lower soil layer are higher than in the upper soil layer (Table 4.4). This may be due to a lack of information in the wet part of the water retention curve, especially for the upper layer of the soil (measurements at 7-cm) where measured water contents do not exceed values around 0.24 cm^3 cm^{-3}. As a consequence, the estimated saturated hydraulic conductivity and water content are an extrapolation of hydraulic properties which were derived for drier soil conditions. For aggregated or tilled soils with a considerable interaggregate porosity, this extrapolation may lead to a considerably underestimation of the real saturated hydraulic conductivity and water content. A measurement period covering a wider range of dry and wet soil conditions may give better results concerning saturated hydraulic conductivity and the saturated water content.

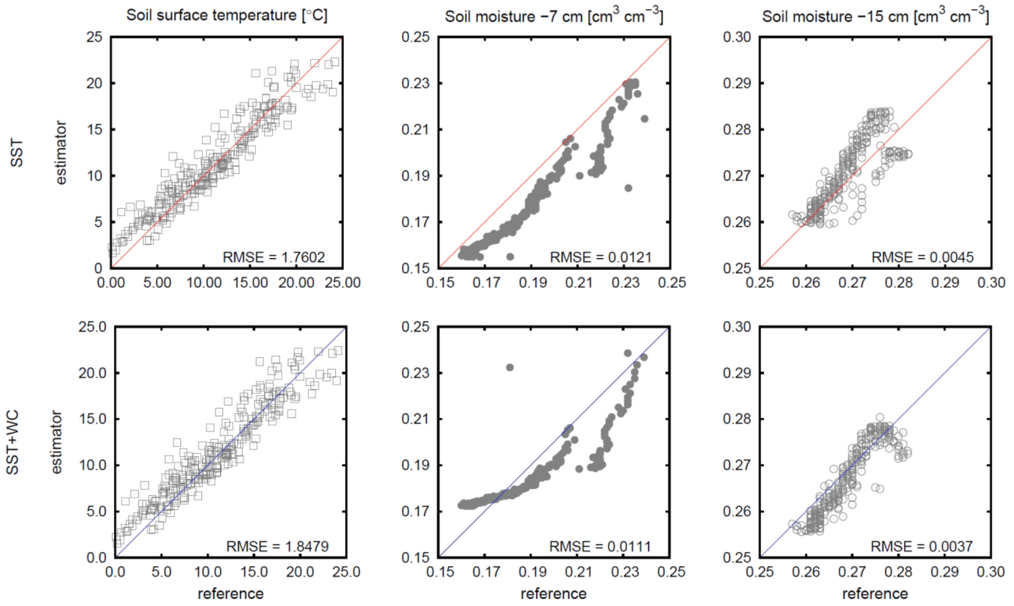

Figure 4.12: Modeled temperatures and water contents (*y*-axis) plotted against the field measurements (*x*-axis). The results for parameters estimated inversely from soil surface temperatures (SST) are shown in the top row. The results for parameters estimated using both soil surface temperatures and soil water contents (SST+WC) are shown in the bottom row.

As already noted before for the synthetic experiment: Including soil water content measurements in the parameter estimation improves the fit of the soil water dynamics (see Figure 4.12). However, the improvement for the real dataset is not as pronounced as it was for the synthetic experiment. This can be seen in the RMSE for the water content at e.g. 7 cm depth, which is reduced from 0.012 cm^3 cm^{-3} for the SO approach to 0.011 cm^3 cm^{-3} for the MO approach. Since the optimal parameter sets that were obtained from SO and MO were similar, the reduction in RMSE of the soil water content fit by the MO is small (Figure 4.12).

Figure 4.11 shows water contents and surface temperatures simulated using parameters determined by both SO and MO approaches. Both approaches show a good agreement between measured and modeled water contents and soil surface temperatures. The RMSE for the water content in 7-cm depth is 0.012 cm^3 cm^{-3} for the SO approach and 0.011 cm^3 cm^{-3} for the MO approach. At 15-cm depth the RMSE calculated from the SO approach is 0.0046 cm^3 cm^{-3} and 0.0037 cm^3 cm^{-3} for the MO approach. The soil water dynamics at 7-cm depth following the rain event around DOY 267 of the field experiment were less well described, which probably indicates inadequacies of the unimodal van Genuchten-Mualem model.

Figure 4.11 also shows surface temperatures simulated using soil hydraulic parameters determined in the laboratory. Simulated surface temperatures significantly underestimate peak measured temperatures, which shows that not only soil water dynamics but also soil surface temperatures strongly depend on the soil tillage.

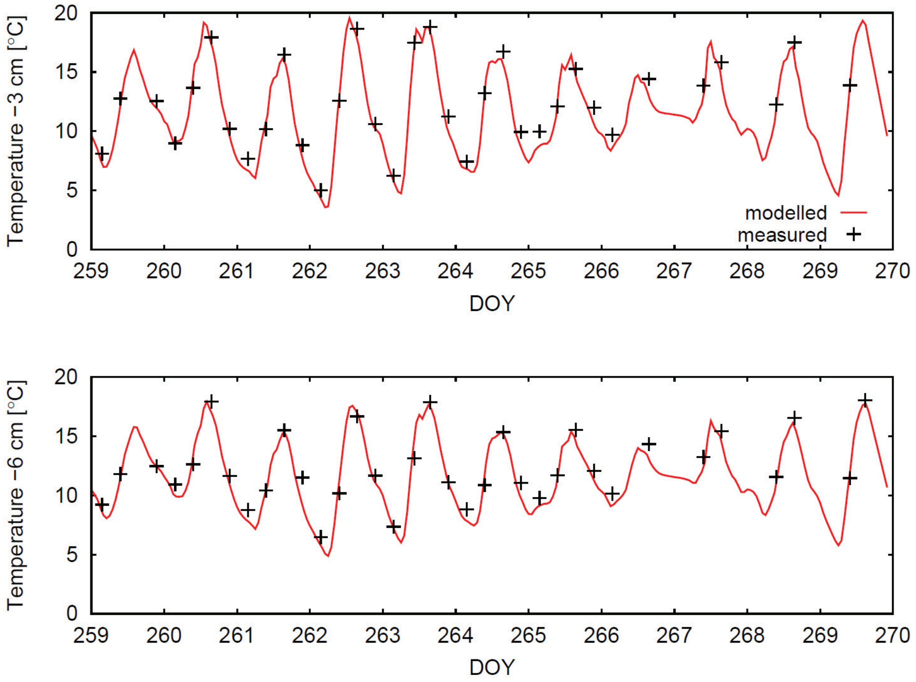

Figure 4.13: Measured and simulated soil temperatures at depths of 3 and 6 cm. Simulated values were obtained with the van Genuchten-Mualem parameter set determined using the MO approach.

As a validation of the simulations and estimated soil hydraulic parameters, it was determined whether soil temperatures measured at depths of 3 and 6 cm could be simulated properly with the parameterized model. Since both best parameter sets (from SO and MO approach) predict nearly identical temperatures in both depths, only soil temperatures simulated using the MO parameters are plotted in Figure 4.13. It shows that modeled and measured soil temperatures are in good agreement. Dampening of the amplitude of the diurnal temperature variation from the soil surface to depths of 3 and 6 cm was predicted well by the model.

4.4 Summary and conclusion

Estimating soil hydraulic properties using inverse modeling of the informational content of the soil surface temperature was analyzed in this chapter. To quantify the constraints soil surface temperature has on the estimation of soil hydraulic parameters, soil hydraulic parameters were estimated using a single-objective approach, which considered only soil surface temperatures, and a multi-objective approach, which considered both soil surface temperatures and TDR-measured soil water contents. A synthetic experiment showed that although soil surface temperature contains enough information to estimate soil hydraulic parameters, their uncertainties can be reduced by additionally considering also water content measurements.

A field experiment was then carried out to test whether hydraulic properties can be estimated using this approach under prepared field conditions. An attempt to find effective soil hydraulic properties characterizing the entire soil profile that could be used to describe field measured soil temperatures and water contents at different depths was not successful. This shows that models, which try to describe water dynamics in layered soils using a single effective hydraulic parameter set (as most land-surface models do) may lead to wrong predictions of soil surface states (water contents and temperatures) and fluxes across the soil-atmosphere boundary, which are important for characterizing soil-atmosphere interactions. Considering a two-layered soil profile, it was found that the hydraulic properties of the soil surface layer were considerably different (e.g. α = 0.187 cm^{-1} for the MO approach) from those of the deeper soil (α = 0.0339 cm^{-1}) and from the hydraulic properties derived in the laboratory on undisturbed soil columns (α = 0.069 cm^{-1}). The hydraulic properties that were optimized for the top layer of the silty-loam soil were more typical for a coarse sandy soil and characterized by a high value of the α parameter of the van Genuchten-Mualem function. This indicates the important effect of soil tillage on hydraulic properties of the soil surface layer, and its consequences for soil-atmosphere interactions. Consequently, the effects of soil tillage (harrowing, grubbing, ploughing) on surface temperature measurements and the resulting estimated soil hydraulic properties are uncertain and need to be studied further (see Section 6.2).

Since the soil surface temperature measurements did not contain enough information to infer the hydraulic properties of the deeper part of the soil profile, the deeper part of the soil was parameterized using soil water contents measured using TDRs installed at a depth of 15 cm. Compared to the shallow soil layer, the obtained water retention curves for the deeper soil layer corresponded better with those derived on laboratory columns. This indicates that soil surface temperature measurements should be combined with information about subsurface soil water contents to derive the soil hydraulic properties of the top soil layer. Soil surface temperatures can be observed at a relatively large scale, and could be used to infer information about the effects not only of spatial, but also temporal, variations in surface soil properties, such as those due to soil tillage, on soil hydraulic properties and soil atmosphere interactions. However, this information should be combined with spatial information about the subsurface soil water contents, which could be obtained using networks of soil water content sensors (Rosenbaum et al., 2009). How to combine these two sources of information on larger scales and how to address the problems involved in the variability of parameters at various scales requires further research (see Section 6.2).

The soil hydraulic parameters of the upper soil layer, inversely estimated only from soil surface temperature measurements, were associated with considerable uncertainty (e.g. CI95 for n: 1.33 – 1.98). Nevertheless, the soil hydraulic parameters and corresponding water retention curves that were obtained using only soil surface temperatures or a combination of temperature and soil water content measurements were similar and could both be distinguished from soil hydraulic properties of the deeper undisturbed soil. Comparing the results obtained using the synthetic and real field experiments indicates that synthetic experiments are important tools to outline the general applicability of a particular method, but can only provide a first approximation about the actual performance of the method under field conditions. Considering a layered soil profile, both parameter sets estimated from field measured data (using MO and SO approaches) led to similar predictions of near-surface soil water dynamics (RMSE for θ in e.g. 7 cm: 0,012 cm^3 cm^{-3} (SO approach); 0.011 cm^3 cm^{-3} (MO approach)), indicating that the proposed method can be applied under field conditions. However, drying-wetting cycles are required to derive soil hydraulic properties form soil surface temperature measurements since it is not possible to relate the soil surface temperature to the soil hydraulic properties in dry soils where heat transfer is controlled by heat conduction.

Finally, the range of soil hydrological conditions, i.e., the range of soil water contents and the range of boundary conditions (radiation, evaporation rates, temperatures), during our experiment was limited. Observations of soil surface temperatures in different plots with different soil surface structure and over a longer time period, containing more than one drying-wetting cycle, may considerably reduce the parameter uncertainty and should be subject of further research.

5 Horizontal fluxes and their influence on evaporation from heterogeneous soils

5.1 Introduction

To correctly define evaporation from bare soils, water and heat flux as well as their interactions need to be well understood: According to Lehmann et al. (2008) capillary water flow through hydraulically connected soil regions towards the soil surface sustains a high and relatively constant evaporation rate also called stage one evaporation. A drying front, which marks the boundary between fully and variably saturated soil, develops and recedes into the soil. However, the evaporative front remains at the soil surface during stage one. Eventually, the hydraulic and capillary interconnection in the soil is no longer high enough to fully sustain the evaporative demand. In the following stage two evaporation, water evaporates no longer at the soil surface but at an evaporative front, which further recedes into the soil with ongoing evaporation. Evaporation is now controlled by vapor diffusion between the evaporative front and the soil surface (Lehmann et al., 2008). As incoming energy is no longer consumed for evaporation at the soil surface, the soil surface is heating up stronger in stage two evaporation compared to stage one evaporation. It follows that soil temperatures are closely linked to evaporation rate and soil water content. This is also shown by Kalma et al. (2008) who reviewed several large-scale methods to estimate land surface evaporation from remotely sensed temperature data or by Moran et al. (1996) who modified the *Penman-Monteith equation* to include soil temperatures and reflectances to estimate evaporation rates. On a smaller scale, similar studies to estimate soil evaporation based on soil temperature were performed by Ben-Asher et al. (1983). In an early small-scale laboratory study, Hanks et al. (1967) studied evaporation from soil as influenced by wind or radiation drying. Hanks et al. (1967) showed that different water content profiles develop when using radiation or wind drying. They observed that higher temperature gradients develop within the soil column when using radiation drying and concluded that water vapor fluxes within the soil following a thermal gradient caused the differences in soil water content development under different drying mechanisms, thereby demonstrating the connection between evaporation, water content and soil temperature. In a more recent laboratory study, Sakai et al. (2009) used data of Miyazaki (1976) and studied condensation and evaporation of water and water vapor within a dry sandy soil column. The open top of the sandy soil column was exposed to hot and humid air, whereas the closed bottom was kept at a constant temperature of 20°C. From the laboratory experiment, Miyazaki (1976) observed that liquid water accumulated at the bottom of the soil column, successively moving upward towards the top end of the soil column where it evaporated. Sakai et al. (2009) used numerical methods considering water and vapor flow according to hydraulic and thermal gradients to interpret the experimental results from Miyazaki (1976). They concluded that with the beginning of the experiment, water vapor entered the soil column from the hot top, condensing at the cooler bottom after following the thermal gradient within in the soil. Accumulated liquid water was observed to follow the hydraulic gradient and moved toward the top of the soil column. Both, laboratory (Miyazaki, 1976) and numerical (Sakai et al., 2009) experiments show the mutual interaction of soil temperature and water content and their influence on evaporation and condensation. Apart from laboratory experiments, an early field study by Rose (1968a, b) monitoring temperature and water content in field soils showed that the daily temperature wave influences moisture fluxes. Goss & Madlinger, 2007) focused on the connection between water content or evaporation rate and soil temperature.

Most of these studies concerning heat and water fluxes within soils are one-dimensional and assume homogeneous (one-material) or horizontally layered soil profiles, thereby neglecting horizontal heat and water fluxes. However, if a two- or three-dimensional soil with two or more different materials in vertical contact is assumed, horizontal fluxes may not be negligible:

In a recent study, Lehmann & Or (2009) used hydraulically coupled soil columns in vertical contact to study evaporative losses from non-homogeneous surfaces in a laboratory experiment. It was shown that evaporation mostly takes place from the fine medium. Depending on the difference in air entry values of both materials, the drying front propagates exclusively within the coarse material part at first (Lehmann & Or, 2009). This results in a difference in capillary pressure between fine and coarse material causing a horizontal water flux from coarse to fine material.

In another study, Shahraeeni & Or (2010) used infrared thermography to measure spatiotemporal patterns of soil temperatures in heterogeneous soils to infer spatiotemporal distributions of evaporative fluxes. Evaporative fluxes from horizontally heterogeneous soils become spatially variable when the evaporative demand can no longer be sustained by the coarse material. As a consequence, incoming energy is no longer consumed at the coarse soil surface and distinct temperature fields develop. At this point, both, the hydraulically controlled stage one evaporation (within the fine soil) and the vapor diffusion controlled stage two evaporation (within the coarse soil) contribute to the overall evaporation rate, leading to a mixed stage evaporation rate. Additionally, surface temperature fields induce heat exchange between both materials. It is theorized that these heat fluxes influence the actual evaporation of the fine material in a way that the constant rate stage one evaporation exceeds the atmospherically demanded potential evaporation rate from a homogeneous soil surface.

The actual studies from Lehmann & Or (2009) and Shahraeeni & Or (2010) show that evaporation from vertically heterogeneous soils still maintains the known basic characteristics of constant (stage one) and falling (stage two) rate evaporation. However, the current understanding of evaporation from homogeneous soil surfaces needs to be expanded for vertically heterogeneous soils by considering horizontal water and heat fluxes which have an important influence of the evaporation behavior. A numerical model capable of simulating these effects of horizontal fluxes needs to incorporate two important aspects: (a) Interaction between water movement and heat fluxes due to temperature and hydraulic gradients and, (b), an energy balance boundary condition providing upper boundary heat and water fluxes for every time step of numerical modeling. As boundary fluxes strongly depend on actual temperature and water content prevailing directly at a certain point on the soil surface, the energy balance additionally needs to be solved at every individual surface boundary node point to preserve (and allow development of) spatial differences in temperature and water content. In this chapter, it is tested whether a fully coupled, three-dimensional model can represent spatial patterns and interactions in evaporation and temperature consistently with recent experimental results. Using the coupled model, the influence of vertical contact between different soil materials on total evaporation and the effect of horizontal heat and water fluxes on enhanced and/or extended stage one evaporation is investigated.

5.2 Materials and methods

As ambient atmospheric conditions and horizontal heat fluxes define the amount of energy available for evaporation, a fully coupled three-dimensional model incorporating an energy balance boundary condition is required to numerically model horizontal fluxes and their influence on temperature and evaporation rate. For this reason a modified HYDRUS-3D source code taking vapor flow into account and allowing for an atmospheric energy balance boundary condition was used This is not the case in the actual public version of HYDRUS-3D.

Please note that water vapor, even though taken into account, had a negligible effect on the presented modeling results. This was shown by comparison of model runs including and ignoring vapor flow. Convergence problems did not allow for a model framework which clearly demonstrated the effects of water vapor on horizontal heat and water fluxes and their influence on evaporation. Nevertheless, the following results provide a reasonable basis for the discussion of evaporation from heterogeneous soils.

Governing equations describing coupled heat and water fluxes and details about the energy balance boundary condition can be found in Sections 2.1.3 and 2.2, respectively.

5.2.1 Surface energy balance implementation

Due to differences in the evaporative behavior of soils with different hydraulic properties, variable temperatures develop in the upper part of systems with laterally variable soil properties. Vice versa, variable soil surface temperatures affect the actual evaporation rate of a soil. If one average energy balance equation for a heterogeneous soil surface is used as upper boundary condition, an average soil surface temperature, vapor pressure and evaporation rate is derived for the entire soil surface so that spatial variations at the soil surface are flattened out. Consequently, a surface energy balance equation was implemented for every surface boundary node exposed to atmospheric conditions.

As discussed in Sections 2.1.3 and 2.2, the evaporation rate E_n [kg m^{-2} s^{-1}] of a boundary node *n* is defined as

$$E_n = \left(\frac{\rho_s - \rho_a}{r_a} \right) \qquad 5.1$$

The absolute actual flux q_n at boundary node *n* with coordinates *(x,y,z)* and at its corresponding boundary segment is defined by

$$q_i = \left| \left(\left(K_{lh} + K_{vh}\right) \left(K_{ij}^{A} \frac{\partial h}{\partial x_j} + K_{iz}^{A} \right) + \left(K_{lT} + K_{vT}\right) \left(K_{ij}^{A} \frac{\partial T}{\partial x_j} \right) n_i \right) \right| \Bigg|_{n(x,y,z)} = \frac{E_n}{\rho_w} \qquad 5.2$$

where n_i are the components of the outward unit vector normal to the corresponding boundary segment. Here, E_n/ρ_w is the actual evaporation or infiltration flux under the current meteorological conditions (Šimůnek et al., 2006). The amount of water actually evaporated or infiltrated during a certain time step is calculated as

$$Q_n = -A_n \cdot \frac{E_n}{\rho_w} \qquad 5.3$$

where Q_n [m^3 s^{-1}] is the volume of water evaporated or infiltrated, A_n [m^2] is a part of surface area of the boundary segment(s) associated with boundary node n. The calculation of every A_n is done as follows.

$$A_n = \sum_{i=1}^{k} \frac{F_i}{N_i^{BP}} \qquad 5.4$$

where F_i [m^2] is the total area of the i^{th} boundary segment deploying n as an adjacent node point and N_i^{BP} [-] the total number of node points forming the i^{th} boundary segment (which in case of tetrahedral elements always equals 3).

An influence of horizontal fluxes is expected to be strongest directly at the contact zone between two different materials. Depending on the dimensions of the modeled domain, node points close to the contact of both materials may show an increased temperature due to horizontal heat fluxes, whereas boundary points at a greater distance may show no increase. Hence, solutions of Eqs. 5.1 and 5.2 require knowledge of node specific values of T and/or h and a solution of the energy balance is required for every surface boundary node point in the modeling domain.

5.2.2 Model parameterization

As modeling domain, a uniform cuboid with dimensions of 11 cm x 5 cm x 100 cm in the directions of x, y, z (respectively) was used, resulting in a volume of 5500 cm^3 and upper and lower boundary surfaces of 55 cm^2 each. Initial numerical test runs have shown that these dimensions are sufficient to simulate the effects of horizontal heat and water fluxes in a relatively short computation time of approximately 120 minutes per run.

Additionally, relatively small modeling domains simplify potential laboratory setups, making comparisons of potential experimental and simulated results easier. A simple structured finite element mesh, consisting of 11000 triangular prism elements with 7272 node points in total was chosen. Discretization in x, y, and z is 1 cm in each direction, which proved to be fine enough as finer discretizations gave no significant change in simulation results.

Initial and boundary conditions are required to solve the coupled heat and water flux equations described in Section 2.1.3. For the beginning of the simulation, a fully saturated soil profile with a homogeneous temperature of 20°C was chosen. At the bottom of the soil column, a zero flux boundary condition for heat and water flux was implemented. As already mentioned, the regular HYDRUS-3D code was modified to allow an energy balance boundary condition at the top of the modeling domain. Heat and water flux at soil surface are being deduced from the solution of this surface energy balance equation (see Sections 2.2 and 5.2.1) at every top boundary node point of the modeling domain.

Two materials with different hydraulic properties, parameterized with the van Genuchten – Mualem model, are used (Figure 5.1) to study the effect of horizontal fluxes within the modeling domain over a modeling duration of 10 days. One part of the soil column (x range: 0 – 5 cm; y range: 0 – 5 cm; z range: 0 – 100 cm) was defined to consist of the coarser material 2 (M2), the other part (x range: 5 – 11 cm; y range: 0 – 5 cm; z range: 0 – 100 cm) of the finer material 1 (M1). This resulted in a soil column with two materials in direct vertical contact with contact zone defined by the y –z plane at x = 5 cm.

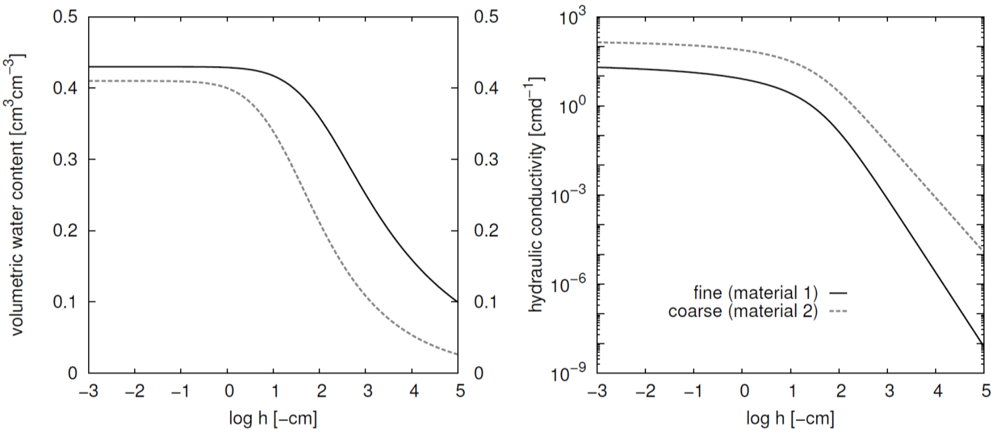

Figure 5.1: Soil water retention (left) and hydraulic conductivity curve (right) of material 1 (fine) and material 2 (coarse) used for simulation.

Soil thermal properties needed for the simulation of heat fluxes are defined according to Chung & Horton (1987) (Figure 5.2). It is theorized that heat fluxes resulting to different temperatures in both materials have an effect on the evaporation rate. Therefore, the same Chung & Horton (1987) parameters were used to rule out heat exchanges due to differences in soil thermal properties of both soils.

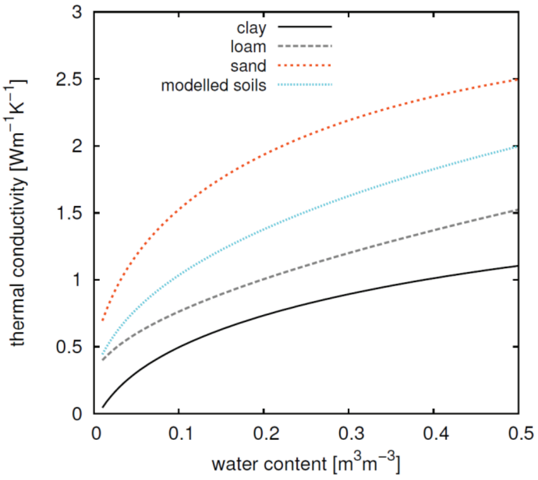

Figure 5.2: Soil thermal properties parameterized by the Chung & Horton model (1987). The dotted cyan line shows the used thermal conductivity curve in comparison with the thermal conductivity curves of a clay (solid black), a loam (short dashed red), and a sand (long dashed grey). The same thermal conductivity function was used for both modeled soils (coarse and fine).

Meteorological conditions representing constant evaporative conditions are used to solve the surface energy balance equation. To solve the energy balance equation, the net radiation is needed. However, the outgoing (from soil to air) longwave radiation depends on soil surface temperature, which itself is a modeling result. Consequently, the net radiation (as a sum of longwave and shortwave radiation) cannot be taken as input parameter, because spatially different surface temperatures are to be expected during simulation, which lead to differences in longwave radiation and thereby are having an effect on the net radiation. Consequently, incoming shortwave radiation was taken as input parameter for the solution of the energy balance equation. The mandatory net radiation is calculated internally from the incoming shortwave and the outgoing longwave radiation, which is calculated based on the boundary node specific soil temperature. All parameters used to solve the surface energy equation are listed in Table 5.1.

Table 5.1: Modeling parameters used during the simulation of two different soil types in direct horizontal contact.

hydraulic properties	θ_s	θ_r	α	n	K_s	l
unit	[cm^3 cm^{-3}]		[cm^{-1}]	[-]	[cm d^{-1}]	[-]
Material 1 (fine)	0.43	0.0	0.015	1.2	24.96	0.50
Material 2 (coarse)	0.41	0.0	0.095	1.2	150.10	0.50
thermal properties#	b_1	b_2	b_3	C_n	C_w	λ_{L+T}
unit		[W m^{-1} K^{-1}]		[J m^{-3} K^{-1}]		[cm]
Material 1 (fine)	0.15	-0.55	2.99	1.92×10^6	4.18×10^6	1.00
Material 2 (coarse)	0.15	-0.55	2.99	1.92×10^6	4.18 ´ 10^6	1.00
meteorologic parameters‡		Rad	v_{wind}	H_r	T_{air}	$T_{profile}$
unit		[MJ m^{-2} d^{-1}]	[km d^{-1}]	[%]	[°C]	
		10	200	25	30	20

C_n: volumetric heat capacity of solid phase; C_w: volumetric heat capacity of liquid phase;
λ_{L+T}: longitudinal and transverse dispersivity

‡ *Rad: radiation; v_{wind}: wind speed; H_r: relative humidity; T_{air}: air temperature;*
$T_{profile}$: initial profile temperature

5.3 Results and discussion

To characterize the effects of horizontal fluxes, modeled evaporation and temperature development of a mixed-material soil column was compared with those of two soil columns described exclusively by parameters for fine and coarse soil (Table 5.1). Simulation period was set to ten days.

5.3.1 Uniform and two-material soil evaporation

Evaporation in homogeneous soils is known to be defined by a constant, atmospheric controlled evaporation (stage one) and a dropping evaporation phase (stage two), which is controlled by the soil's hydraulic properties (e.g: Shahraeeni & Or, 2010; Fraure and Coussot, 2010). Figure 5.3 shows this classical behavior for a uniform fine and uniform coarse soil column. Please note that the values shown in all plots of Figure 5.3 are presented as mean values over the whole surface of each soil column.

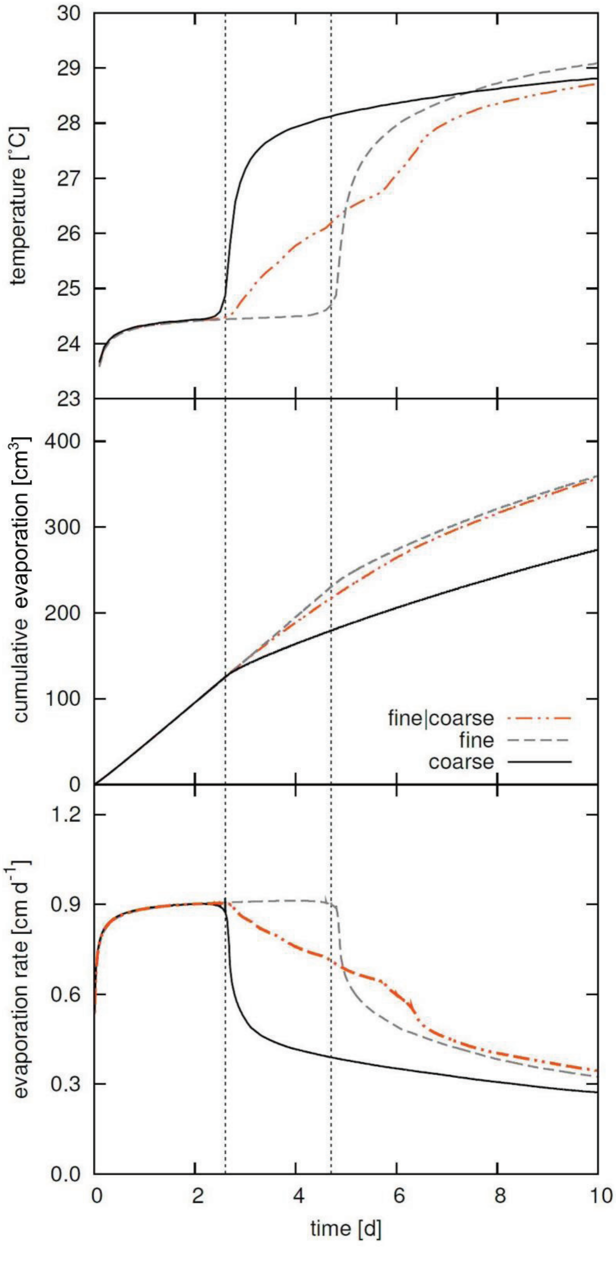

Figure 5.3: Comparison of surface temperature (top), cumulative evaporation (middle), and evaporation rate (bottom) of a homogeneous fine (dashed grey), a homogeneous coarse (solid black), and a horizontallly heterogeneous (dashed-dotted amber) soil over time. In all plots, mean values over the whole soil surface are given. The two vertical short dashed black lines in each plot denote the change from stage one to stage two evaporation for the coarse (time ≈ 2.5 d) and the fine (time ≈ 4.5 d) soil.

As expected, both soils, fine and coarse start with a constant evaporation rate of approximately 0.9 cm day^{-1}. After 2.8 days of evaporation, the coarse soil can no longer maintain the atmospherically demanded evaporation rate and the coarse soil's evaporation changes from a stage one (ST1) to a stage two (ST2) evaporation rate. Lehmann et al. (2008) explains this with the assumption that upper soil regions are no longer hydraulically connected and the evaporative front recedes into the soil, resulting in a lower evaporation rate. As evaporation no longer takes place at the soil surface and water vapor diffusion controls the evaporation, soil surface temperature of the coarse soil increases from 24 °C to 28.5 °C and cumulative discharge flattens. The same processes can be seen for the fine soil after ~4.5 days of evaporation. Note that, after 4.0 days, close-surface water content in the uniform fine soil is lower than in the vertically heterogeneous case.

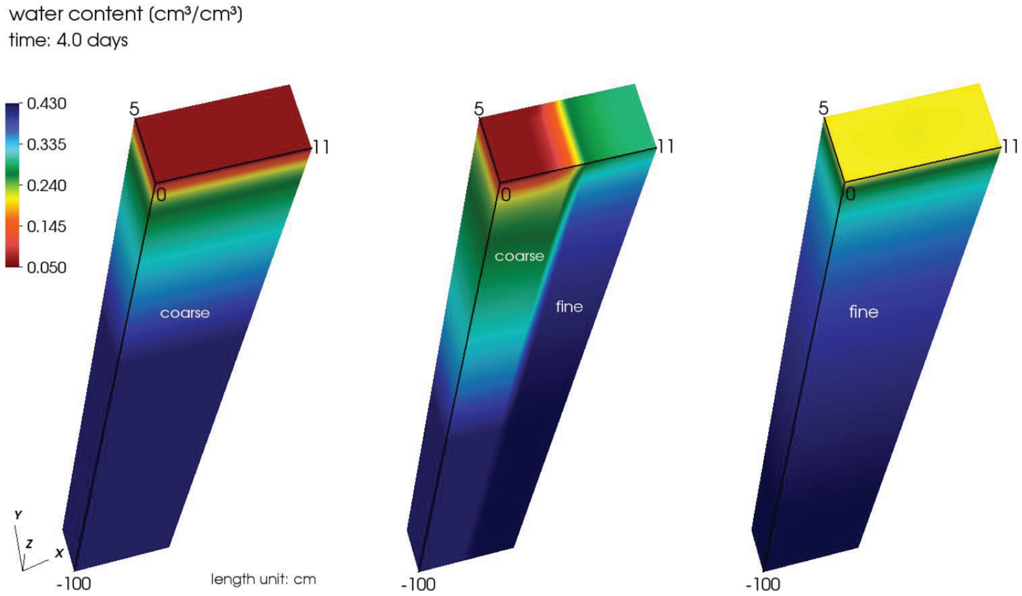

Figure 5.4: Soil water content after 4 days of evaporation of the (left) coarse material, (center) two-material and (right) the fine material soil column. Length unit is centimeter.

Looking on the mean evaporation rate from the two-material soil in Figure 5.3, different evaporation characteristics compared to the uniform soils can be seen. In uniform soil columns, the slope of the curve depicting ST2 evaporation represents the speed at which the soil drying recedes into the soil. In the two-material soil column, the evaporating surface recedes in the coarse soil first while it remains at the surface in the fine material soil (Figure 5.4), causing a less steep slope in mean evaporation rates compared to the uniform material soil. Consequently, the distinction between ST1 and ST2 evaporation in the two-material soil is not as typical as in the uniform material soils. As surface temperature and evaporation rate are dependent, a similar effect can be seen for the temperature plot in Figure 5.3: A steep increase of the surface temperature of the uniform soil columns can be seen, where the mean two-material's surface temperature increases less fast and within two phases. Again, this can be attributed to the temperature development of the individual soil materials. In the first phase, temperature increases in the coarse material because the cooling effect of evaporation diminishes. During this time, evaporation remains high within the fine materials and temperatures remain low. In the second phase, cooling by evaporation also diminishes in the fine material and surface temperatures increase over the whole surface.

Additionally, after ten days of drying, cumulative evaporation from the fine soil is higher (~ 360 cm^3) when compared to the coarse soil (~ 280 cm^3). Despite the fact that the fine soil material makes up only 50% of the evaporating area the total cumulative evaporation from the two-material soil (~355 cm^3) is much more similar to that of the uniform fine material soil than to the surface weighted average of cumulative evaporation from the uniform fine and coarse soil materials. Laboratory experiments by Lehmann & Or (2008) corroborate these simulation results. The amount of water that evaporates within a certain time from a composite surface is not a surface weighted average of the amount of water that would evaporate from its laterally separated parts. This result points at the importance of lateral water fluxes for evaporation losses from a composite porous medium. The larger cumulative evaporation from the composite medium than the surface weighted average of its separated parts could be due to a prolonged duration of the stage I phase of the fine material in the composite medium when water depletion from the fine material is compensated by lateral water flow out of the coarse material. The simulated average evaporation flux from the composite medium is larger than the evaporation from the uniform fine material after 5 d which indicates an extended phase I evaporation from the fine material in the composite medium.

The evaporative fluxes from the composite medium during the time period when the evaporation flux from the separated coarse material decreases and the evaporation from the separated fine material is still in phase I are larger than the surface weighted average of the fluxes from the separated parts. This indicates that the flux from the fine material in the composite material becomes larger than the flux from the separated fine material during phase I. Higher fluxes from the fine part in the composite medium go along with lateral heat fluxes from the heated coarse material. Besides lateral water fluxes, also lateral heat fluxes may be responsible for the larger cumulative evaporative losses in the composite material.

These fluxes are discussed in the next section.

5.3.2 Two-material soil column: Compensated evaporation

A) Water fluxes

Figure 5.5 shows evaporation rates and temperatures for two representative surface boundary nodes in coarse (*x=1; y=3; z=0*) and fine (*x=10; y=3; z=0*) part within the two-material soil column. It can be seen that fine and coarse material start with a constant (stage one) evaporation rate of ~ 0.98 cm day^{-1}.

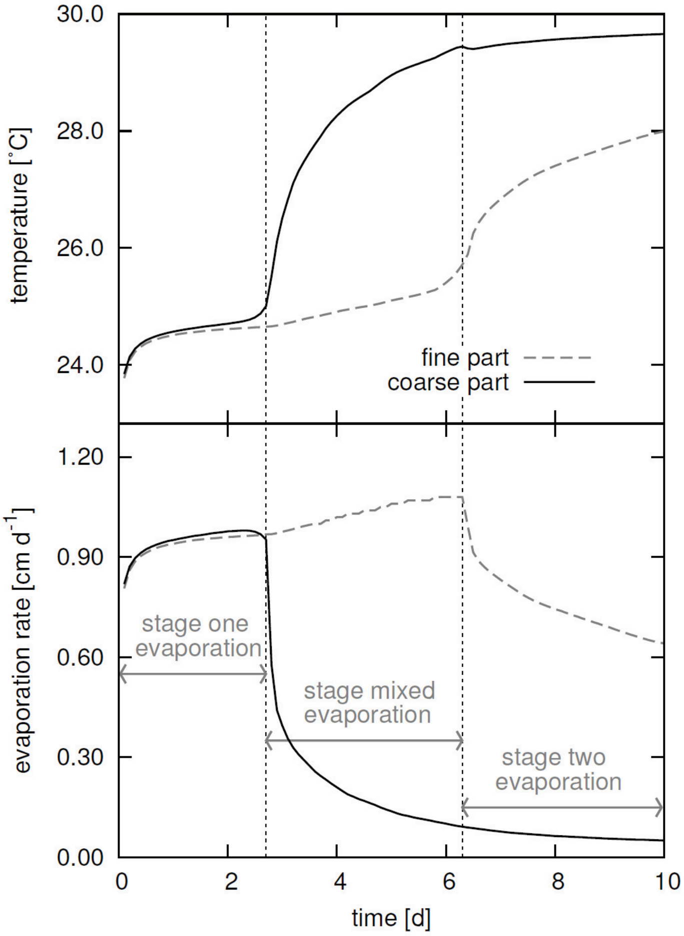

Figure 5.5: (top) Temperature and (bottom) evaporation rate development over 10 days in fine (dashed grey) and coarse (solid black) material of a soil column with both materials in direct vertical contact. Values of two representative surface boundary nodes (coarse: x=1; y=3; z=0; fine: x=10; y=3; z=0) are shown.

At day 2.8, the coarse material reaches ST2 evaporation and evaporation rate drops. This is in agreement with the ST1 evaporation duration of a uniform coarse material column (Figure 5.3). Via its evaporating surface, the coarse material does not significantly contribute to the total surface flux after day 2.8. However, water fluxes from coarse to fine material over the whole duration of the experiment play an important role in the evaporation development of the fine material: Figure 5.6 shows the fluxes at day 1.5 during simulated evaporation. At day 1.5, ST1 evaporation still takes place in both materials.

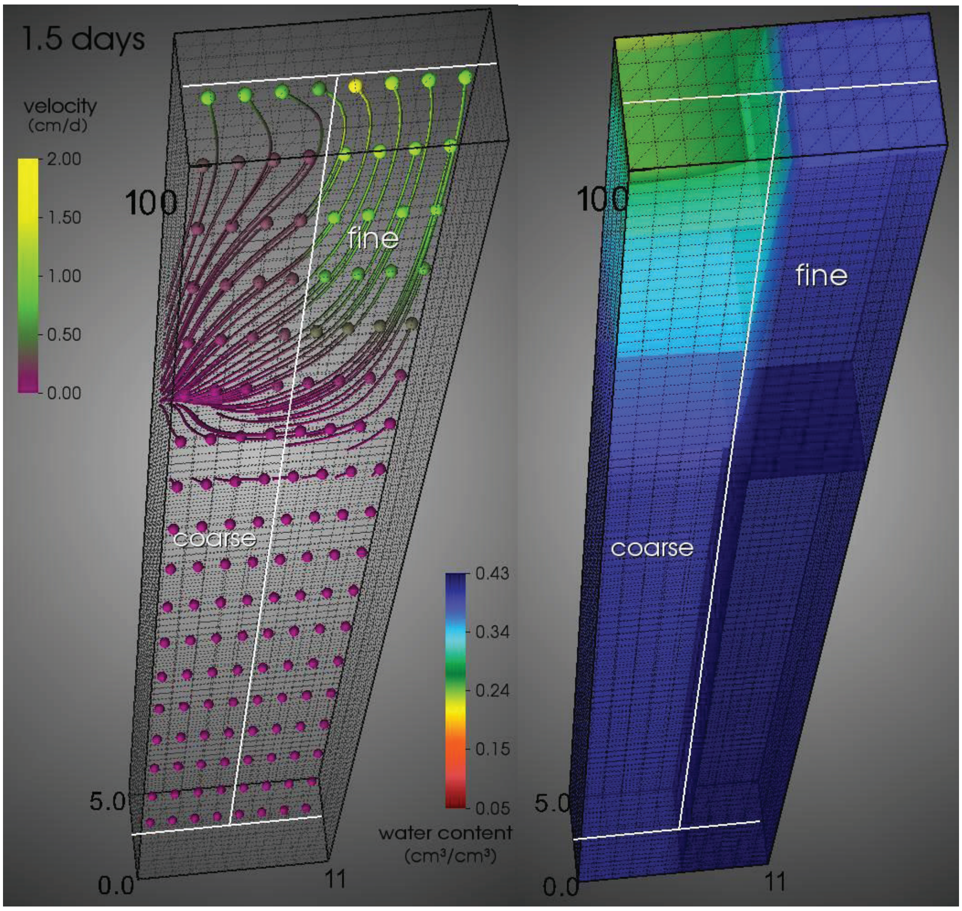

Figure 5.6: Water content and fluxes after 1.5 days of simulated evaporation in a soil column with two materials in vertical contact. Water movement is displayed by streamlines calculated from the vector field, with the streamline color indicating water fluxes within the soil column.

Note that during stage I, water flows laterally from the coarse into the fine material deeper below the soil surface but flows back towards the coarse material close to the soil surface. This phenomenon is corroborated by experiments of Bechtold et al. (2011).

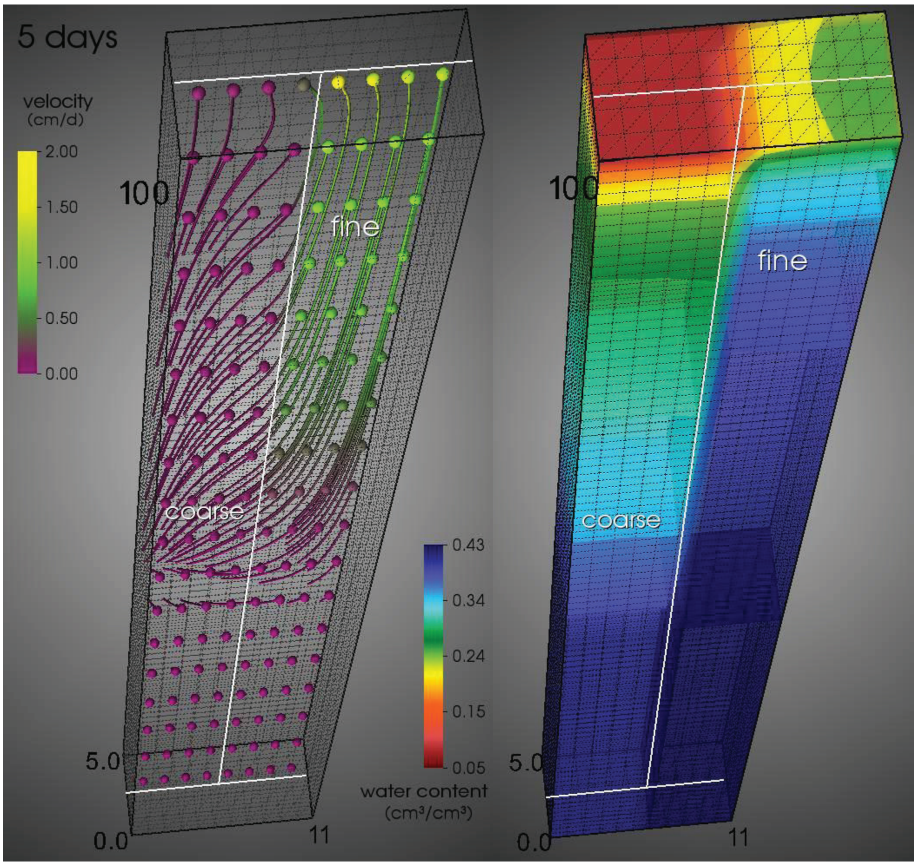

Figure 5.7: Water content and fluxes after 5 days of simulated evaporation in a soil column with two materials in vertical contact. Water movement is displayed by streamlines calculated from the vector field, with the streamline color indicating water fluxes within the soil column.

After 5 days (Figure 5.7), the coarse material's evaporation is reduced to ST2, whereas the fine material still maintains ST1 evaporation. Both materials are in ST2 after 9 days (Figure 5.8) of modeled evaporation. It can be seen that a slow but constant horizontal water flux takes place from coarse to fine material caused by differences in pressure head between both materials.

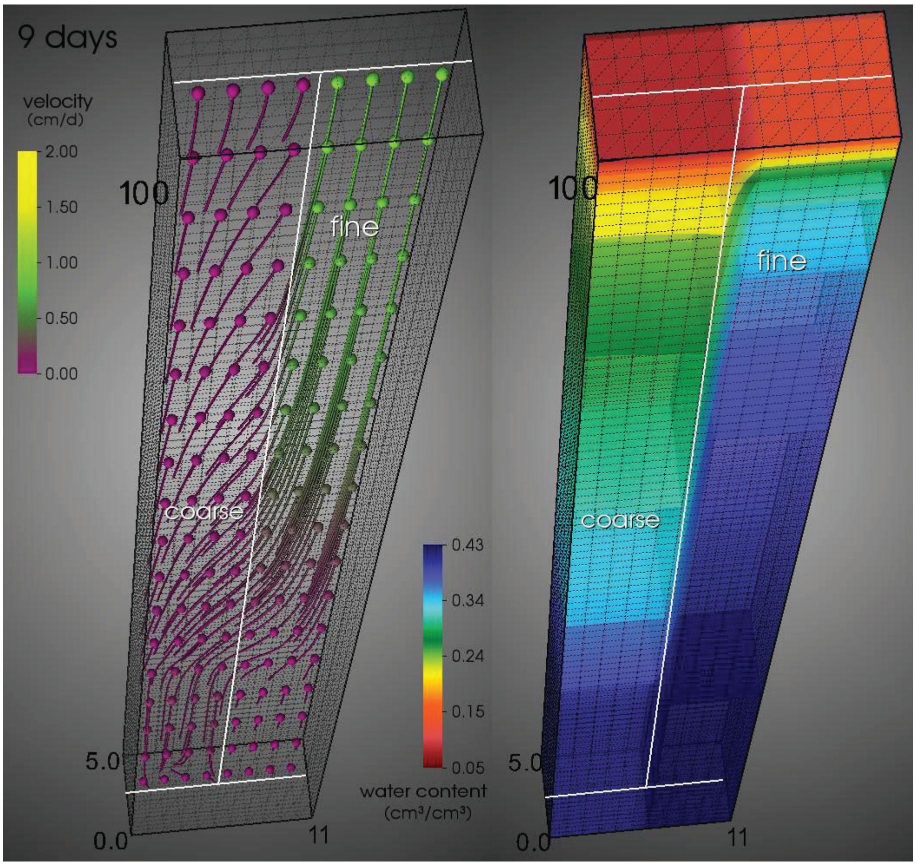

Figure 5.8: Water content and fluxes after 9 days of simulated evaporation in a soil column with two materials in vertical contact. Water movement is displayed by streamlines calculated from the vector field, with the streamline color indicating water fluxes within the soil column.

This flux serves as an additional water source for evaporation from the fine material and takes place in deeper regions of the soil column with ongoing evaporation. Hence, under equal meteorological conditions, horizontal water fluxes in the two-material soil column extend ST1 evaporation of the fine material from 4.5 to 6.2 days when compared to a uniform fine material soil column. In a study by Lehmann & Or (2009) these fluxes have been verified in a laboratory setup. According to Lehmann & Or (2009), this mechanism of water extraction from the coarse material may exceed several meters. Consequently, in natural soils with spatially different soils in vertical (or near vertical) contact with each other, water may be extracted from deeper areas within the coarser soil by horizontal water fluxes acting as a water resource for the finer soil.

B) Heat fluxes

For both systems, uniform and two-material soil, short wave radiation input from the upper boundary remains constant over the simulation period. However, if the coarse part within the two-material soil column reaches ST2 evaporation, incoming energy is no longer consumed at the soil surface. A temperature gradient between coarse and fine material, which is still in ST1, (Figure 5.5) develops and causes horizontal heat fluxes, transporting energy from the warmer coarse to the cooler fine material. This increases the energy available for evaporation from the fine soil. As a consequence, the constant potential ST1 evaporation rate in the fine soil increases, when the soil is in mixed stage evaporation rate.

Actual evaporation is driven by the vapor density gradient between soil and atmosphere reduced by the soil resistance (Eq. 5.1). Hence, if horizontal heat fluxes are responsible for increased evaporation rates, a direct dependency between evaporation rate and surface temperature must be verifiable: Monteith & Unsworth (2007) and Campbell (1977) define the saturated vapor density ρ_{sv} [kg m^{-3}] as an exponential function of the temperature

$$\rho_{sv} = 10^{-3} \frac{\exp\left(31.3716 - \frac{6014.79}{T} - 7.92495 \times 10^{-3} T\right)}{T} \qquad 5.5$$

and the actual vapor density ρ_a [kg m^{-3}] can be defined according to (Allen et al. 1998)

$$\rho_a = \frac{H_r}{100} \rho_{sv} \qquad 5.6$$

where T [K] is temperature and H_r [%] is the relative humidity.

To calculate the relative humidity of soil air $H_r soil$, the thermodynamic relationship postulated by Edlefsen and Anderson (1943) can be used:

$$H_r soil = \exp\left(\frac{hMg}{RT}\right) \qquad 5.7$$

Mixed stage evaporation in the two-material soil column lasts from day 2.7 to day

6.3. Evaporation rate during the mixed stage evaporation increases from ~0.98 to ~1.08 cmd^{-1}, or by approximately 10% (Figure 5.5). In the same period, temperature at the surface of the fine material increases from ~24.5°C to ~25.5°C. According to Eq. 5.1 and Eq. 5.5 to 5.7, this corresponds with an increased water vapor density gradient between soil and atmosphere of approximately 10% as well. As energy incoming from the boundaries remains constant over simulated time period, this indicates that horizontal heat fluxes result in the increased evaporation rate, thereby compensating for the reduced fine material surface.

The spatiotemporal evaporation along a profile in direction x (*x: 1 – 10; y = 1; z = 0*) can be seen in Figure 5.9. The whole profile, fine and coarse material, starts with a constant evaporation rate of ~0.98 cmd^{-1}, which is controlled by given meteorological conditions. As seen in Section A) in this chapter, water flows from coarse to fine material within the soil column. Flux directions (e.g Figure 5.6) cause the coarse material to dry out first in the domain farthest from the contact zone between both materials.

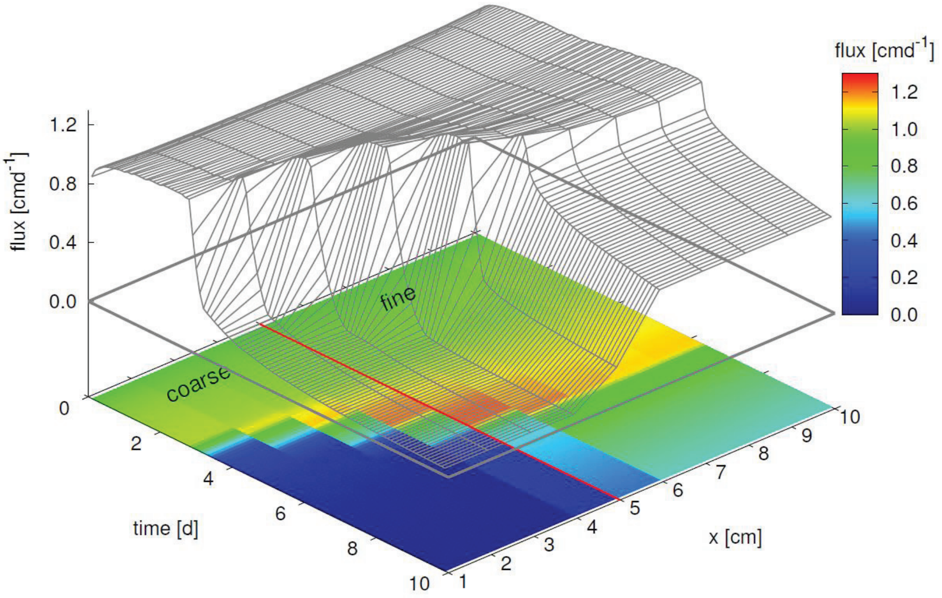

Figure 5.9: Temporal development of evaporation flux profile looking at the x-coordinate of the two-material soil column. The grey mesh gives the surface plot. A colored contour map is shown at the bottom. The red line in the contour plot parallel to the time [d] coordinate gives the contact region between fine (right) and coarse (left) material.

Accordingly, evaporation rate decreases around the $x = 1$ domain in the evaporation profile and soil temperature increases.

With the beginning of ST2 in parts of the coarse material, the surface flux exceeds the atmospherically demanded evaporation rate starting in the coarse material closer to the contact zone, which is still in ST1 evaporation. However, the strongest effect of horizontal fluxes can be seen in the fine material, where evaporation increases over the whole fine material part. Both mechanisms, horizontal water and heat fluxes, may be significant, because horizontal water fluxes into the finer material may sustain longer potential evaporation rates from the fine soil and horizontal heat fluxes increase the actual evaporation rate. Hence, evaporation rates may be wrongly estimated when assuming homogeneous soil surfaces and thereby neglecting horizontal flux mechanisms between different soil types.

5.4 Summary and conclusion

The effects of horizontal water and heat fluxes on soil evaporation from heterogeneous soils were analyzed in this section. A three-dimensional model was modified to feature coupled heat and water flow and an upper boundary condition solving the energy balance for every surface boundary node, thereby allowing the calculation of spatially variable evaporation rates and temperatures. Supporting the results of Shahraeeni & Or (2010), who performed laboratory experiments with vertically heterogeneous soils, modeling results show that combination of heat and water flux mechanisms characterize the evaporation behavior, when different soil materials are in direct vertical contact. Abe et al. (1995) present the evaporation drainage method, where highly water absorbing fabric material is inserted in a soil. Because of evaporation from the top of the fabric material, water constantly evaporates and is absorbed again, consequently drying the soil. Using different soil materials instead of fabric materials as proposed by Abe et al. (1995) may provide an ecological alternative for naturally controlled, sustainable drying of soils profitable for several disciplines such as civil and surface mining engineering.

Results of the present chapter can be summarized as follows:

a) Water fluxes within the modeling domain are directed from the coarse to the fine material and are caused by hydraulic pressure differences. These fluxes serve as a water source for the fine material, which consequently maintains a high evaporation rate for a longer time period when compared to a uniform fine material soil.

b) Heat fluxes are caused by different temperatures within the soil profile. With ongoing evaporation, the coarse material incrementally dries up and soil evaporation changes from ST1 to ST2. At this time, energy incoming from the upper boundary is no longer consumed at the soil surface, which consequently heats up. Because of this heating, a gradient in temperature develops and heat exchanges take place between cooler fine material, which is still in ST1 evaporation, and warmer coarse material. These heat fluxes increase the energy available for evaporation in the cooler material and the evaporation rate increases above an atmospherically demanded potential evaporation from a homogeneous soil surface.

c) Adding up both mechanisms shows that negligence of horizontal water and heat fluxes may lead to wrongly estimated evaporation rates, when dealing with vertically heterogeneous soil and representing them by effective parameters.

d) Numerical results presented in this study focus on a small scale of ~0.5 m^2 and an effect of horizontal fluxes on larger (plot or field) scales cannot be proven with this study. However, tillage, small scale textural, and/or structural variabilities in soils have a long history of attention (e.g. Peck et al., 1977; Cambardella et al., 1994; Vogel & Roth, 2003) and are causing preferential flow (Clothier et al., 2008) which is another controversial research area in soil sciences. Hence, heterogeneities and preferential flow in natural soils is rather rule than exception and questions regarding the importance of horizontal fluxes even at larger scales under natural field conditions need to be addressed.

e) As mentioned, water vapor influence on the presented results is negligible. Numerical restrictions and convergence problems did not allow for a model framework, which clearly demonstrated the effects of water vapor in the context of horizontal fluxes and their influence on evaporation. Further research about stability of the numerical implementation of coupled three-dimensional vapor, heat and liquid fluxes (under meteorological conditions) may be necessary.

f) For future research, a combination of laboratory, field, and numerical experiments may offer opportunities to gain a good understanding of compensated evaporation from heterogeneous soils. For these studies, a combination of different soils and the resulting effects on evaporation could be analyzed numerically and experimentally.

6 Summary and concluding remarks

6.1 Summary

The present work is part of the Sonderforschungsbereich *Transregio Collaborative Research Center 32: Patterns in Soil – Atmosphere – Vegetation Systems (SFB/TR32)*. This interdisciplinary research project focuses on interaction of energy, water, and carbon between the domains of soil, vegetation, and lower atmosphere and resulting patterns of state variables, which are highly variable in time and space. As mentioned domains are mostly studied separately from each other, a main goal for SFB/TR32 is the formulation and implementation of a complete modeling system, providing a mutual basis which considers essential feedback processes between the three compartments and thereby being able to monitor and simulate spatiotemporal development of structural, physical and chemical patterns. Focusing on the domain soil, water and temperature fluxes are important state variables significantly influencing vapor flux between soil and atmosphere. Soil surface water content and temperature patterns provide the lower boundary for atmospheric and the upper boundary for hydrologic problems, making the soil surface an important interface between both domains.

Because of the strong non-linearity of soil hydraulic properties, measureable soil water content and, directly linked by evaporation, temperature patterns develop even at relatively small scales of a few decimeters. This link between temperature and water content and the resulting formation of measureable patterns within soils makes consideration of coupled heat and water fluxes inevitable, when trying to simulate or predict the underlying processes.

Within this context, Chapter 2 gives the governing equations describing the difference between coupled and uncoupled modeling. Additionally, the implementation of an energy balance boundary condition and basics on infrared thermography (needed in Chapter 4) are discussed. Following the theoretical introduction, three different key aspects, discussed in the Chapters 3, 4 and 5 were subject of the present work:

In Chapter 3, the influence of neglecting thermal effects on instantaneous fluxes such as diurnal evaporation and on state variables such as surface temperature and water content is studied. Over a period of five days, evaporation, water content and temperature were calculated using a coupled and an uncoupled modeling approach Measured meteorological data were taken as upper boundary condition. Both models were run assuming wet and dry initial conditions. Results show that no difference between coupled an uncoupled approach can be seen, when assuming wet initial conditions. Isothermal liquid flux is shown to be the dominant flux component. In a dry soil, evaporation no longer takes place at the soil surface. Differences in actual evaporation rate in both model approaches resulted in relatively large differences in modeled surface temperatures. As evaporation no longer takes place at the soil surface, thermal and isothermal vapor fluxes gain importance. This is especially true for the region between the evaporative front and the soil surface. In this part of the soil, influence of vapor flux components has a significant effect on the total net water flux (as entirety of liquid water and vapor). Additionally, a statement about the usage of the enhancement factor is given. The enhancement factor is used to compensate differences between experimental measurement and theoretical prediction of water vapor diffusion in soils and, even though widely used, its necessity is subject to current research. By comparing the results of different model scenarios considering and neglecting the enhancement factor, it is concluded that actual studies need to be expanded in order to fully proof that the enhancement factor is obsolete if certain adjustment (such as film flow) is considered in numerical models.

In Chapter 4 the derivation of soil hydraulic properties from remote sensing methods, in particular from infrared measurements is studied. Focus is on the extend that is necessary to substantiate surface measurements with subsurface water content measurements in order to inversely estimate effective soil hydraulic properties. The spatiotemporal development of soil surface temperatures (SST) depends on water availability in the near-surface soil layer. Since the soil loses latent heat during evaporation and water available for evaporation depends on soil hydraulic properties (SHP), the temporal variability of SST should contain information about the near-surface SHP. The objective of this chapter was to investigate the uncertainties of SHP derived from SST. HYDRUS-1D coupled with a global optimizer (DREAM) was used to inversely estimate van Genuchten-Mualem parameters from infra-red measured SST and TDR-measured water contents. This approach was tested using synthetic and real data, collected during September 2008 from a harrowed silty-loam field plot in Selhausen, Germany. The synthetic data illustrated that SHP can be derived from SST and that additional soil water content measurements reduce the uncertainty of estimated SHP. Unlike for the synthetic experiment with a vertically homogeneous soil profile, a layered soil profile had to be assumed to derive SHP from the real data. Therefore, the uncertainty of SHP derived from real data was considerably larger. Water retention curves of undisturbed soil cores were similar to those estimated from SST and TDR data for the deeper undisturbed soil. The retention curves derived from SST and TDR data for the harrowed top soil layer were typical for a coarse textured soil and deviated considerably from the retention curves of soil cores, which were typical for a fine textured soil and similar to those from the subsoil.

Chapter 5 investigates whether a fully coupled, three-dimensional model can represent spatial patterns caused by interactions in evaporation and temperature consistently with recent experimental results. To allow a for a spatial distribution of evaporation rates depending on the boundary node specific temperature and water content, the model was modified to allow the solution of an energy balance boundary condition for every single upper boundary node exposed to atmospheric conditions. A soil column with dimensions of 11 cm x 5 cm x 100 cm (in x, y, z direction respectively) and a uniform resolution of 1 cm in every direction was used as modeling domain. One part of the soil column was characterized by hydraulic properties for a fine soil, the other part with hydraulic properties of a coarse soil. This results in a soil column with two different soil materials in direct vertical contact. Constant meteorological conditions representing laboratory conditions were. Results from a ten day simulation period show that this arrangement of soil materials causes vertical (and horizontal) heat and water fluxes between both soils. Based on the hydraulic gradient, general water flux is directed from coarse to fine material. Consequently, the coarse material dries faster when compared to a uniform coarse soil. Due to different water contents in coarse and fine material, temperature differences are increasing. This leads to heat fluxes from coarse to fine material and as a consequence, evaporation rates in the fine material are higher than the atmospherically demanded potential evaporation from a uniform fine soil material. Hence, negligence of horizontal heat and water fluxes may lead to wrongly estimated evaporation rates, when dealing with vertically heterogeneous soils and representing them by effective parameters.

6.2 Concluding remarks

Research documented with the present work was conducted within the framework of the first research phase of Sonderforschungsbereich *Transregio Collaborative Research Center 32: Patterns in Soil – Atmosphere – Vegetation Systems (SFB/TR32)*. Classified in the soil domain with scale range from decimeter to plot scale, the main focus of this work is on different aspects of experimental and numerical modeling tools needed for the development a multi-scale soil – vegetation – atmosphere modeling system and the involved complex feedback mechanisms and scaling problems. Coming back to the initial key aspects of research in this work, some important statements and their meaning and/or research potential as well as open questions for the next project periods will be discussed below.

As shown in Chapter 3, coupled thermal fluxes in dry soils have an impact on the modeled diurnal development of soil surface state variables. When trying to combine models from the domains soil and atmosphere under the constraints of a high (~hourly) temporal resolution, the negligence of coupled thermal fluxes may lead to error-prone boundary conditions for both, hydrological and meteorological model. As a consequence, feedback mechanisms between both domains are erroneous. However, no effect of thermal fluxes was observed in wet soil. Calculations considering vapor and thermal gradients as coupling mechanism have increased numerical complexity and higher computation times. Additionally, constraints for a stable numerical solution are stronger. Therefore in the following research phases, the effort of incorporating effects of water vapor on soil state variables should not focus on a process-based consideration in general. A better approach when trying to combine models at different scales is the development of correlation factors or functions effectively considering the impact of coupled thermal fluxes as a function of temperature and water content. Doing this, the process-based coupled model can be used to validate proposed correlation factors (or functions).

In Chapter 4, it was shown that the temporal development of soil surface temperatures (measured by a ground-based infrared camera) contains information about soil hydraulic properties. However, without supporting TDR measurements, uncertainty of estimated properties was high. As installation of TDR probes over large areas is costly and time-consuming, possible combinations of remote sensing methods should be investigated.

Furthermore, the question of scaling is mentioned in Chapter 4. Usually, when trying to transfer data from process-based hydrologic models to larger scaled meteorological models, upscaling methods are needed to compensate for the loss of spatial variability. The other way round, downscaling also needs to be taken in mind. When downscaling meteorological state variables needed as upper boundary condition for hydrologic models, information about the spatiotemporal variabilities of hydrologic state variable is necessary. Therefore, further research should focus on the definition of downscaling transfer functions. In this context, Chapter 4 shows that infrared soil surface temperature observation is a useful tool, because it contains information about soil surface temperature, water content and, as an imaging measurement technique, about state variable patterns.

Additionally, it should be investigated to what extent soil surface temperature measurements are linked to the soil's structure and its micro-relief (Figure 6.1). Field experiments in Chapter 4 were performed under the constraints of a uniformly prepared research field plot. Consequently, the human management of soil, which is directly related to the soil structure and the resulting impact on soil hydraulic properties could not be investigated. However, the scale ranges studied by Project 4 correspond with the scale relevant to coupled heat and water fluxes and with the scale at which humans directly take influence on the soil's structure (e.g. by grubbing, harrowing or ploughing). Thus, following research in Project B should take different kinds of land use and its effect on soil hydraulic properties and patterns into consideration. Also the effect of soil tillage on inversely estimated soil hydraulic properties could be studied.

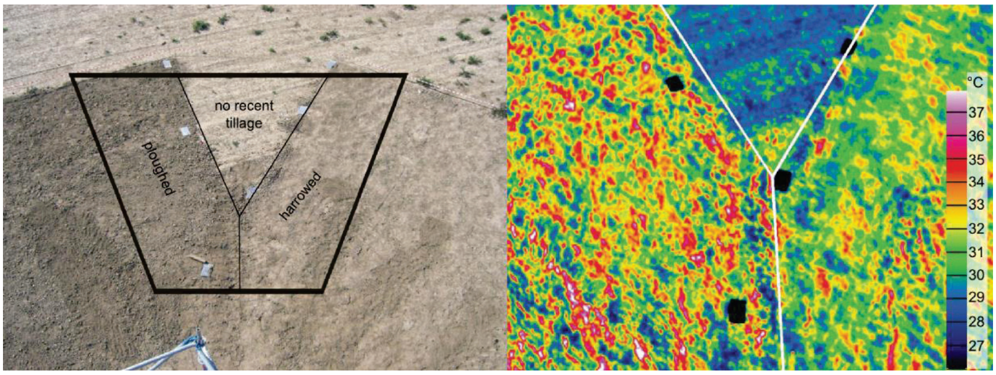

Figure 6.1: Photograph and imaging infrared measurement taken during the preparation of a field experiment in Selhausen, Germany in September 2009. Differing soil surface temperatures and temperature patterns can be seen for different soil tillage.

Results in Chapter 5 show that three-dimensional heat and water fluxes in vertically heterogeneous soils have a considerable on the evaporative behavior of heterogeneous soils. Because three-dimensional simulations come at a very high computational cost, usage of small scale process-based 3D-models within a multiscale modeling system is not an option. However, it could be shown in Chapter 5 that developing spatial patterns at the soil surface cause subsurface redistributions of important state variables such as temperature and water content. In the next research period, the scale at which these lateral redistributions can be neglected needs to investigated. If the spatial extend of lateral redistribution is known, one dimensional stream tube models representing the variability of properties on a scale larger than the scale of lateral redistribution are an alternative to represent the effect of spatial heterogeneity.

References

Abe, Y., J. Tsurui, T. Yamaguchi, Y. Ohtsuka and H. Ii. 1995. Evaporation of a salt capturing stick and its influence on solution and solute in soil. J. of Arid Land Studies 5: 43 – 54.

Akinyemi, O.D. & N. Mendes. 2007. Numerical and experimental determination of surface temperature and moisture evolution in a field soil. J. Geophys. Eng. 4: 7 – 17.

Allen, R.G., L.S. Pereira, D. Raes and M. Smith. 1998. Crop evapotranspiration: Guidelines for computing crop water requirements. FAO Irrig. Drain. Pap. 56. FAO, Rome.

Arnfield, A. J. . 2003. Two decades of urban climate research: A review of turbulence, exchanges of energy and water, and urban heat islands. Int. J. Climatol. 23: 1 – 26.

Asaeda, T. and V. T. Ca. 1993. The subsurface transport of heat and moisture and its effect on the environment: A numerical model. Bound-Lay Meteorol 65: 159 – 179.

Bach, L. B. . 1992. Soil water movement in response to temperature gradients: Experimental measurements and model evaluation. Soil Sci. Soc. Am. J. 56: 37 – 46.

Battistelli., A., Calore, C., Pruess, K. 1997. The simulator TOUGH2/EWASG for modelling geothermal reservoirs with brines and non-condensible gas. Geothermics 26: 437 – 464.

Bauer, J., M. Herbst, J. A. Huisman, L. Weihermüller and H. Vereecken. 2008. Sensitivity of simulated soil heterotrophic respiration to temperature and moisture reduction functions. Geoderma 145: 17 – 27.

Bear, J.. 1972. Dynamics of fluids in porous media. Dover Publications, Inc., New York, 764 pp.

Ben-Asher, J., A . D. Matthias and A. W. Warrick. 1983. Assessment of evaporation from bare soil by infrared thermometry. Soil Sci. Soc. Am. J. 47: 185 – 191.

Bogena, H., K. Schulz and H. Vereecken. 2006. Towards a Network of Observations in Terrestrial Environmental Research. Advances in Geosciences 9: 109 – 114.

Burke, E. J., R. J. Gurney, L. P. Simmonds, T. J. Jackson. 1997. Calibrating a soil water and energy budget model with remotely sensed data to obtain quantitative information about the soil. Wat. Resourc Res. 33: 1689 – 1697.

Burke, E. J., R. J. Gurney, L. P. Simmonds and P. E. O'Neill. 1998. Using a modelling approach to predict soil hydraulic properties from passive microwave measurements. IEEE Trans. Geosci. Remote Sensing 36: 454 – 462.

Bittelli, M., F. Ventura, G. S. Campbell, L. R. Snyder, F. Gallegati, P. R. Pisa. 2008. Coupling of heat, water vapor and liquid water fluxes to compute evaporation in bare soils. J. Hydrol. 362: 191 – 205.

Cahill. A. T. and M. B. Parlange. 1998. On water vapor transport in field soils. Wat. Resour. Res 34: 731 – 739.

Cambardella, C.A., T. B. Moorman, J. M. Novak, T. B. Parkin, D. L. Karlen, R. F. Turco, and A. E. Konopka, . 1994. Field.scale variability of soil properties in central Iowa soils. Soil Sci. Soc. Am. J. 58: 1501 – 1511.

Camillo, P. J., R. J. Gurney and T. J. Schmugge. 1983. A soil and atmospheric boundary layer model for evaporation and soil moisture studies. Wat. Resour. Res 19: 371 – 380.

Camillo, P. J. and R. J. Gurney. 1986. A resistance parameter for bare soil evaporation models. Soil Sci. 141: 95 – 105.

Camillo, P. J., P. E. O'Neill and R. J. Gurney. 1986. Estimating soil hydraulic parameters using passive microwave data. IEEE Trans. Geosci. Remote Sensing. GE-24: 930 – 936.

Campbell, G. S. . 1985. Soil physics with BASIC. Developments in soil sciences: 14. 150 pp. Elsevier, Amsterdam, The Netherlands.

Cary, J. W. . 1979. Soil heat transducers and water vapor flow. Soil. Sci. Soc. Am. J. 43: 835 – 839.

Cass, A., G. S. Campbell, and T. L. Jones. 1984. Enhancement of thermal water vapor diffusion in soils. Soil Sci. Soc. Am. J. 48: 25-32.

Chanzy, A., L. Bruckler and A. Perrier. 1995. Soil evaporation monitoring - a possible synergism of microwave and infrared remote-sensing. J. of Hydrol. 165:235 – 259.

Chung, S.-O. and R. Horton. 1987. Soil heat and water flow with a partial surface mulch. Wat. Resour. Res. 23: 2175 – 2186.

Clothier, B. E., S. R. Green and M. Deurer. 2008. Preferential flow and transport in soil: Progress and prognosis. Eur. J. Soil Sci.. 59: 2 – 13.

Dane, J. H. and G. C. Topp (ed.). 2002. Methods of soil analysis: Part 4 – Physical methods. SSSA book series 5. 1692 pp.

Das, N. N., and B. P. Mohanty. 2006. Root zone soil moisture assessment using remote sensing and vadose zone modeling. Vadose Zone J. 5:296-307.

de Marsily, G. . 1986. Quantitative hydrogeology. Academic Press, London, UK

de Vries, D. A. . 1975. Heat transfer in soils. In heat and mass transfer in the biosphere. p. 5 – 28. Scripta Book, Washington D. C.

Demarty, J., C. Ottle, J. Braud, A. Olioso, J. P. Frangi, H. V. Gupta, L. A. Bastidas. 2005. Constraining a physically based soil-vegetation-atmosphere transfer model with surface water content and thermal infrared brightness temperature measurements using a multiobjective approach. Wat. Resour. Res 41, doi:10.1029/2004WR003695.

Diao, N., Q. Li and Z. Fang. 2004. Heat transfer in ground heat exchangers with groundwater advection. Int. J. Therm Sci. 43: 1203 – 1211.

Duan, Q., V. K. Gupta, and S. Sorooshian. 1992. A shuffled complex evolution approach for effective and efficient global minimization. J. Optim. Theory Appl. 76: 501 – 521.

Edlefsen, N. E. and A. B. C. Anderson. 1943. The thermodynamics of soil moisture. Hilgardia 16: 31 – 299.

Farnworth, B. . 1986. A numerical model of combined diffusion of heat and water vapor through clothing. Textile Research Journal 56: 653 – 665.

Faust, C. R. and J. W. Mercer 1979. Geothermal reservoir simulation 1. Matematical models for liquid- and vapor-dominated hydrothermal systems, Wat. Resour. Res. 15: 23 – 30.

Friedel, M. J. . 2005. Coupled inverse modeling of vadose zone water, heat, and solute transport: calibration constraints, parameter nonuniqueness, and predictive uncertainty. J. Hydrol. 312: 148 – 175.

Gaussorgues, G. and S. Chomet. 1994. Infrared thermography. Chapman & Hall, London, UK, 508 pp.

García-Navarro, P. and E. Playán (eds). 2008. Numerical modelling of hydrodynamics for water resources. Taylor & Francis Group, London, UK, 402 pp.

Goss, K.-U. and M. Madlinger. 2007. Estimation of water transport based on in situ measurements of relative humidity and temperature in a dry Tanzanian soil. Wat. Resour. Res 43, doi:10.1029/2006WR005197.

Grifoll, J., J. M. Gastó and Y. Cohen. 2005. Nonisothermal soil water transport and evaporation. Adv. Water Resour. 28: 1254 – 1266.

Hanks, R. J., H. R. Gardner, and J.T. Hutton. 1967. Evaporation of water from soils as influenced by drying with wind or radiation. Soil Sci. Soc. Am. Proc. 31: 593 – 598.

Herbst, M., N. Prolingheuer, A. Graf, J. A. Huisman, L. Weihermüller and J. Vanderborght. 2009. Characterization and understanding of bare soil respiration spatial variability at plot scale. Vadose Zone J. 8: 762 – 771.

Ho, C. K. and S. W. Webb. 1998. Review of porous media enhanced vapor-diffusion mechanisms, models, and data – Does enhanced vapor-phase diffusion exist? J. Porous Media 1: 71 – 92.

Hopmans, J. W., J. Šimůnek and K. L. Bristow. 2002. Indirect estimation of soil thermal properties and water flux using heat pulse probe measurement: Geometry and and dispersion effects. Wat. Resour. Res. 38 (1), doi: 10.1029/2000WR000071.

Jackson, R. D., B. A. Kimball, R. J. Reginato, and F. S. Nakayama. 1973a. Diurnal soil-water evaporation: Time-depth-flux patterns. Soil Sci. Soc. Am. Proc. 37: 505 – 509.

Jackson, R. D., R. J. Reginato, B. A. Kimball, and F. S. Nakayama. 1973b. Diurnal soil-water evaporation: Comparison of measured and calculated soil-water fluxes. Soil Sci. Soc. Am. Proc. 38: 861 – 866.

Jhorar, R.K., W.G.M. Bastiaanssen, R. A. Feddes, J. C. Van Dam. 2002. Inversely estimating soil hydraulic functions using evapotranspiration fluxes. J. Hydrol. 258:198-213.

Jury, W. A. and R. Horton. 2004. Soil physics. John Wiley & Sons, New Jersey, 6th edition, 384 pp.

Jury, W. A. and J. Letey. 1979. Water vapor movement in soils: Reconciliation of theory and experiment. Soil Sci. Soc. Am. J. 43: 823 – 827.

Kalma, J. D., T. R. McVicar and M. F. McCabe. 2008. Estimating land surface evaporation: A review of methods using remotely sensed surface temperature data. Surv. Geophys. 29: 421 – 469.

Kondo, J., N. Saigusa and T. Sato. 1990. A parameterization of evaporation from bare soil surfaces. J. Appl. Meteor. 29:385 – 389.

Lehmann, P., S. Assouline, and D. Or. 2008. Characteristic lengths affecting evaporative drying of porous media. Phys. Rev. E. 77. 056309, doi:10.1103/PhysRevE.77.056309.

Lehmann, P. and D. Or. 2009. Evaporation and capillary coupling across vertical textural contrasts in porous media. Phys. Rev. E. 80. 046318, doi:10.1103/PhysRevE.80.046318

Mapa, R. B., R. E. Green and L. Santo. 1986. Temporal variability of soil hydraulic properties with wetting and drying subsequent to tillage. Soil Sci. Soc. Am. J. 50: 1133 – 1138.

Millington, R. J. and J. P. Quirk. 1961. Permeability of porous media. Trans. Faraday

Soc. 57: 1200 – 1207.

Milly, P. C. D. . 1982. Moisture and heat transport in hysteretic, inhomogeneous, porous media: A matric head-based formulation and a numerical model. Wat. Resour. Res 18: 489 – 498.

Milly, P. C. D. . 1984. A simulation analysis of thermal effects on evaporation from soil. Wat. Resour. Res. 20: 1087 – 1098.

Monteith, J. L and M. Unsworth. 2007. Principles of environmental physics. 440 pp. Elsevier, USA.

Moran, M. S., A. F. Rahman, J. C. Washburne, D. C. Goodrich, M. A. Weltz and W. P. Kustas. 1996. Combining the Penman-Monteith equation with measurements of surface temperature and reflectance to estimate evaporation rates of semiarid grasslands. Agric. For. Meteorol. 80: 87 – 109.

Murphy, B. W., T. B. Koen, B. A. Jones, L. M. Huxedurp. 1993. Temporal variation of hydraulic properties for some soils with fragile structure. Australian Journal of Soil Research 31: 179 – 197.

Nassar, I.N. and R. Horton. 1989. Water transport in unsaturated nonisothermal salty soils: II. Theoretical development. Soil Sci. Soc. Am. J. 53: 1330 – 1337.

Nassar, I.N. and R. Horton. 1992. Simultaneous transfer of heat, water and solute in porous media: I. Theoretical development. Soil Sci. Soc. Am. J. 56: 1350 – 1356.

Nimmo, J. R. and E. E. Miller. 1986. The temperature dependence of isothermal moisture vs. potential characteristics in soils. Soil Sci. Soc. Am. J. 50: 1105 – 1113.

Noborio, K., K .J. McInnes and J. L. Heilmann. 1996b. Two-dimensional model for water, heat and solute transport in furrow-irrigated soil. II. Field evaluation. Soil Sci. Soc. Am. J. 60: 1010 – 1021.

Miyazaki, T. 1976. Condensation and movement of water vapor in sand under temperature gradient. (Japanese) Trans. Jpn. Soc. Irrig. Drain.Rural Eng. 61: 1 – 8.

Mualem, Y. 1976. A new model for predicting the hydraulic conductivity of unsaturated porous media. Wat. Resour. Res 12: 513 – 521.

Olioso, A., O. Taconet and M.B. Mehrez. 1996. Estimation of Heat and Mass Fluxes from IR brightness temperature. IEEE Trans. Geosci. Remote Sensing 34: 1184 – 1190.

Olioso, A., H. Chauki, D. Courault, and J.-P. Wigneron, 1999. Estimation of evapotranspiration and photosynthesis by assimilation of remote sensing data into SVAT models. Remote Sens. Environ. 68:341-356.

Osunbitan, J. A., D. J. Oyedele and K. O. Adekalu. 2005. Tillage effects on bulk density, hydraulic conductivity and strength of a loamy sand soil in southwestern Nigeria. Soil and Tillage Research 82: 57 – 64.

Parlange, M. B., A. T. Cahill, D. R. Nielsen, J. W. Hopmans, O. Wendroth. 1998. Review of heat and water movement in field soils. Soil and Tillage Research 47: 5 – 10.

Peck, A. J., R. J. Luxmore and J. L. Stolzy. 1977. Effects of spatial variability in soil hydraulic properties in water budget modeling. Water Resour. Res. 13: 348 – 354.

Philip, J. R. 1957. Evaporation, and moisture and heat fields in the soil. J. Meteor. 14: 354 – 366.

Philip, J. R. and D. A. de Vries. 1957. Moisture movement in porous materials under temperature gradient. Trans. Amer. geophys. Union 38: 222 – 232.

Rose, C. W. 1968a. Water transport in soil with a daily temperature wave. I. Theory and experiment. Aust. J. Soil Res. 6: 32 – 44.

Rose, C. W. 1968b. Water transport in soil with a daily temperature wave. II. Analysis. Aust. J. Soil Res. 6: 45 – 57.

Rosenbaum, U., J. A. Huisman, J. Vrba, H. Vereecken, H. R. Bogena. 2011. Correction of temperature and electrical conductivity effects on dielectric permittivity measurements with ECH2O sensors. Vadose Zone J. 10: 582 – 593.

Saito, H., J. Šimůnek and B. P. Mohanty. 2006. Numerical analysis of coupled water, vapor and heat transport in the vadose zone. Vadose Zone J. 5: 784 – 800.

Sakai, M., N. Toride, and J. Šimůnek. 2009. Water and vapor movement with condensation and evaporation in a sandy column. Soil Sci. Soc. Am. J. 73: 707 – 717.

Seetharam, S. C., H. R. Thomas, and P. J. Cleall. 2007. Coupled thermo/hydro/chemical/mechanical model for unsaturated soils – Numerical algorithm. Int. J. Numer. Meth. Engng 70: 1480 – 1511.

Scanlon, B. R. and P. C. D. Milly. 1994. Water and heat fluxes in desert soils: 2. Numerical simulations. Water Resour. Res. 30: 721 – 733.

Scanlon, B., K. Keese, R. C. Reedy, J. Šimůnek, and B. Andraski. 2003. Variations in flow and transport in thick desert vadose zones in response to paleoclimatic forcing (0 – 90 kyr): Monitoring, modeling, and uncertainties. Wat. Resour. Res 39, doi:10.1029/2002WR001604.

Scharnagl, B., J.A. Vrugt, H. Vereecken, and M. Herbst. 2010. Information content of incubation experiments for inverse estimation of pools in the rothamsted carbon model: A bayesian perspective. Biogeosciences 7:763-776.

Shahraeeni, E. and D. Or. 2010. Thermo-evaporative fluxes from heterogeneous porous surfaces resolved by infrared thermography.. Wat. Res. Resour. 46. W09511, doi:10.1029/2009WR008455.

Shokri, N., P. Lehmann and D. Or. 2009. Critical evaluation of enhancement factors for vapor transport through unsaturated porous media. Wat. Res. Resour. 45. W10433, doi:10.1029/2009WR007769.

Shokri, N., P. Lehmann, P. Vontobel, D. Or. 2008. Drying front and water content dynamics during evaporation from sand delineated by neutron radiography. Wat. Resour. Res 44, doi: 10.1029/2007WR006385.

Šimůnek, J. and D. L. Suarez. 1993. UNSATCHEM-2D code for simulating two dimensional variably saturated water flow, heat transport, carbon dioxide production and transport, and multicomponent solute transport with major ion equilibrium and kinetic chemistry. Version 1.1, Research Report No. 128, U.S. Salinity Laboratory, USDA, ARS, Riverside, CA.

Šimůnek, J., J. M. H. Hendrickx and B. Borchers. 2001. Modeling transient temperature distributions around landmines in homogeneous bare soils. *In* A. C. Dubey et al. (ed), Proc. Detection and Remediation Technologies for Mines and Minelike Targets. Vol 4394: 387 – 397, Bellingham, WA.

Šimůnek, J., M.Th. van Genuchten and M. Šejna. 2005. The HYDRUS-1D software package for simulating the one-dimensional movement of water, heat, and multiple solutes in variably-saturated media. Version 3.0, HYDRUS Software Series 1, Department of Environmental Sciences, University of California Riverside, Riverside, CA, 270 pp.

Šimůnek, J., M.Th. van Genuchten and M. Šejna. 2006. The HYDRUS software package for simulating the two- and three-dimensional movement of water, heat, and multiple solutes in variably-saturated media. Technical Manual. Version 1.0, HYDRUS Software Series 1, Department of Environmental Sciences, University of California Riverside, Riverside, CA, 241 pp.

Šimůnek, J., M. Th. van Genuchten, and M. Šejna. 2008. Development and applications of the HYDRUS and STANMOD software packages, and related codes, Vadose Zone J., Special Issue “Vadose Zone Modeling”, 7(2): 587 – 600. doi:10.2136/VZJ2007.0077

Sophocleous, M. 1979. Analysis of water and heat flow in unsaturated-saturated porous media. Wat. Resour. Res 15: 1195-1206.

Steenpass C., J. Vanderborght, M. Herbst, J. Šimůnek and H. Vereecken (2010). Estimating soil hydraulic properties from infrared measurements of soil surface temperatures and TDR data. Vadose Zone J. 9: 910 – 924.]

Talloen, J. 2009. Comparison of measured soil surface temperatures and bare soil evaporation rates with simulations by the coupled water and energy transport model HYDRUS 1-D. Master Thesis, Faculty of Bioscience Engineering, K.U.Leuven, Belgium, 58p.

Topp, G.C., J.L. Davis and A.P. Annan. 1980. Electromagnetic determination of soil water content: measurement in coaxial transmission lines. Wat. Res. Resourc. 16: 574-582

van Bavel, C. H. M. and D. I. Hillel. 1976. Calculating potential and actual evaporation from a bare soil surface by simulation of concurrent flow of water and heat. Agric. For. Meteorol. 17: 453 – 476.

Vanderborght, J., A. Graf, C. Steenpass, B. Scharnagl, N. Prolingheuer, M., H.-J. Hendricks Franssen,and H. Vereecken. 2010. Effect of within-field variability on the variability of bare soil evaporation: comparison of eddy covariance measurements with potential and actual evaporation calculations. Vadose Zone J. 9: 943 – 954.

van de Griend, A. and M. Owe. 1994. Bare soil surface resistance to evaporation by vapor diffusion under semiarid conditions. Water Resour. Res. 30: 181 – 188.

van Genuchten, M.T. . 1980. A closed-form equation for predicting the hydraulic conductivity of unsaturated soils. Soil Sci. Soc. Am. J. 44: 892 – 898.

Vereecken, H., J. A. Huisman, H. Bogena, J. Vanderborght, J. A. Vrugt, and J. W. Hopmans. 2008. On the value of soil moisture measurements in vadose zone hydrology: A review. Wat. Resour. Res., 44, doi:10.1029/2008WR006829.

Vogel H.-J. and K. Roth. 2003. Moving through scales of flow and transport in soil. J. Hydrol. 272: 95 – 106.

Vrugt, J., H. V. Gupta, W. Bouten, S. Sorooshian. 2003. A Shuffled Complex Evolution Metropolis algorithm for optimization and uncertainty assessment of hydrologic model parameters. Wat. Resour. Res 39(8), doi:10.1029/2002WR001642.

Vrugt, J., C. J. F. ter Braak, M. P. Clark, J. M. Hyman, B. A. Robinson. 2008a. Treatment of input uncertainty in hydrologic modeling: Doing hydrology backward with Markov chain Monte Carlo simulation. Wat. Resour. Res. 44, doi: 10.1029/2007WR006720.

Vrugt, J., C. J. F. ter Braak, H. V. Gupta, B. A. Robinson. 2008b. Equifinality in formal (DREAM) and informal (GLUE) bayesian approaches in hydrologic modeling? Stochastic Environ. Res. Risk Assess. 23(7), doi: 10.1007/s00477-008-0274-y.

Yang, K., T. Koike, B. Ye, L. Bastidas. 2005. Inverse analysis of the role of soil vertical heterogeneity in controlling surface soil state and energy partition. J. Geophys. Res.: 110. 15 pp.

Yiotis, A. G., A. K. Stubos, A. G. Boudouvis, I. N. Tsimpanogiannis, and Y. C. Yortos. 2005. Pore-network modeling of isothermal drying in porous media. Transp. Porous Media 58: 63 – 86.

Abstract

The present work is part of the Sonderforschungsbereich Transregio Collaborative Research Center 32 (SFB/TR32). This interdisciplinary research project focuses on interaction of energy, water, and carbon between the domains of soil, vegetation, and lower atmosphere and resulting patterns of state variables. Soil surface water content and temperature patterns provide the lower boundary for atmospheric and the upper boundary for hydrologic problems, making the soil surface an important interface between both domains. Because of the strong non-linearity of soil hydraulic properties (SHP), measureable soil water content and, directly linked by evaporation, temperature patterns develop even at relatively small scales of a few decimeters. This link between temperature and water content and the resulting formation of measureable patterns within soils makes consideration of coupled heat and water fluxes inevitable when trying to simulate or predict underlying processes. The present work was conducted in the first research period of SFB TR 32 and focus was on near surface fluxes and patterns in bare soils. Within this context, the present thesis consists of three key objectives:

First, the influence of neglecting thermal effects on instantaneous fluxes such as diurnal evaporation and on state variables such as surface temperature and water content is studied. Over a period of five days, evaporation, water content and temperature were calculated using a coupled and an uncoupled modeling approach. Measured meteorological data were taken as upper boundary condition. Both models were run assuming wet and dry initial conditions. Results show that with wet initial conditions, differences between coupled and uncoupled approach are negligible. In a dry soil, differences in actual evaporation rate in both model approaches resulted in relatively large differences in modeled soil surface temperatures (SST). In the upper part of the soil, influence of thermal and isothermal vapor flux components has a significant effect on the total net water flux (as entirety of liquid water and vapor). Furthermore, the enhancement factor (Cass et al. 1984) used to compensate differences between experimental measurement and theoretical prediction of water vapor diffusion in soils is studied. Even though widely used, its necessity is subject to current research. By comparing the results of different model scenarios considering and neglecting the enhancement factor, it is concluded that actual studies need to be expanded in order to fully proof that the enhancement factor is obsolete if certain adjustments (such as film flow) are considered in numerical models.

Secondly, the derivation of SHP from infrared temperature measurements is studied. The spatiotemporal development of SST depends on water availability in the near-surface soil layer. Since the soil loses latent heat during evaporation and water available for evaporation depends on soil hydraulic properties, the temporal variability of SST should contain information about the near-surface SHP. HYDRUS-1D coupled with a global optimizer (DREAM) was used to inversely estimate van Genuchten-Mualem parameters from infra-red measured SST and TDR-measured water contents. This approach was tested using synthetic and real data, collected from a harrowed silty-loam field plot in Selhausen, Germany. The synthetic data illustrated that SHP can be derived from SST and that additional soil water content measurements reduce the uncertainty of estimated SHP. Unlike for the synthetic experiment with a vertically homogeneous soil profile, a layered soil profile had to be assumed to derive SHP from the real data. Therefore, the uncertainty of SHP derived from real data was considerably larger. Water retention curves of undisturbed soil cores were similar to those inversely estimated for the deeper undisturbed soil. The retention curves derived from SST and TDR data for the harrowed top soil layer were typical for a coarse textured soil and deviated considerably from the retention curves of soil cores, which were typical for a fine textured soil and similar to those from the subsoil.

Lastly, a mechanistic model was used to study the effects of three-dimensional heat and water fluxes on spatially distributed evaporation rates. To allow for a spatial distribution of evaporation rates depending on the boundary node specific temperature and water content, the model was modified to allow the solution of an energy balance boundary condition for every single upper boundary node exposed to atmospheric conditions. A soil column with dimensions of 11 cm x 5 cm x 100 cm (in x, y, z direction respectively) and a uniform resolution of 1 cm in every direction was used as modeling domain. One part of the soil column was characterized by SHP for a fine soil, the other part with SHP of a coarse soil, leading to a soil column with two different soil materials in direct vertical contact. Modeling results of the two-material soil column were compared to results from a uniformly coarse and a uniformly fine soil. Constant meteorological conditions representing laboratory conditions were chosen. Results show, that based on the hydraulic gradient, net water flux is directed from coarse to fine material. Consequently, the coarse material dries faster when compared to a uniform coarse soil. Due to different water contents in coarse and fine material, temperature differences are increasing. This leads to heat fluxes from coarse to fine material and as a consequence, evaporation rates in the fine material are higher than the atmospherically demanded potential evaporation from a uniform fine soil material. Hence, negligence of horizontal heat and water fluxes may lead to wrongly estimated evaporation rates, when dealing with vertically heterogeneous soils and representing them by effective parameters.

Kurzfassung

Die vorliegende Arbeit ist Teil des interdisziplinären Soderforschungsbereichs SFB TR32, welcher die Interaktion von Energie, Wasser und Kohlenstoff in Boden, Vegetation und Atmosphäre untersucht. Hierbei kommt der Bodenoberfläche eine besondere Bedeutung zu, da oberflächliche/r Wassergehalt und Temperatur die untere Randbedingung für meteorologische und die obere Randbedingung hydrologische Modelle maßgeblich beeinflussen. Schon auf kleinen Skalen von wenigen Dezimetern Fläche entwickeln sich aufgrund nichtlinearer bodenhydraulischer Eigenschaften messbare Muster in Wassergehalt und Temperatur, welche über die Evaporation direkt verknüpft sind. Diese Verbindung zwischen Temperatur und Wassergehalt und die daraus resultierende Bildung von messbaren Mustern an der Bodenoberfläche machen eine Berücksichtigung gekoppelter Wärme- und Wasserflüsse unabdingbar. Die vorliegende Arbeit wurde in der ersten Förderperiode des SFB TR 32 durchgeführt, in der der Schwerpunkt auf oberflächennahen Flüssen und Mustern in unbewachsenen Böden lag. In diesem Zusammenhang wird die vorliegende Arbeit von drei unterschiedlichen Fragestellungen aufgebaut:

Zuerst wird der Einfluss der Nichtberücksichtigung thermaler Effekte auf kurzzeitige Entwicklung von Evaporation, Oberflächentemperatur und Wassergehalt untersucht. Über einen Zeitraum von fünf Tagen wurden Verdunstung, Wassergehalt und Temperatur unter Verwendung eines gekoppelten und eines ungekoppelten Modells berechnet. Beide Modelle wurden unter Annahme feuchter und trockener Anfangsbedingungen durchgeführt. Während Unterschiede zwischen beiden Modellansätzen unter feuchten Anfangsbedingungen vernachlässigbar sind, führen im trockenen Boden Unterschiede in der aktuellen Verdunstung zu relativ großen Unterschieden in der modellierten Bodenoberflächen-temperatur. Im oberen Teil des Bodens haben thermaler und isothermaler Wasserdampffluß einen signifikanten Effekt auf den absoluten Wasserfluß (= flüssiges Wasser + Wasserdampf). Weiterhin wird ein Faktor (enhancement factor, Cass et al. 1984) untersucht, der zur Kompensation von publizierten Abweichungen zwischen theoretisch prognostizierter und experimentell ermittelter Wasserdampfdiffusion eingeführt wurde. Aktuelle Studien zweifeln die Notwendigkeit des Faktors an, sofern Prozesse wie Wasserfilmfluss im Modell berücksichtigt werden. Der Vergleich verschiedener Modellszenarien unter Berücksichtigung und Vernachlässigung des Faktors ergab, dass erweiterte Studien notwendig sind, um eine Redundanz des Faktors zu bekräftigen.

Zweitens wird die Möglichkeit der inversen Bestimmung bodenhydraulischer Eigenschaften über Infrarot (IR)-Messungen untersucht. Die raumzeitliche Entwicklung von Oberflächentemperaturen hängt von der Wasserverfügbarkeit nahe der Bodenoberfläche ab. Mit der Verdunstung von Wasser geht Energie in Form von latenter Wärme über Wasserdampffluss in die Atmosphäre verloren. Da das für die die Evaporation zur Verfügung stehende Wasser von den bodenhydraulischen Eigenschaften abhängt, sollte die zeitliche Entwicklung der Oberflächentemperatur Informationen über oberflächennahe boden-hydraulische Eigenschaften beinhalten. Unter dieser Annahme wurde HYDRUS-1D an einen globalen Optimierungsalgorithmus (DREAM) gekoppelt, um van Genuchten-Mualem Parameter des Bodens aus infrarot ermittelten Temperaturen und TDR gemessenen

Wassergehalten invers zu bestimmen. Dieser Ansatz wurde für synthetische und reale Daten (ermittelt auf einer unbewachsenen und geeggten Ackerfläche) durchgeführt. Der synthetische Ansatz zeigt, dass bodenhydraulische Eigenschaften von Oberflächentemperaturen abgeleitet werden können; zusätzliche Bodenwassergehalts-messungen verringern die Unsicherheit der geschätzten Eigenschaften. Im Unterschied zu dem vertikal homogenen Bodenprofil des synthetischen Ansatzes, musste für reale Messdaten ein zweigeschichtetes Bodenprofil angenommen werden, was zu deutlichen Steigerungen der Unsicherheit in den geschätzten BHE führte. Für die untere Bodenschicht entsprachen die Wasserretentionskurven von ungestörten Bodenproben denen der invers ermittelten Kurven. Die invers bestimmten Retentionskurven der geeggten und damit aufgelockerten oberen Bodenschicht unterschieden sich von denen ungestörter Bodenproben aus der oberen Bodenschicht.

Weiterhin wurde ein mechanistisches Modell zur Untersuchung dreidimensionaler Wasser- und Wärmeflüsse und deren Einfluss auf räumlich variable Evaporationsraten genutzt. Um räumlich variable Verdunstungsraten simulieren zu können, wurde HYDRUS-3D derart modifiziert, dass eine Energiebilanz als Randbedingung für jeden atmosphärischen Knotenpunkt einzeln ermöglicht war. Als Modellkörper wurde eine Bodensäule von 11 cm x 5 cm x 100 cm (x, y, z) mit einer räumlichen Auflösung von einem Zentimeter in jede Richtung verwendet. Ein Teil der Bodensäule wurde mit bodenhydraulischen Eigenschaften eines feinkörnigeren Bodens, der andere Teil mit den bodenhydraulischen Eigenschaften eines grobkörnigeren Bodens charakterisiert. Beide Materialien stehen in einem direkten vertikalen Kontakt zueinander. Modellergebnisse des zusammengesetzten Bodens wurden mit denen eines uniform feinen und groben Bodens verglichen. Konstante meteorologische Bedingungen repräsentativ für Laborbedingungen wurden verwendet. Die Ergebnisse zeigen, daß der absolute Wasserfluss als Resultat des hydraulischen Gradienten von dem groben in den feinen Bodenbereich gerichtet ist, wodurch das grobe Material des zusammengesetzten Bodens im Vergleich zu dem uniform grobkörnigen Boden schneller austrocknet. Basierend auf den Wassergehaltsunterschieden erhöhen sich auch die Temperaturunterschiede zwischen beiden Materialien. Dies führt zu zunehmenden Wärmeflüssen vom groben in das feine Material, die wiederum eine Verdunstungsrate bewirken, die oberhalb

der atmosphärisch geforderten, potentiellen Verdunstungsrate eines uniform feinkörnigen Bodens liegt. Dadurch kann die Vernachlässigung von horizontalen Wärme- und Wasserflüssen in vertikal heterogenen Böden zu einem Fehler in der Abschätzung der Evaporationsraten führen, wenn diese Böden durch effektive Parameter beschrieben werden.

Band / Volume 153
Bildung von sekundären Phasen bei tiefengeologischer Endlagerung von Forschungsreaktor-Brennelementen – Struktur- und Phasenanalyse
A. Neumann (2012), 329 pp
ISBN: 978-3-89336-822-8

Band / Volume 154
Coupled hydrogeophysical inversion for soil hydraulic property estimation from time-lapse geophysical data
M. Cho Miltin (2012), xi, 79 pp
ISBN: 978-3-89336-823-5

Band / Volume 155
Tiefentschwefelung von Flugturbinenkraftstoffen für die Anwendung in mobilen Brennstoffzellensystemen
Y. Wang (2012), 205 pp.
ISBN: 978-3-89336-827-3

Band / Volume 156
Self-consistent modeling of plasma response to impurity spreading from intense localized source
M. Koltunov (2012), V, 113 pp.
ISBN: 978-3-89336-828-0

Band / Volume 157
Phosphorsäureverteilung in Membran-Elektroden-Einheiten dynamisch betriebener Hochtemperatur-Polymerelektrolyt-Brennstoffzellen
W. Maier (2012), VI, 105 pp.
ISBN: 978-3-89336-830-3

Band / Volume 158
Modellierung und Simulation von Hochtemperatur-Polymerelektrolyt-Brennstoffzellen
M. Kvesic (2012), ix, 156 pp.
ISBN: 978-3-89336-835-8

Band / Volume 159
Oxidation Mechanisms of Materials for Heat Exchanging Components in CO_2/H_2O-containing Gases Relevant to Oxy-fuel Environments
T. Olszewski (2012), 200 pp.
ISBN: 978-3-89336-837-2

Band / Volume 160
Ice Crystal Measurements with the New Particle Spectrometer NIXE-CAPS
J. Meyer (2013), ii, 132 pp.
ISBN: 978-3-89336-840-2

Schriften des Forschungszentrums Jülich
Reihe Energie & Umwelt / Energy & Environment

Band / Volume 161
Thermal Shock Behaviour of Different Tungsten Grades under Varying Conditions
O. M. Wirtz (2013), XIV, 130 pp.
ISBN: 978-3-89336-842-6

Band / Volume 162
Effects of ^{137}Cs and ^{90}Sr on structure and functional aspects of the microflora in agricultural used soils
B. Niedrée (2013), XII, 92 pp.
ISBN: 978-3-89336-843-3

Band / Volume 163
Lidar observations of natural and volcanic-ash-induced cirrus clouds
C. Rolf (2013), IX, 124 pp.
ISBN: 978-3-89336-847-1

Band / Volume 164
CO2-Abscheidung, -Speicherung und -Nutzung:
Technische, wirtschaftliche, umweltseitige und gesellschaftliche Perspektive
Advances in Systems Analysis 2
Kuckshinrichs, W.; Hake, J.-F. (Eds.) (2012), iv, 354 pp.
ISBN: 978-3-89336-850-1

Band / Volume 165
Interest Mediation and Policy Formulation in the European Union
Influence of Transnational Technology-Oriented Agreements on European Policy in the Field of Carbon Capture and Storage
Advances in Systems Analysis 3
Schenk, O. (2013), XIII, 253 pp.
ISBN: 978-3-89336-852-5

Band / Volume 166
Versagensverhalten plasmagespritzter Mg-Al-Spinell-Schichten unter Thermozyklierung
Ebert, S. M. (2013), X, 173 pp.
ISBN: 978-3-89336-853-2

Band / Volume 167
Coupled modeling of water, vapor and heat in unsaturated soils - Field applications and numerical studies
Steenpaß, C. (2013), X, 123 pp.
ISBN: 978-3-89336-854-9

Weitere ***Schriften des Verlags im Forschungszentrum Jülich*** unter
http://wwwzb1.fz-juelich.de/verlagextern1/index.asp

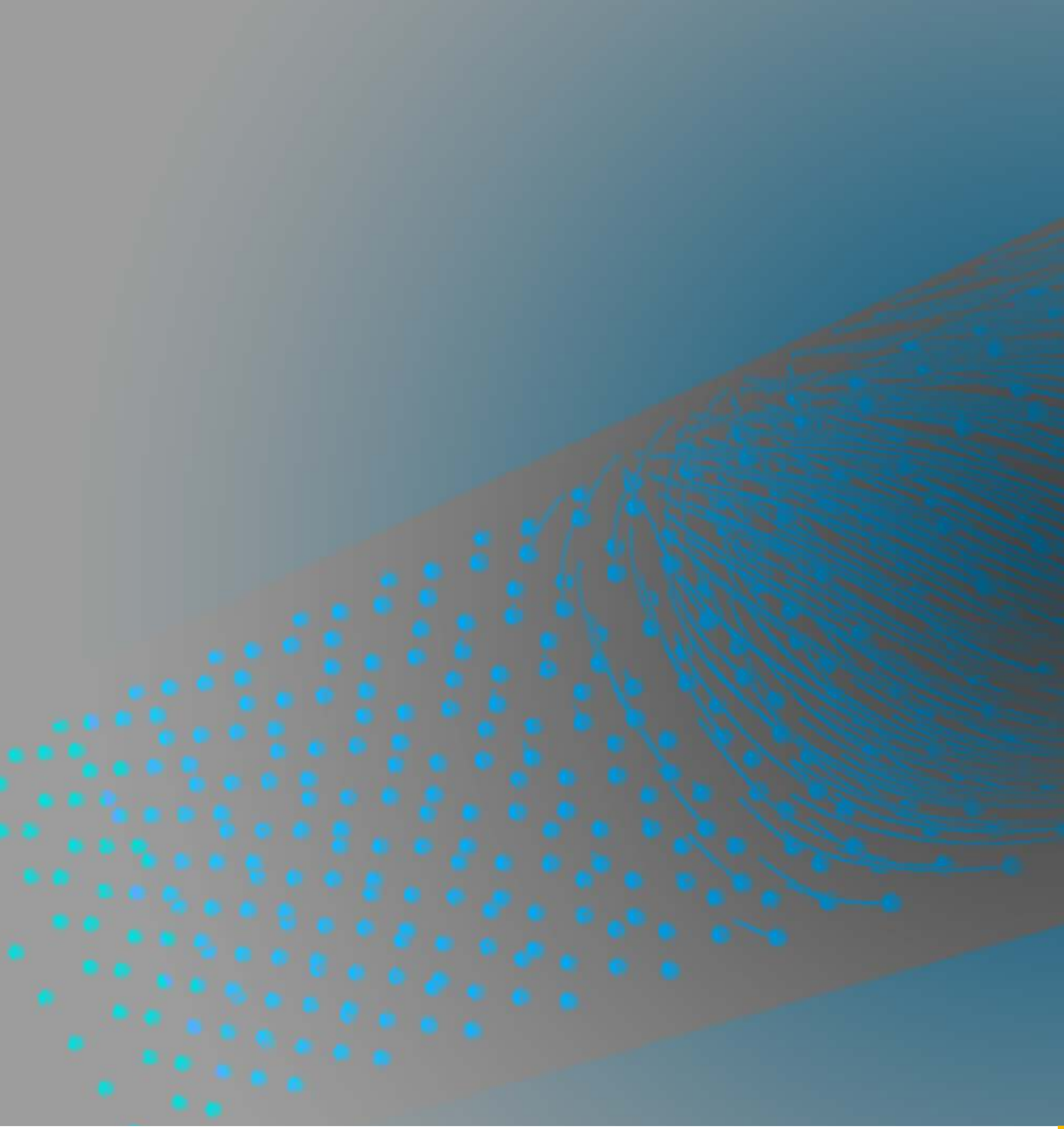

Energie & Umwelt / Energy & Environment
Band / Volume 167
ISBN 978-3-89336-854-9

JÜLICH
FORSCHUNGSZENTRUM